Leibniz-Institut
für Festkörper- und
Werkstoffforschung
Dresden

TECHNISCHE
UNIVERSITÄT
DRESDEN

Investigation of the Superconducting and Magnetic Phase Diagram of Off-Stoichiometric LiFeAs

Dissertation
zur Erlangung des wissenschaftlichen Grades
Doktor rerum naturalium

vorgelegt von

Uwe Gräfe
geboren am 26.03.1986 in Räckelwitz

Leibniz-Institut für Festkörper- und Werkstoffforschung Dresden

Fakultät Mathematik und Naturwissenschaften
der Technischen Universität Dresden
Fachrichtung Physik
2017

Eingereicht am 24. Februar 2017

1. Gutachter: Prof. Dr. Bernd Büchner
2. Gutachter: Prof. Dr. Rüdiger Klingeler

Abstract

At their discovery in 2008, iron pnictide superconductors (IPS) provoked tremendous scientific interest, comparable to the discovery of the cuprate superconductors. So far, IPS reached critical temperatures T_c up to 56 K. Typically, they show an antiferromagnetic (afm) spin density wave (SDW) which has to be suppressed by doping before superconductivity develops, which then is supported by further doping. Due to the close vicinity of the magnetic and the superconducting (sc) phase, magnetic fluctuations are discussed to be responsible for the sc pairing mechanism in IPS.

A special member of the IPS is LiFeAs, because it does not need doping to become sc. It is a stoichiometric superconductor at a T_c of 18 K. In fact, doping is suppressing its T_c. Also, there is no sign of an afm SDW present. Therefore, LiFeAs is a interesting material to study the properties of the IPS in an undisturbed material.

In 2010, experiments of the Leibniz Institute for Solid State and Materials Research Dresden (IFW Dresden) revealed further surprising properties of LiFeAs. Samples with a Li deficiency undergo a ferromagnetic (fm) phase transition at 165 K. Theoretical calculations suggest that fm fluctuations could induce triplet superconductivity in LiFeAs. This would cause a non-vanishing dynamic susceptibility below T_c, which is supported by nuclear magnetic resonance (NMR) experiments.

This thesis is discussing the results of the IFW Dresden experiments, and concludes that this ferromagnetism is of weak itinerant nature. The origin might be an increase of the density of states (DOS) at the Fermi level, which is causing an instability towards fm order, as proposed by the Stoner model.

For further doping experiments, the synthesis procedure of polycrystalline LiFeAs was optimized to get samples with maximum T_c and minimum impurities. Therefore, nuclear quadrupole resonance (NQR) was used. The NQR line width is a measure of impurities in the sample. By minimizing the NQR line width, optimal samples were synthesized. These samples are able to compete with the properties of single crystals.

To investigate the doping behavior of LiFeAs, a scenario with four different kinds of impurities and deficiencies was performed with the optimized synthesis procedure. 24 different samples were analyzed, by means of NQR and electrical conductivity. It was found that in fact Fe excess is responsible for changing the physical properties of LiFeAs, and not Li deficiency. It is causing a shrinking of the unit cell volume, as seen by X-ray diffraction (XRD) measurements and it causes a decrease of T_c. It also leads to a decrease of room temperature resistivity, which is supporting an increase of the DOS at the Fermi level. The NQR frequency is scaling with the amount of Fe excess and can be used to draw the sc and fm phase diagram of off-stoichiometric LiFeAs. At an amount between 3.2 and 3.6 % of Fe excess, LiFeAs undergoes the fm transition.

Contents

1 Introduction **1**

2 Nuclear Quadrupole Resonance **5**

- 2.1 Nuclear Magnetic Moment . . . 5
- 2.2 Nuclear Electric Quadrupole Interaction . . . 6
- 2.3 Energy Levels and Transition Frequencies . . . 9
- 2.4 Excitation and Detection . . . 10
- 2.5 Small Magnetic Fields . . . 12
- 2.6 Large Magnetic Fields . . . 12
- 2.7 Line Widths . . . 13

3 Electrical Conductivity **15**

- 3.1 Drude–Sommerfeld Model . . . 15
- 3.2 Energy Bands . . . 17
  - 3.2.1 Bloch-Electrons . . . 18
  - 3.2.2 Density of States . . . 20
- 3.3 Dynamics . . . 21
  - 3.3.1 Semiclassical Model . . . 21
  - 3.3.2 Motion of Crystal Electrons . . . 23
- 3.4 Scattering Processes . . . 26
  - 3.4.1 Scattering Cross Sections . . . 27
  - 3.4.2 Electron-Phonon-Scattering . . . 28
  - 3.4.3 Scattering at Impurities . . . 28
  - 3.4.4 Electron-Electron-Scattering . . . 29
- 3.5 Ioffe–Regel Criterion . . . 31

4 Properties of LiFeAs **33**

- 4.1 Crystal Structure . . . 33
- 4.2 Electronic Structure . . . 34
- 4.3 Superconductivity . . . 37
- 4.4 Doping Behavior . . . 38
- 4.5 Nuclear Quadrupole and Magnetic Resonance Measurements on LiFeAs . . . 40

4.6 Resistivity Measurements on LiFeAs 42

4.7 Ferromagnetic LiFeAs 43

5 Experimental Setup 47

5.1 Sample Preparation 47

5.2 Nuclear Quadrupole Resonance 48

5.2.1 Temperature Control 49

5.2.2 Measurement Process 49

5.2.3 Quantitative Analysis 50

5.3 Resistivity 51

6 Ferromagnetic LiFeAs 55

6.1 Sample Preparation 55

6.2 Evidence of Ferromagnetism in Li deficient LiFeAs Derivatives 56

6.2.1 Static Susceptibility 56

6.2.2 Ferromagnetic Resonance 57

6.2.3 Muon Spin Resonance 58

6.2.4 Dynamic Magnetic Susceptibility 60

6.2.5 Magnetoresistance 61

6.2.6 Nuclear Quadrupole Resonance 62

6.2.7 Neutron Scattering 64

6.2.8 Summary 64

6.3 Distinctive Properties of ferromagnetic LiFeAs Derivatives 65

6.3.1 Nuclear Quadrupole Resonance 65

6.3.2 Hall Effect and Resistivity 66

6.4 Charge Doping 68

6.5 Stoner Model 68

6.6 Origin of the ferromagnetic transition 70

7 Nuclear Quadrupole Resonance as Tool for the Optimization of LiFeAs Synthesis 73

7.1 Sample Preparation 74

7.2 Nuclear Quadrupole Spectroscopy 74

7.3 Other Sample Characterization 77

7.3.1 Powder X-Ray Diffraction 78

7.3.2 Magnetization 79

7.3.3 Resistivity 80

7.4 Discussion 81

8 Physical Properties of Off-Stoichiometric LiFeAs 85

8.1 Sample Preparation 86
8.2 Nuclear Quadrupole Resonance 86
8.3 X-Ray Diffraction 89
8.4 Static Magnetic Susceptibility 93
8.5 Resistivity 95
8.6 Relevance of the Synthesis Temperature 98
8.7 Summary 102

9 Conclusion and Outlook 105

Bibliography 107

List of Figures 119

List of Tables 123

Acknowledgment 125

Acronyms

µSR muon spin resonance.

AAS automatic adjustment system.

afm antiferromagnetic.

alumina Al_2O_3.

ARPES angle-resolved photoemission spectroscopy.

Ba122 $BaFe_2As_2$.

BZ Brillouin zone.

CSW center of spectral weight.

DMS dynamic magnetic susceptibility.

DOS density of states.

EDX energy dispersive x-ray.

EFG electric field gradient.

ESR electron spin resonance.

FC field cooled.

FID free induction decay.

fm ferromagnetic.

FMR ferromagnetic resonance.

FS Fermi surface.

FWHM full width at half maximum.

ICP inductively coupled plasma optical emission spectroscopy.

ICS iron chalcogenide superconductor.

IFW Dresden Leibniz Institute for Solid State and Materials Research Dresden.

IPS iron pnictide superconductor.

La1111 LaOFeAs.

Li111 LiFeAs.

MPMS-5T Quantum Design Magnetic Properties Measurement System.

NMR nuclear magnetic resonance.

NQR nuclear quadrupole resonance.

pm paramagnetic.

rf radio frequent.

RRR residual resistivity ratio.

SDW spin density wave.

SMS static magnetic susceptibility.

SNR signal to noise ratio.

XRD X-ray diffraction.

ZFC zero-field cooled.

1 Introduction

One large topic of research in condensed matter physics is superconductivity. It denotes the phenomenon of infinite electrical conductivity in a material by cooling it below a transition temperature, called the critical temperature. Since its discovery, more than one hundred years ago, there have been four major breakthroughs on this field of research.

The first is undoubtedly its discovery in 1911 [1]. After that, it took almost 50 years until there was a fundamental understanding, that can describe the properties of superconductors: The BCS model [2], which marks the second breakthrough.

Today, it is commonly known, that superconductivity originates in the formation of pairs of electrons caused by an interaction between the electrons. This pair formation leads to a gap in the energy spectrum which suppresses excitations of the electrons, resulting in the vanishing resistivity. For many materials, these pairing mechanism is mediated by phonons. From the BCS model, it was clear, that the possibilities to reach very high values for the critical temperature with a phonon mediated pairing mechanism are limited.

These limitations were passed by the third major breakthrough in 1986: The discovery of the high temperature superconductivity in cuprates [3]. The critical temperatures of this material class soon exceeded the boiling point of nitrogen, bringing more applications of superconductivity in reach. These materials cannot be described by the BCS model anymore and, thus, the cuprates are unconventional superconductors. For more than 20 years, the cuprates were the prime example for high temperature superconductors, until the fourth breakthrough in 2008.

The discovery of a critical temperature of 26 K in $LaO_{0.89}F_{0.11}FeAs$ [4] was the starting point for the research interest in the iron pnictide superconductors (IPS). From there on, many more members of the IPS were found in very short intervals and soon the maximum critical temperature rose up to 56 K in $Sr_{0.5}Sm_{0.5}FFeAs$ [5].

Typically, the IPS are not stoichiometric superconductors. They show a magnetic transition to an antiferromagnetic (afm) spin density wave (SDW). It is a magnetic order which is defined by a periodicity, which does not have to coincide with the lattice structure of the crystal. The wave vector of the SDW is the same as a nesting vector, which maps main parts of the Fermi surface (FS) on each other. Therefore, nesting is discussed to be responsible for the formation of the SDW in IPS.

Superconductivity is induced after the suppression of the SDW order, which is usually done by doping. Due to the close vicinity of magnetic and superconducting order, magnetic fluctuations are the most favored candidate to mediate the pairing interaction.

The topic of this work is LiFeAs. Although, it is only one member of the class of IPS, it is a quite unique one. Its structure is known for quite a long time, already since 1968 [6], but this can be said about many of the IPS. When superconductivity was detected in LiFeAs [7–9], it was the only IPS being a stoichiometric superconductor. There is no further variation of the composition necessary to induce superconductivity. Moreover, there are no signs of nesting, or of a SDW, present in this material. In other IPS, the superconducting transition temperature T_c can be increased by doping, but in LiFeAs, any kind of doping is decreasing T_c [10, 11].

Thus, LiFeAs is a very interesting member of the IPS, but it is guarding its secrets quite well. The high reactivity of Li with moist air, which destroys the samples in a couple of minutes, make precautions necessary, which complicate any measurement.

In 2010, experiments of the Leibniz Institute for Solid State and Materials Research Dresden (IFW Dresden) revealed more surprising properties of LiFeAs. Samples with a Li deficiency undergo a ferromagnetic (fm) transition at 164 K, which was confirmed by several methods. The proximity of LiFeAs to ferromagnetism was also found by theoretical models of its band structure [12]. Due to this vicinity, it is thought that also fm fluctuations might be responsible for the superconducting pairing mechanism.

These type of fluctuations would also lead to a different kind of pairing of the electrons. In conventional superconductors, the electrons are paired with anti-parallel spin-alignment which is called singlet superconductivity. For fm fluctuations, the electrons should pair with parallel spin, and the pair is then called a triplet. By understanding the nature of the ferromagnetism in LiFeAs, deeper insights in its superconducting properties might become possible.

The purpose of this thesis is to investigate the superconducting and fm phase diagram of off-stoichiometric LiFeAs. Therefore, as a starting point, it is combining the results of different experiments conducted at the IFW Dresden to get a comprehensive view on the properties of the ferromagnetism in LiFeAs.

For a phase diagram, a controlled doping scheme is necessary and, therefore, a control group of stoichiometric material is needed. To get this control group, the synthesis procedure of polycrystalline stoichiometric LiFeAs was optimized. From these stoichiometric samples, a study with different types of off-stoichiometries was performed to see which processes are necessary to drive LiFeAs to the fm transition in a systematic fashion.

In the investigation of LiFeAs, nuclear quadrupole resonance (NQR) plays a major role to uncover alternations in its structure, since LiFeAs is showing distinctive properties in the NQR point of view. NQR is a spectroscopic method, which uses radio frequent (rf) pulses to excite nuclear energy states, originating in the magnetic exchange interaction of a selected nucleus with its electromagnetic environment. This exchange interaction is sensitive to structural changes, which then can be detected by NQR. In the frame of this thesis, NQR was used for the optimization of the synthesis procedure of polycrystalline LiFeAs. Moreover, the distinctive properties of LiFeAs in NQR were used to draw its phase diagram.

It is clear from the start, that another important method to investigate superconductors is the measurement of its electrical resistivity. It is providing insights in fundamental physical properties, and can reveal not only superconductivity, but also changes of the electronic band structure, induced by stoichiometric modifications.

This thesis has the following structure. The first two chapters will give introductions on the physical background of the techniques of NQR and electrical resistivity measurements. They are followed by a chapter about the properties of LiFeAs. Afterwards, a brief summary about the applied experimental setups is given. This is followed by chapter 6 about the detection of ferromagnetism in Li-deficient LiFeAs. Chapter 7 will show a study about the optimization of the synthesis of stoichiometric LiFeAs, which is used as a starting point for off-stoichiometric LiFeAs-samples, whose properties are investigated in chapter 8.

2 Nuclear Quadrupole Resonance

The history of nuclear quadrupole resonance (NQR) dates back to the year 1950 when the first NQR experiments were reported by Dehmelt and Krüger on ^{35}Cl in trans-dichloroethylene [13]. NQR is closely related to nuclear magnetic resonance (NMR). Both methods use radio frequent (rf) magnetic fields to induce transitions between nuclear energy levels. The difference between the two methods is that NMR uses an external static magnetic field to induce the splitting of energy levels, while NQR takes advantage of the splitting due to the interaction of the nuclei with internal electric field gradients (EFGs) of the material. As such, NQR experiments do not require an applied static magnetic field.

NQR requires nuclei of isotopes with a high natural abundance, which have a nuclear spin $I > \frac{1}{2}$ and are located at a lattice site in a solid which has a lower symmetry than tetragonal.

Typical measurands of NQR, which it has also in common with NMR, are transition frequencies and relaxation rates. NQR is sensitive to crystal symmetries and bonding. It can therefore obtain detailed information on lattice constant changes, phase transitions in solids and other properties. As such, it can be used as thermometer, pressure sensor, or even material detector.

This chapter is mostly based on [14–17] and will give an overview on the physical basics of NQR.

2.1 Nuclear Magnetic Moment

Although, it is called nuclear quadrupole resonance it is, like in NMR, the interaction of the nucleus, or better its magnetic moment, with magnetic fields that makes NQR possible.

The nucler moment or nuclear spin $\mathbf{I}$ of a nucleus consists of the angular moments $\mathbf{l}_i$ and the spins $\mathbf{s}_j$ of each nucleon. Both, neutrons and protons have a spin $S = \frac{1}{2}$. Since the angular moment is integer, the total angular moment is integer, for an even number of nucleons and half-integer for an odd number of nucleons.

It appears that, protons and neutrons appear in pairs of its type. Thus, their spins annihilate each other to a total spin of $\mathbf{S} = 0$, i.e., nuclei with an even number of protons and an even number of neutrons have a total angular moment of $\mathbf{I} = 0$, since NQR usually probes the ground state with zero angular moment.

The total nuclear moment of the nucleus is connected with its magnetic moment $\vec{\mu}$ such that

$$\vec{\mu} = \gamma\hbar\mathbf{I}, \tag{2.1}$$

where γ is the gyromagnetic ratio and $\hbar$ is Planck's constant.

This operator is defined such, that if applied on its eigenfunctions $|I, m\rangle$

$$\mathbf{I}^2 |I, m\rangle = I(I+1) |I, m\rangle \tag{2.2}$$

$$I_z |I, m\rangle = m |I, m\rangle, \tag{2.3}$$

where I_z is the arbitrarily chosen z-component which commutes with $\mathbf{I}^2$. Its eigenvalues m can take any of the $2I + 1$ values from $-I, -I+1, ..., I-1, I$.

So, eq. (2.1) can be rewritten as

$$\langle I, m| \mu_{x'} |I, m'\rangle = \gamma\hbar \langle I, m| I_{x'} |I, m'\rangle, \tag{2.4}$$

to describe the matrix elements of the magnetic moment in the arbitrary x'-direction.

2.2 Nuclear Electric Quadrupole Interaction

With the nuclear magnetic moment, one of the necessary parts of NQR is defined. This section will describe its interaction with the surrounding electrical environment.

A multipole expansion of the electrical field of the nucleus yields 2^n-poles with n being even (monopoles, quadrupoles, etc.). In a solid, the nucleus is located at an equilibrium position where the resulting electrical field between the nucleus and the surrounding environment is zero. To observe non-zero interactions between the nucleus and its environment, a closer look has to be taken on higher moments of the electrical field of the nucleus. Since the multipole moments generally get weaker rapidly with increasing n, the strongest non-zero interaction stems from the quadrupole moment of the nucleus, which can be described by the quadrupole tensor $\hat{Q}$.

A quadrupole moment arises from nuclei which have a non-spherical charge distribution which is either prolate or oblate. For a known charge distribution the scalar quadrupole moment Q can be calculated by

$$eQ = \int \varrho(3z^2 - r^2) d\tau. \tag{2.5}$$

The z-axis represents the direction of axial symmetry, e is the elementary charge and ϱ

the nuclear charge density integrated over the nucleus volume. Q describes if the charge distribution is prolate ($Q > 0$) or oblate ($Q < 0$). For a spherical charge distribution, e.g. nuclei with nuclear spin of 0 or $\frac{1}{2}$, the integral in eq. (2.5) vanishes and Q is zero.

Due to external charges close to the nucleus, the EFG is defined by the spatial derivatives of the corresponding electrostatic potential V at the site of the nucleus. If the nucleus is located at the origin of the coordinate system the derivatives are:

$$V_{jk} = \left.\frac{\partial^2 V}{\partial r_j \partial r_k}\right|_0 . \tag{2.6}$$

Here, r_j corresponds to x,y and z. From the Laplace-equation,

$$\sum_{i=x,y,z} V_{ii} = 0, \tag{2.7}$$

follows that, the resulting field gradient $\hat{V}$ can be treated as a real, symmetric, traceless tensor. Thus, it can be diagonalized by choosing the principal axes as basis. Now the following definitions are made:

$$eq = V_{zz}, \tag{2.8a}$$

$$\eta = \frac{V_{yy} - V_{xx}}{V_{yy} + V_{xx}} = \frac{V_{xx} - V_{yy}}{V_{zz}}, \tag{2.8b}$$

where η is the asymmetry parameter. The principal axes are usually chosen such that

$$|V_{xx}| \leq |V_{yy}| \leq |V_{zz}|, \tag{2.9a}$$

$$0 \leq \eta \leq 1. \tag{2.9b}$$

Since the principal axes are determined by the environment surrounding the nucleus, those axes are referred to as the *crystal coordinate system*[1]. Here,

$$\begin{aligned} V_{xx} &= V_{yy} = -V_{zz}/2 \text{ and} \\ \eta &= 0 \end{aligned} \tag{2.10}$$

describe axial symmetry.

Figure 2.1 shows a schematic of two orientations of a prolate nucleus ($Q > 0$) at a point where the electric field is zero in the vicinity of four fixed point charges. The configuration in fig. 2.1(a) will have a lower energy than that shown in fig. 2.1(b) because the positive

---

[1] In this work, the crystal coordinate system will be marked by non-primed variables. Primed variables refer to an arbitrary coordinate system which does not have to coincide with the crystal coordinate system.

charge is on the whole closer to the negative charges. In quantum mechanics, the different energies for the two shown orientations give rise to a splitting of the nuclear energy levels. The width of the splitting is related to the orientation of the nucleus.

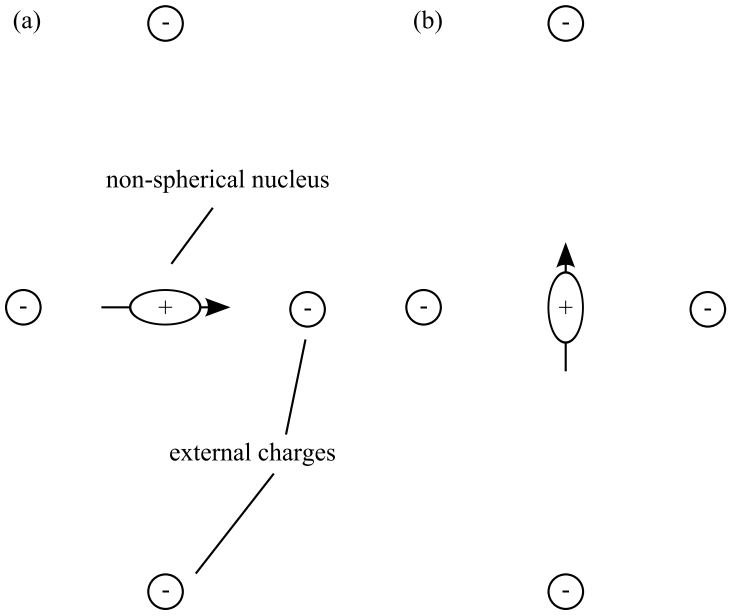

Figure 2.1: Two configurations of a non-spherical nucleus near charges external to the nucleus. The configuration at (a) has a lower energy than that shown at (b) since the negative charges are closer to the nucleus [17].

Since the nuclear state can be expressed by the nuclear angular momentum, the interaction between the quadrupole moment and the EFG can be described in terms of the angular momentum. The Hamiltonian $\mathcal{H}_Q$ for a nucleus of spin I expressed in the crystal coordinate system is

$$\mathcal{H}_Q = -\hat{Q}\hat{V}, \tag{2.11a}$$

$$\mathcal{H}_Q = \frac{e^2 qQ\hbar^2}{4I(2I-1)} \left[3\hat{I}_z^2 - \hat{I}^2 + \eta \frac{\hat{I}_+^2 - \hat{I}_-^2}{2} \right] \tag{2.11b}$$

with angular momentum raising and lowering operators $\hat{I}_\pm = \hat{I}_x \pm i\hat{I}_y$.

2.3 Energy Levels and Transition Frequencies

For axial symmetry ($\eta = 0$), the resulting $2I+1$ energy levels, for $m = -I, -I+1, ..., I-1, I$, of the Hamiltonian are given by

$$E_m = \frac{e^2 qQ}{4I(2I-1)} \left(3m^2 - I(I+1)\right). \tag{2.12}$$

It should be possible to detect the presence of such set of energy levels by spectral absorption. An interaction, causing transitions between levels, is needed. It is possible to take a time dependent interaction of frequency ν such that,

$$h\nu = \Delta E, \tag{2.13}$$

where ΔE is the energy difference between the initial and final energies. The interaction must have a non-vanishing matrix element joining the initial and final states.

Defining the quadrupole frequency

$$\nu_Q = \frac{3e^2 qQ}{4I(2I-1)h} \tag{2.14}$$

where h is Planck's constant, the allowed transition frequencies are given by

$$\nu_{m,m\pm1} = \nu_Q |(2m \pm 1)| \text{ where } |m|,\ |m \pm 1| \leq I. \tag{2.15}$$

This work shows NQR-experiments on ^{75}As, which has a spin $I = \frac{3}{2}$. Therefore, further discussions concentrate on $I = \frac{3}{2}$-systems. For a spin $I = \frac{3}{2}$, it is possible to specify the energy levels for $\eta \neq 0$, which leads to the expressions

$$E_{\pm3/2} = h\nu_Q \left(1 + \frac{\eta^2}{3}\right)^{1/2}, \tag{2.16a}$$

$$E_{\pm1/2} = -h\nu_Q \left(1 + \frac{\eta^2}{3}\right)^{1/2}, \tag{2.16b}$$

and the transition frequency

$$\nu = 2\nu_Q \left(1 + \frac{\eta^2}{3}\right)^{1/2}. \tag{2.17}$$

As it is visible from fig. 2.1, the direction of the spin does not affect the energy of the nucleus in the field gradient. Therefore, the energy levels of $E_{\pm3/2}$ and $E_{\pm1/2}$ are doubly degenerated and there is only one transition frequency ν.

2.4 Excitation and Detection

An rf magnetic field of magnitude $2H_1$ is able to couple to the nuclear magnetic moment and it induces transitions corresponding to $\Delta m = \pm 1$. Because of the degeneracy of the states, there is only one transition frequency for $I = \frac{3}{2}$.

The Hamiltonian for an applied rf magnetic field is

$$\mathcal{H} = \mathcal{H}_Q + \mathcal{H}_1, \tag{2.18a}$$

$$\text{with } \mathcal{H}_1 = -\gamma\hbar\mathbf{I}\cdot\mathbf{H}(t). \tag{2.18b}$$

A coil provides the rf magnetic field, defined by $|\mathbf{H}(t)| = H_{x'} = 2H_1\cos\omega t$, along the x' axis. The field is turned on for the time $0 < t < t_w$ and it is $H_{x'} = 0$ for $t > t_w$. Since the field is not continuous for all times t, it is called a pulsed field or pulse. The wave function ψ of $\mathcal{H}$ for $I = \frac{3}{2}$ can be expressed in terms of eigenfunctions of the electrical quadrupole interaction $\mathcal{H}_Q$

$$\psi = \sum_{m=-\frac{3}{2}}^{\frac{3}{2}} C_m(t)\,|I,m\rangle\, e^{-i\nu_m t}, \tag{2.19}$$

where $\nu_m = \nu_{-m} = \frac{E_m}{h}$.

After solving the time-dependent Schrödinger equation, it is possible to describe the system at all times. At $t = 0$, the system is in thermal equilibrium and an excess spin population is established for $m = \pm\frac{3}{2}$ for $Q > 0$.

The population of the different states is redistributed after the pulse, $t \geq t_w$. The redistribution leads to a non-vanishing nuclear magnetization in the $x'y'$ plane. The average magnetic moment in x' direction can be described by [14]

$$\bar{\mu}_{x'}(t) = \gamma\hbar\left(\frac{\sqrt{3}}{2}\right)\sin(\sqrt{3}\gamma H_1 t_w)\sin(\omega_0(t - t_w)). \tag{2.20}$$

The total magnetization $M_{x'}$ is then given by

$$M_{x'} = N\cdot\bar{\mu}_{x'}, \tag{2.21}$$

with N being the number of nuclei. In a coil, this time-dependent magnetization causes an electromotive force

$$V(t) \propto \frac{dM_{x'}}{dt} \tag{2.22}$$

by Faraday's law of induction which results in the measurement signal.

The expectation value $\bar{\mu}_{x'}$ is becoming maximal if $\sqrt{3}\gamma H_1 t_w = \omega_1 t_w = \frac{\pi}{2}$. Therefore, a pulse of length $t_w = \frac{\pi}{2\omega_1}$ is called a $\frac{\pi}{2}$-pulse or 90°-pulse. The magnetization $M_{x'}$ which is induced by the 90°-pulse is called free induction. Strains and imperfections in the crystal and a temperature gradient over the sample can lead to a dephasing process and thus, to a consequent attenuation of $\bar{\mu}_{x'}$. This leads to a decay process of the expectation value $\bar{\mu}_{x'}$ and thus also for the magnetization $M_{x'}$ [14]:

$$\bar{\mu}_{x'}(t) = \gamma\hbar \left(\frac{\sqrt{3}}{2}\right) \sin(\sqrt{3}\gamma H_1 t_w) \sin(\omega_0(t - t_w)) \exp(-\frac{1}{2}\delta^2(t - t_w)^2). \tag{2.23}$$

Since the free induction is decaying, the process is called free induction decay (FID).

If after a time τ, another pulse is applied, the decay process can be reversed partially. Depending on the length of the second pulse t_w, the time dependency of some of the angular momenta gets reversed and after another time τ, after the second pulse, the expectation value $\bar{I}_{x'}$ and thereby $M_{x'}$ is partially reestablished, like an echo. Therefore, it is called spin echo.

If for the second pulse the pulse length is $t_w = \frac{\pi}{\omega_1}$, i.e. a π-pulse or 180°-pulse, the time dependencies of every involved angular momentum get reversed and the resulting spin echo is maximized.

Compared to the FID, the spin echo has the advantage that its amplitude does not depend on time-dependent inhomogeneities. In fig. 2.2, a schematic of such a pulse sequence can be seen. The effect of forming spin echoes was first detected and described for NMR-experiments in 1950 [18].

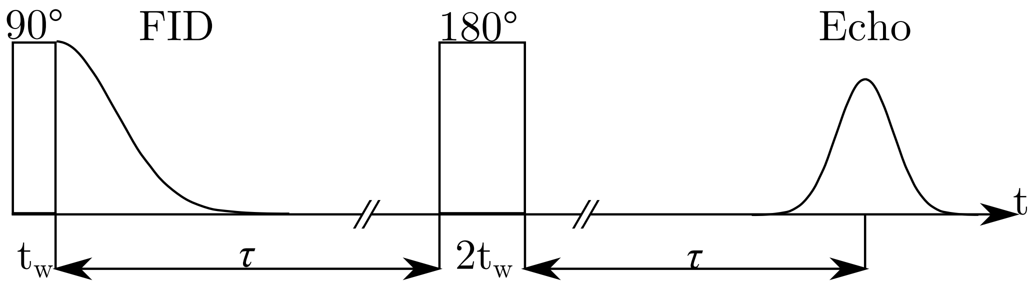

Figure 2.2: Schematic spin echo pulse sequence with a 90°-pulse and a 180°-pulse.

2.5 Small Magnetic Fields

The effects of small magnetic fields H_s ($\gamma H_s \ll \nu_Q$) are usually unavoidable in NQR-experiments, e.g. the effect of the earth magnetic field, although they can be useful in certain cases. For example in the presence of an asymmetric field gradient ($\eta \neq 0$), the perturbation with a small magnetic field can be used to determine the asymmetry parameter η.

In case of $I = \frac{3}{2}$, the Zeeman-effect caused by the small magnetic field leads to a splitting of the two energy states described in section 2.3. Transitions are now allowed between all four of these new states. The most prominent ones are the following four:

$$\begin{aligned}
\omega_\alpha &= \frac{E_{+3/2} - E_{+1/2}}{\hbar}, \\
\omega_{\alpha'} &= \frac{E_{-3/2} - E_{-1/2}}{\hbar}, \\
\omega_\beta &= \frac{E_{+3/2} - E_{-1/2}}{\hbar}, \\
\omega_{\beta'} &= \frac{E_{-3/2} - E_{+1/2}}{\hbar}.
\end{aligned}$$

The distances between the energy levels are depending on the angle between the perturbing field and the principal axes of the EFG. For single crystals, it is now possible to measure the angular dependency of the NQR-signal. For polycrystals, it is possible to analyze the line shape. Thus it is possible to get information of anisotropic effects.

2.6 Large Magnetic Fields

In case of large magnetic fields H_l ($\gamma H_l \gg \nu_Q$), the method of NQR is transformed into NMR. Now, the EFG causes small perturbations to the large magnetic field. This field can have different reasons. One reason might be that a typical NMR-experiment with a large external magnetic field is done. Another reason might be that the material itself shows an internal magnetic field, as it would be the case for antiferromagnetic (afm) or ferromagnetic (fm) materials. The method used in such a case is called zero-field NMR, since no external field is needed to cause a Zeeman-splitting.

For a sample which undergoes a magnetic transition, e.g. fm, the temperature-dependent NQR-signal shows an abrupt loss of intensity. The reason is that the NMR-frequency of the nucleus lies usually far away from the NQR-frequency and thus the applied rf field of the NQR-experiment is suddenly off-resonance.

2.7 Line Widths

For a completely homogeneous crystal, consisting at least partially of nuclei with $I = \frac{3}{2}$, whose energy states get excited by a sharp rf magnetic field, i.e. a field with a narrow band width, the NQR-spectrum would show a single line at only the resonance frequency. However, due to various effects this singular line gets broadened. The broadening effects of the NQR-spectrum can mostly be divided into magnetic effects and electrical effects.

For the magnetic effects, there is at first the direct dipole-dipole interaction of the nucleus with its neighboring atoms. This means that, the magnetic moment of the investigated nucleus interacts with the magnetic moments of its surrounding nuclei. The amount of this broadening effect is usually of the order of 1 kHz.

Another effect is the indirect spin-spin coupling of the nucleus with the surrounding electrons, e.g. itinerant electrons of metals. This leads to a broadening of the NQR-line if the bonding is of equal strength, like in metals or ionic crystals.

For polycrystals, there is a further magnetic effect which can usually not be excluded. It is the effect of the magnetic field of the earth. Due to the various orientations of the grains to the earth magnetic field, the caused Zeemann-splitting leads to a broadening effect. This broadening is of the order of $\Delta\omega = 2\gamma H_{\text{earth}}$. For ^{75}As this is between 0.1 kHz and 0.7 kHz.

The electrical effects of broadening the line width can be all brought down to the effect that they somehow cause a distribution of frequencies due to small variations of the EFGs. The reasons for these deviations are several: Common causes are impurities, crystal lattice defects, and dislocations and strains in the crystal or the powder grains.

3 Electrical Conductivity

Next to nuclear quadrupole resonance (NQR), which was described in the previous chapter, another method has a high importance for this thesis: The electrical conductivity. It is a measure on how much force is needed to move charged particles with a given velocity through an electrical conductor. Measurements of it are widely used in all natural sciences. In solid state physics, it can give information about a metallic or non-metallic behavior, on charge carriers, phase transitions, scattering effects, and many more.

In this work, it is mostly used to get information on scattering effects and charge carriers of the investigated LiFeAs samples and to confirm superconducting transition temperatures. To understand the processes leading to the presented results, this chapter will give an introduction on the basic principles of electrical conductivity.

This chapter is based on ref. [19].

3.1 Drude–Sommerfeld Model

The description of metallic conductivity by the motion of completely free electrons was developed much earlier than the development of quantum mechanics. Already in 1900, Paul Drude developed a classical model for a gas consisting of free electrons [20]. This classical theory was based on the wrong conception, that the velocity distribution of electrons in the free electron gas can be described by the Maxwell–Boltzmann distribution. Still, it had some rather random successes like the deduction of Ohm's law or the relation between electrical and thermal conductivity, but it could not explain the specific heat, the thermolectric effect, or the magnetic susceptibility of metals. After the development of quantum mechanics, Arnold Sommerfeld put Drude's theory on a quantum mechanical basis. He used the Pauli principle on the free electrons and did describe the velocity distribution by Fermi–Dirac statistics, which was the transition from a classical to a quantum gas. Today, the model of the conductivity of the free electron gas is called the Drude–Sommerfeld model.

The electrical conductivity σ of a solid body is defined as proportionality constant between the electrical field $\mathbf{E}$ and the resulting electrical current density $\mathbf{J}_q$:

$$\mathbf{J}_q = \sigma \mathbf{E} \tag{3.1}$$

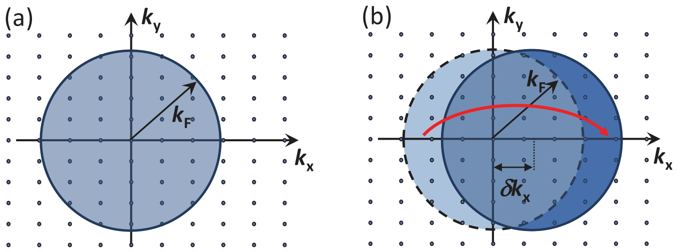

Figure 3.1: The Fermi sphere encloses all occupied electron states in the $\mathbf{k}$-space. (a) For $\mathbf{F} = 0$ the total momentum is zero, because for every wave-vector $\mathbf{k}$ exists a corresponding wave-vector $-\mathbf{k}$. (b) For $\mathbf{F} \neq 0$ every wave-vector $\mathbf{k}$ grows by the amount $\delta\mathbf{k} = \frac{\mathbf{F}t}{\hbar}$, i.e., shifting the Fermi sphere by $\delta\mathbf{k}$. The states of the light blue area on the left are relocated to the dark blue area on the right [19].

To calculate the electrical conductivity of a solid body, $\mathbf{J}_q$ has to be described as a function of the average velocity $\langle\mathbf{v}\rangle = \left\langle\frac{\hbar\mathbf{k}}{m}\right\rangle$:

$$\mathbf{J}_q = -en\langle\mathbf{v}\rangle = -en\frac{\hbar}{m}\langle\mathbf{k}\rangle = -e\frac{1}{V}\sum_{\mathbf{k},\sigma}\frac{\hbar\mathbf{k}}{m}. \tag{3.2}$$

Here, e is the elementary charge. In thermal equilibrium, $\langle\mathbf{k}\rangle = 0$ and there is no current. A finite electrical current density is only achievable by a non-equilibrium situation:

$$\mathbf{J}_q = -\frac{en\hbar}{m}\left[\langle\mathbf{k}\rangle - \langle\mathbf{k}\rangle^0\right] = -\frac{en\hbar}{m}\delta\mathbf{k}. \tag{3.3}$$

If the momentum distribution of the electrons deviates from the equilibrium distribution, there is a finite current density.

The momentum distribution in a specific region of space can be changed by external forces and scattering processes. By the force $\mathbf{F} = e\mathbf{E}$, the wave-vectors of the electron states get changed by the amount $\delta\mathbf{k}$ in the time t. This corresponds to the shift of the whole Fermi sphere by $\delta\mathbf{k}$ during the time t (see fig. 3.1). By switching off the force, $\delta\mathbf{k}$ is relaxating to zero by $\delta\mathbf{k} \propto e^{-\frac{t}{\tau}}$ because of scattering processes.

For stationary processes, $\frac{d\langle\mathbf{k}\rangle}{dt} = 0$, it follows

$$\delta\mathbf{k} = -\frac{e\mathbf{E}}{\hbar}\tau \tag{3.4}$$

which leads to Ohm's law:

$$\mathbf{J}_q = \frac{ne^2\tau}{m}\mathbf{E} \tag{3.5}$$

With eq. (3.1), the electrical conductivity is given by

$$\sigma = \frac{ne^2\tau}{m} = \frac{ne^2 l}{mv_F}. \tag{3.6}$$

Figure 3.2: Exemplification of the energy margin in which scattering is possible. Scattering processes far inside the Fermi sphere are forbidden by the Pauli principle. Only electrons within the energy margin of width $\propto k_B T$ around the Fermi energy can participate in scattering processes [19].

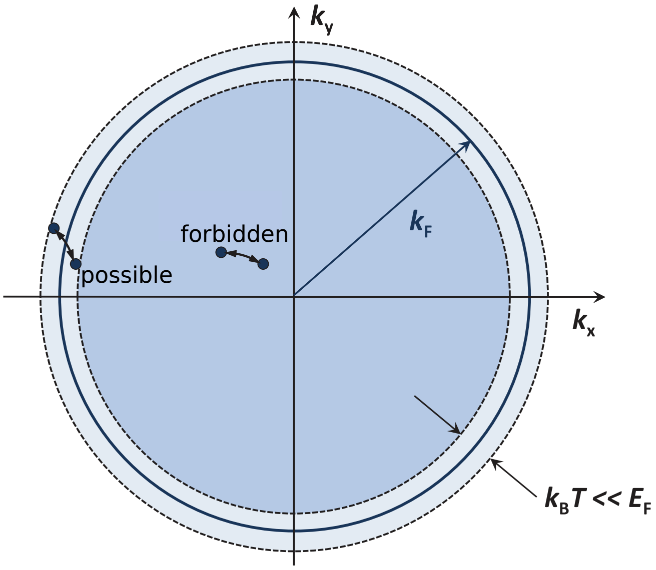

Here $l = v_F \tau$ is the free mean path. It is the distance an electron passes in the average time τ between two scattering processes. It is important to note that l has to be calculated by the Fermi velocity $v_F = \frac{\hbar \mathbf{k}_F}{m}$ and not by the drift velocity v_D of the electrons. This is because only electrons in a small energy interval of width $\propto k_B T$ around the Fermi energy can participate in scattering processes (see fig. 3.2). Since the maximum energy transfer for any scattering process is in the order of $k_B T \ll E_F$, electrons much below the the Fermi energy cannot particpate in scattering processes, because there are no free states to be scattered into. Only electrons in the region of width $\propto k_B T$ around the Fermi energy, i.e. electrons with $v \approx v_F$, can find free states and are able to be scattered.

Equation (3.6) can be interpreted in the following way: The charge transported is proportional to ne. The factor $\frac{e}{m}$ comes from the acceleration by the electrical field which is proportional to $\frac{e}{m}$. Finally, τ or $l = v_F \tau$ describes the time- or length-interval during which an electron can be accelerated until it is slowed down by a scattering process.

3.2 Energy Bands

In a solid body, the electrons can not move completely free. The electrons are influenced by the potential of the atomic cores. Since the atoms are arranged in a periodic lattice, their potentials can be combined to a periodic crystal potential $V(\mathbf{r})$. So, the electrons are not free but they will be treated as non-interactive with each other.

To treat the electrons as quasi-free, the description starts at the free electron gas and treats the additional periodic potential as a small perturbation. This will lead to the formation of energy bands which are divided by energy gaps from each other.

3.2.1 Bloch-Electrons

An ideal solid body is a strict periodic arrangement of atoms. Electrons can move through the lattice without getting affected by the atomic cores. This is possible because, electrons can be described as plane waves which are modulated by the lattice. These lattice-modulated waves are called Bloch waves [21]. The eigenvalues E of the Schrödinger equation can be indicated by the wave vector $\mathbf{k}$ of the Bloch waves:

$$E_{\mathbf{k}} = E(\mathbf{k}) \tag{3.7}$$

For every $\mathbf{k}$, infinite solutions $E_n(\mathbf{k}) = E(\mathbf{k} + \mathbf{G}_n)$ of the Schrödinger equation exist, with $\mathbf{G}_n$ being the reciprocal lattice vector of E_n. Therefore, the number n, called band index, is necessary to classify the different solutions. The indication is typically done by size:

$$E_1(\mathbf{k}) \leq E_2(\mathbf{k}) \leq \cdots \leq E_n(\mathbf{k}) \leq E_{n+1}(\mathbf{k}) \leq \cdots . \tag{3.8}$$

Crystal Momentum

Due to the periodicity of the lattice-potential, it follows

$$\Psi_{\mathbf{k}+\mathbf{G}}(\mathbf{r}) = \Psi_{\mathbf{k}}(\mathbf{r}). \tag{3.9}$$

So, Bloch-waves, which differ only in a reciprocal lattice-vector $\mathbf{G}$, are identical. Therefore, $\hbar\mathbf{k}$ can not be used as the momentum of the electrons, because $\mathbf{k}$ is not uniquely defined.

To define the index $\mathbf{k}$ of a Bloch wave, it is common to choose $\mathbf{k}$ from the first Brillouin zone (BZ). If there exists a $\mathbf{k}'$, then there always exists a reciprocal lattice vector $\mathbf{G}$ such that

$$\mathbf{k} = \mathbf{k}' + \mathbf{G}. \tag{3.10}$$

$\mathbf{k}$ is called the crystal momentum. Bloch-waves are no eigenfunctions of the crystal momentum, because $\mathbf{k}$ is not translational-invariant in general, but discretely.

With the crystal momentum $\mathbf{k}$, it is possible to specify the group velocity of a Bloch wave $\Psi_{n,\mathbf{k}}$ by

$$v_{n,\mathbf{k}} = \frac{1}{\hbar}\frac{\partial E_n(\mathbf{k})}{\partial \mathbf{k}}. \tag{3.11}$$

So, the velocity of Bloch-electrons is given by the dispersion relation $E_n(\mathbf{k})$ of its energy eigenvalues.

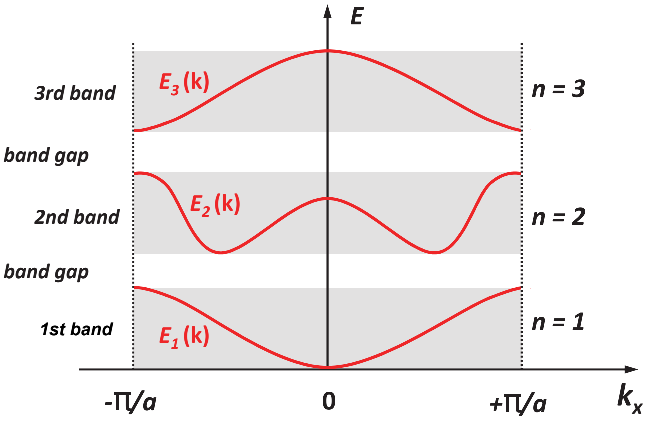

Figure 3.3: Qualitative picture of the energy bands $E_n(\mathbf{k})$ for a given crystal direction. The energy bands are divided by energy gaps [19].

Dispersion Relation and Band Structure

For any possible value $\mathbf{k}$, the Schrödinger equation provides a set of energy eigenvalues $E_n(\mathbf{k})$ which are labeled by the band index n. An example of such functions $E_n(\mathbf{k})$ is shown in fig. 3.3.

As the periodicity of the lattice potential defines the properties of the wave functions, it also defines the properties of the energy eigenvalues.

The properties of $E_n(\mathbf{k})$ are:

- The energy eigenvalues $E_n(\mathbf{k})$ are periodic functions of the quantumnumber $\mathbf{k}$, which is the wave-vector of the Bloch-waves.
- The function $E_n(\mathbf{k})$ is bounded. For a given index n, $E_n(\mathbf{k})$ covers only a finite region, which is called the band width W. Therefore, $E_n(\mathbf{k})$ is called an energy band.
- The different bands are divided by forbidden regions, which are called energy gaps[1].
- For inversion symmetry, i.e. $V(\mathbf{r}) = V(-\mathbf{r})$,

$$E_n(\mathbf{k}) = E_n(-\mathbf{k}) \tag{3.12}$$

  This leads to $\left(\frac{\partial E_n(\mathbf{k})}{\partial \mathbf{k}}\right)_{\mathbf{k}=0} = 0$. So, for any direction of $\mathbf{k}$, there are minimum and maximum values of $E_n(\mathbf{k})$.

- For a general potential,

$$E_n(\mathbf{k}, \uparrow) = E_n(-\mathbf{k}, \downarrow) \tag{3.13}$$

  is valid.

---

[1] It is also possible to get overlapping bands: $E_n(\mathbf{k}) = E_{n+1}(\mathbf{k}')$, $\mathbf{k} \neq \mathbf{k}'$

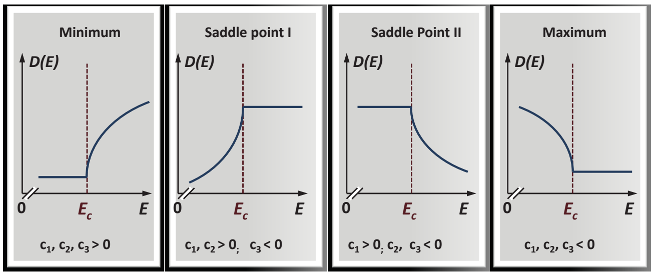

Figure 3.4: Qualitative course of the density of states $D(E)$ close to critical points. The energy at the critical point is E_c [19].

3.2.2 Density of States

By knowing the surface of constant energy $E(\mathbf{k}) = \text{const.}$, it is possible to calculate the density of states (DOS) of a crystal.

The DOS $D(E)$ in energy space can be calculated with

$$2\frac{V}{(2\pi)^3}\int_{\mathbf{k}(E)}^{\mathbf{k}(E+\Delta E)} d^3k = \int_{E(\mathbf{k})}^{E(\mathbf{k}+\Delta E)} D(E)dE \approx D(E)\Delta E \tag{3.14}$$

and the known dispersion relation $E(\mathbf{k})$, resulting in

$$D(E) = 2\frac{V}{(2\pi)^3}\int_{E(\mathbf{k})=\text{const.}} \frac{dS_E}{|\nabla_{\mathbf{k}}E(\mathbf{k})|}. \tag{3.15}$$

Here, dS_E is a surface element of the surface of constant energy $E(\mathbf{k}) = E$ and $\nabla_{\mathbf{k}}E(\mathbf{k}) = \frac{dE(\mathbf{k})}{dk_\perp}$, with $dk_\perp$ being perpendicular to dS_E.

For free electrons, the surfaces of constant energy are spherical surfaces and the dispersion relation is given by $E(\mathbf{k}) \propto k^2$. For crystal electrons, the surfaces of constant energy can be much more complicated. Especially for $\mathbf{k}$-space points, with $|\nabla_{\mathbf{k}}E(\mathbf{k})| = 0$, i.e., the curve of the dispersion relation $E(\mathbf{k})$ is flat, the DOS gets a rich structure. These points are called critical points. For 3D-systems, an expansion of $E(\mathbf{k})$ at these points provides always $E(\mathbf{k}) \propto k^2$. This implies that $|\nabla_{\mathbf{k}}E(\mathbf{k})|^{-1}$ has an $\frac{1}{k}$ singularity and the integral over the surface $E(\mathbf{k}) = \text{const.}$ has a linear k-dependency.

The form of $D(E)$ close to a critical point is shown in fig. 3.4. Close to the critical point, the dispersion can be written as

$$E(\mathbf{k}) = E_c + \sum_{i=1}^{3} c_i(k_i - k_{ci})^2. \tag{3.16}$$

Here, E_c is the energy at the critical point and c_i are constants, which have different signs depending on the type of critical point (minimum, maximum, or saddle point). The resulting DOS are:

$$\begin{aligned}
D(E) &= D_0 + C\sqrt{E - E_c}, & c_1, c_2, c_3 &> 0, & &\text{minimum} & &\text{(3.17a)}\\
D(E) &= D_0 - C\sqrt{E_c - E}, & c_1, c_2 > 0, c_3 &< 0, & &\text{saddle point I} & &\text{(3.17b)}\\
D(E) &= D_0 - C\sqrt{E - E_c}, & c_1 > 0, c_2, c_3 &< 0, & &\text{saddle point II} & &\text{(3.17c)}\\
D(E) &= D_0 + C\sqrt{E_c - E}, & c_1, c_2, c_3 &< 0, & &\text{maximum} & &\text{(3.17d)}
\end{aligned}$$

3.3 Dynamics

The previous section introduced band electrons by assigning each electron to the energy states of the bands. This section will now use the properties of these band electrons to describe how they behave under the influence of external forces and more specificly under the effect of an external electrical field.

3.3.1 Semiclassical Model

To describe the dynamics, the following rules will be applied:

1. **Bandindex:** The bandindex n is a constant of motion, i.e. there are no band-band transitions described.
2. **Equations of motion:** In section 3.2.1, the velocity of the crystal electron was already defined by eq. (3.11). The change of energy δE through an external force can be described by

$$\delta E = \delta \mathbf{F} \cdot \mathbf{v} \delta t. \tag{3.18}$$

   On the other hand, using eq. (3.11) leads to

$$\delta E = \frac{\partial E_n(\mathbf{k})}{\partial \mathbf{k}} \cdot \delta \mathbf{k} = \hbar \mathbf{v}_n(\mathbf{k}) \cdot \delta \mathbf{k}. \tag{3.19}$$

   Therefore, to describe the time evolution of the spatial coordinate and the wave-vector, the equations of motion can be used:

$$\frac{d\mathbf{r}}{dt} = \mathbf{v}_n(\mathbf{k}) = \frac{1}{\hbar}\frac{\partial E_n(\mathbf{k})}{\partial \mathbf{k}} \tag{3.20a}$$
$$\hbar\frac{d\mathbf{k}}{dt} = \mathbf{F}(\mathbf{r}, t) = -e\left[\mathbf{E}(\mathbf{r}, t) + \mathbf{v}_n(\mathbf{k}) \times \mathbf{B}(\mathbf{r}, t)\right]. \tag{3.20b}$$

3. **Effective mass:** Using eqs. 3.20a and 3.20b leads to

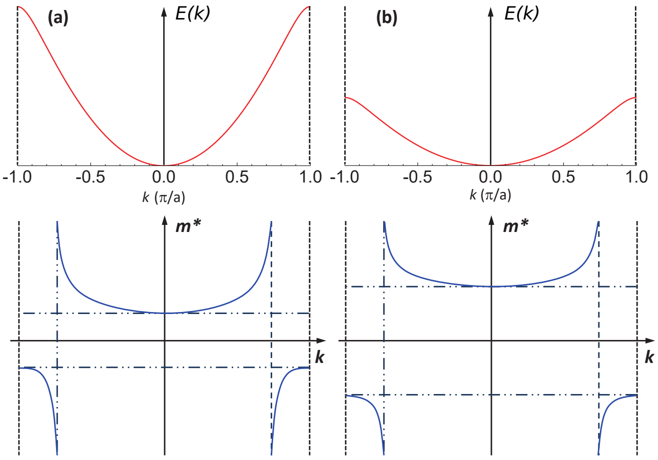

Figure 3.5: Schematic course of the band structure (top) and the effective mass (bottom): (a) A strong band-curvature results in a small effective mass. (b) A weak band-curvature results in a big effective mass [19].

$$\frac{d\mathbf{v}_n(\mathbf{k})}{dt} = \frac{1}{\hbar}\frac{d}{dt}\left(\frac{\partial E_n(\mathbf{k})}{\partial \mathbf{k}}\right) = \frac{1}{\hbar}\sum_{j=1}^{3}\frac{\partial^2 E_n(\mathbf{k})}{\partial k_i \partial k_j}\frac{dk_j}{dt} \tag{3.21a}$$

$$= \frac{1}{\hbar^2}\sum_{j=1}^{3}\frac{\partial^2 E_n(\mathbf{k})}{\partial k_i \partial k_j}F_j \tag{3.21b}$$

Equation 3.21b is equal to the classical equation of motion $\dot{\mathbf{v}} = m^{-1}\mathbf{F}$, if the scalar mass m is substituted by the effective-mass tensor:

$$[(m^*)^{-1}(\mathbf{k})]_{ij} = \frac{1}{\hbar^2}\frac{\partial^2 E_n(\mathbf{k})}{\partial k_i \partial k_j}. \tag{3.22}$$

This tensor represents a dynamic mass of the crystal electrons. It is given by the curvature of the band structure $E_n(\mathbf{k})$. Since the effective mass tensor m^*_{ij} and its inverse tensor $[(m^*)^{-1}(\mathbf{k})]_{ij}$ are symmetrical, it is possible to transform m^*_{ij} on the main axis. In the easiest case, if the three effective masses in all main axis directions are equal, it is

$$m^*_{ij} = \frac{\hbar^2}{d^2E_n(\mathbf{k})/dk^2}. \tag{3.23}$$

This holds true, e.g., at the top edge or under edge of a band. Here, the band can be described by an isotropic parabolic behavior:

$$E(\mathbf{k}) = E_0 \pm \frac{\hbar^2}{2m^*}(k_x^2 + k_y^2 + k_z^2). \tag{3.24}$$

Close to such a critical point, the effective mass is a constant and hence very useful. Further away, the band structure is deviating from the parabolic form and getting $\mathbf{k}$-dependent. Figure 3.5 shows the typical course of two one-dimensional bands $E_n(k)$ with strong and weak curvature. Therefore, the effective mass is respectively small or big. At the boundary of the BZ, the curvature is negative resulting in a negative effective mass. Using the effective mass, it is possible to describe the motion of band electrons like the motion of free particles. The interaction with the periodic lattice potential is part of the effective, **k**-dependent mass.

4. **crystal momentum:** The wave-vecor **k** is only well defined up to an reciprocal lattice vector **G**. If two electrons are sharing the same position and the same band and their wave-vectors differ only by **G**, they are indistinguishable. The equations of motion for crystal electrons correspond to the equations of motion for free electrons, with the exception that $E_n(\mathbf{k})$ represents the energy and not $\frac{\hbar^2\mathbf{k}^2}{2m}$. Nonetheless, $\hbar\mathbf{k}$ is not the momentum of the Bloch-electrons. It is only its quasi momentum. The time change of the momentum is given by all forces influencing the electron. The change of $\hbar\mathbf{k}$ is only given by the external forces and not by the forces from the periodic lattice-potential.

5. **Fermi statistics:** In thermal equilibrium, the contribution to the electronic DOS of electrons from band n with wave-vectors in the volume element d^3k is given by

$$2\frac{V}{(2\pi)^3}d^3kf[E_n(\mathbf{k}),T] = \frac{V}{4\pi^3}\frac{d^3k}{e^{[E_n(\mathbf{k})-\mu]/k_BT}+1} \tag{3.25}$$

3.3.2 Motion of Crystal Electrons

This subsection will treat the motion of crystal electrons under the following conditions:

- only one band is treated (ignoring bandindex n)
- f(E,T)=f(E,T=0)

Filled Bands

To calculate the particle-current density **J**, the contribution $d\mathbf{J}$ of electrons with wave-vectors from the region d^3k is needed. With the DOS $\frac{1}{4\pi^3}$ in **k**-space for both spin directions, it leads to

$$d\mathbf{J} = \mathbf{v}(\mathbf{k})\frac{1}{4\pi^3}d^3k = \frac{1}{4\pi^3\hbar}\nabla_{\mathbf{k}}E(\mathbf{k})d^3k. \tag{3.26}$$

To get the total particle-current density, an integration over the 1st BZ is necessary. For the electrical current density $\mathbf{J}_q = -e\cdot\mathbf{J}$ follows

$$\mathbf{J}_q = \frac{-e}{4\pi^3\hbar}\int_{1^{\mathrm{st}}\ \mathrm{BZ}}\nabla_{\mathbf{k}}E(\mathbf{k})d^3k. \tag{3.27}$$

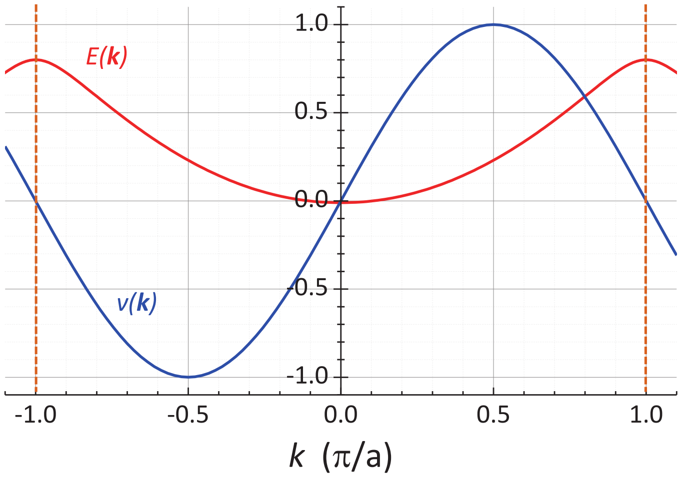

Figure 3.6: Course of $E(\mathbf{k})$ and $\mathbf{v}(\mathbf{k})$ as functions of $\mathbf{k}$ or, equally, as functions of time, since $\mathbf{k}(t) \propto t$. The course in one dimension corresponds to direction parallel to one reciprocal lattice-vector [19].

This integral is done over the gradient of the periodic functions $E(\mathbf{k}) = E(\mathbf{k}+\mathbf{G})$ which gives zero. So, the conclusion is:

> The electrical current in a filled band vanishes. Electrical current is only possible by electrons in partly filled bands.

Partly Filled Bands

The contribution to the current density of occupied electron states in a band is given by

$$\mathbf{J}_q = \frac{-e}{4\pi^3\hbar} \int_{\text{occupied}} \nabla_{\mathbf{k}} E(\mathbf{k}) d^3k \tag{3.28}$$

Contrary to to a filled band, $\mathbf{J}_q$ does not have to be zero. The current density is only vanishing in thermal equilibrium because, here, for every $\mathbf{v}(\mathbf{k})$ exists a $-\mathbf{v}(-\mathbf{k})$, which lets the integral vanish. But, if there is an external perturbation (e.g. an electrical field) a redistribution is happening which leads to a non-vanishing current density.

If a band is partly filled, an electrical field leads to a change in the velocity distribution of the electrons. For the time change of the wave-vector follows

$$\mathbf{k}(t) = \mathbf{k}(0) + \frac{e\mathbf{E}}{\hbar} t. \tag{3.29}$$

So for the velocity applies

$$\mathbf{v}(\mathbf{k},t) = \mathbf{v}\left(\mathbf{k}(0) + \frac{e\mathbf{E}}{\hbar} t\right). \tag{3.30}$$

Since $\mathbf{v}(\mathbf{k})$ is a periodic function in $\mathbf{k}$-space, $\mathbf{v}(\mathbf{k},t)$ is a bounded function in time. If the electrical field $\mathbf{E} \parallel \mathbf{G}$, $\mathbf{v}(\mathbf{k},t)$ is a periodic function (see fig.3.6), the velocity vanishes, i.e., the acceleration of the electron is oppositely directed to the external force, at the zone boundary. This is a consequence of the lattice forces influencing the electron.

Without scattering processes, the wave-vector of the electron would grow continuously. In this case, the crystal electron would travel a distance in **k**-space which is larger than the 1^{st} BZ which would lead to an oscillating velocity. A external electrical field would lead to an oscillating electron motion, i.e. alternating current. This phenomenon is called Bloch-oscillation. Without scattering processes, there would be no directed current along the external electrical field.

Electrons and Holes

For a completely filled band $\mathbf{J}_q = 0$. Writing the integration over the occupied states as a difference of an integral over the whole BZ and an integral over the un-occupied states leads to

$$\mathbf{J}_q = \underbrace{\frac{-e}{4\pi^3\hbar}\int_{1^{\text{st}}\ \text{BZ}} \nabla_{\mathbf{k}} E(\mathbf{k}) d^3k}_{=0} - \frac{-e}{4\pi^3\hbar}\int_{\text{un-occupied}} \nabla_{\mathbf{k}} E(\mathbf{k}) d^3k \tag{3.31}$$

$$= \frac{+e}{4\pi^3\hbar}\int_{\text{un-occupied}} \nabla_{\mathbf{k}} E(\mathbf{k}) d^3k \tag{3.32}$$

The current-contribution of the occupied electron-states of a band is equal to the current of free states filled with positively charged charge-carriers. So, it can be advantageous to assume that the current is done by virtual positively charged particles, even when there are only negatively charged electrons existing in a solid body. These virtual charge carriers are called holes or defect-electrons.

The concept of holes is useful at the upper edge of a band. This will be visualized by a band with a maximum $E(\mathbf{k}_0)$ at $\mathbf{k}_0$ close to the Fermi level. The negative curvature at the maximum resulst in a negative effective mass. Close to the maximum, the band can be apporached by a parabolic course:

$$E(\mathbf{k}) = E(\mathbf{k}_0) - c(\mathbf{k} - \mathbf{k}_0)^2 \tag{3.33}$$

Here, c is a positive constant, which determines the effective mass (see section 3.3.1 point 3)

$$m^* = \frac{\hbar^2}{d^2E_n/dk^2} = -\frac{\hbar^2}{c} < 0 \tag{3.34}$$

So, m^* is negative, since c is a positive constant. Now, to all wave-vectors close to $\mathbf{k}_0$,

$$\mathbf{v}(\mathbf{k}) = \frac{1}{\hbar}\frac{\partial E}{\partial \mathbf{k}} = -\frac{2c}{\hbar}(\mathbf{k} - \mathbf{k}_0) \tag{3.35}$$

can be applied and, therefore,

$$\frac{d}{dt}\mathbf{v}(\mathbf{k}) = -\frac{2c}{\hbar}\frac{d}{dt}\mathbf{k} \propto -\dot{\mathbf{k}}. \tag{3.36}$$

The acceleration is anti-parallel to $\dot{\mathbf{k}}$ and, therefore, anti-parallel to the active force. Using the equation of motion 3.20b, the electron close to a band maximum reacts on external fields as it would have a negative effective mass. Changing the sign of both sides of eq. (3.20b) shows that the equation of motion describes the motion of a positively charged particle with positive effective mass.

> An electron with negative effective mass reacts on external fields like a positively charged particle with a positive effective mass.

Bands which show a maximum at the Fermi level are called hole bands and bands with a minimum at the Fermi level are called electron bands, correspondingly.

3.4 Scattering Processes

In the previous sections, the motion of free electrons and crystal electrons was described. Already in the definition of the electrical conductivity in section 3.1, scattering processes were mentioned, which change the electron momentum by a average scattering time τ. But so far, the origin of these scattering processes was not mentioned, although they are of high importance for electrical resistance. This section will treat the most important scattering processes in solid bodies.

The original assumption was, that electrons get scattered at the positively charged atomic-cores[2]. As was shown in section 3.3.2, this is not true. An exact periodic arrangement of atoms in a crystal does not cause scattering processes. The periodic lattice potential is included in the description of Bloch-waves, which are stationary solutions of the Schrödinger equation. Since $|\Psi|^2$ is time-independent, these solutions describes undisturbed propagation of electron-waves. Scattering processes are only possible by disturbing the propagation of stationary Bloch-waves. This is possible in different ways. Some of them are mentioned here:

1. **Deviations from the Strict Periodicity of the Lattice:**

---

[2] An image which was still taught in german elementary schools, at least until 1998, possibly even until today.

   a) Crystal defects, e.g. surface defects, dislocations, impurities, etc.: These defects are spatially fixed and can usually be treated as time-independent.

   b) Phonons: These are time-dependent deviations of the strict periodicity.

2. **Electron-Electron-Scattering:** Scattering processes between electrons can disturb the stationary Bloch-waves, but the probability of such processes is much smaller than for the two effects mentioned before.

3. **Electron-Magnon-Scattering:** In magnetically ordered materials, the electron spins are aligned, parallel for ferromagnets and anti-parallel for anti-ferromagnets. At finite temperatures, this state receives energy and some spins flip. This deviation of the periodicity of the spins can wander as a spin-wave through the crystal. Such spin-waves existing at $T > 0$ are called magnons. Magnons are deviations of the ordered spins. Electrons can scatter at these deviations, leading to a typical resistance behavior in dependency of temperature. For ferromagnets this behavior is

   $$\rho \propto T^2. \tag{3.37}$$

   The scattering at magnons in magnetically ordered systems can only happen below the ordering temperature. Therefore, the occurrence of the typical resistance behavior, as an anomaly of the resistivity curve below a specific temperature, can indicate a magnetic transition.

In the following subsections the discussion will concentrate on scattering processes from type 1 and 2.

3.4.1 Scattering Cross Sections

Different types of scattering centers can be characterized by their density n_s and their scattering cross sections S. The free mean path is given by

$$\frac{1}{l} = n_s S. \tag{3.38}$$

If in a sample different scattering processes are present and are independent from each other, the cross sections can be weighted with its densities and can be summed:

$$l^{-1} = \sum n_{Si} S_i. \tag{3.39}$$

The inverse free mean path is proportional to the resistivity. So, the total resistivity ρ is the sum of all single-resistivities ρ_i caused by independent mechanisms:

$$\frac{1}{l} = \frac{1}{l_1} + \frac{1}{l_2} + \frac{1}{l_3} + \cdots \tag{3.40a}$$

$$\rho = \rho_1 + \rho_2 + \rho_3 + \cdots \,. \tag{3.40b}$$

This is called Matthiesen's rule [22].

Both, scattering density and cross section can be temperature-dependent. In the following the single scattering mechanisms are discussed.

3.4.2 Electron-Phonon-Scattering

The scattering rate for electron-phonon scattering is proportional to the average number of phonons $\langle n \rangle$. It is proportional to T^3 at low temperatures ($T \ll {\Theta_D}^3$) and proportional to T for high temperatures ($T \gg \Theta_D$). This leads to the following temperature dependency of the electrical resistivity:

1. For high temperatures: Since $\frac{1}{\tau_{\text{ph}}} \propto \langle n \rangle \propto \frac{T}{\Theta_D}$,

$$\rho_{\text{ph}} \propto T. \tag{3.41}$$

2. For low temperatures: Additionally to the number of phonons, which is $\langle n \rangle \propto T^3$ at low temperatures, a weighting factor influences the scattering behavior, which weights the scattering depending on the scattering direction. For low temperatures, this weighting factor is $\propto T^2$. So in the end, it leads to

$$\rho_{\text{ph}} \propto T^5. \tag{3.42}$$

3.4.3 Scattering at Impurities

The number of defects and impurities in a sample is independent of temperature. Therefore, scattering at impurity-atoms provides a temperature-independent contribution to the resistivity. This contribution is called residual resistivity:

$$\rho_0 = \text{const.} \tag{3.43}$$

---

[3] Θ_D is the Debye Temperature. It is a measure of the number of phonon frequencies in a material. For temperatures below the Debye temperature phonon modes freeze and the number of frequencies decreases.

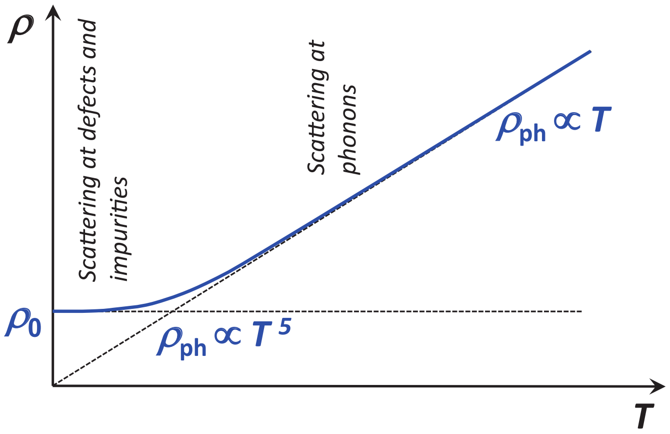

Figure 3.7: Temperature dependency for the resistivity of a typical metal. At low temperatures the scattering at defects and impurities is dominating, at high temperatures it is phonon scattering[19].

A quantity which is usually taken to characterize the purity of conducting materials is the so called residual resistivity ratio (RRR):

$$RRR = \frac{\rho(300\,\mathrm{K})}{\rho_0}. \tag{3.44}$$

For many pure materials, the resistivity at 300 K is dominated by electron-phonon-scattering and at the same time the residual resistivity is getting very small, due to missing impurity atoms. Therefore, very high RRR-values up to 10^6 are possible.

3.4.4 Electron-Electron-Scattering

For electron-electron-scattering, the conservation of energy and momentum have to be valid too. So, by scattering of two electrons from the states 1 and 2 into the states 3 and 4

$$E_1(\mathbf{k}_1) + E_2(\mathbf{k}_2) = E_3(\mathbf{k}_3) + E_4(\mathbf{k}_4) \tag{3.45a}$$

$$\mathbf{k}_1 + \mathbf{k}_2 = \mathbf{k}_3 + \mathbf{k}_4 + \mathbf{G} \tag{3.45b}$$

have to be valid. Here $E_i(\mathbf{k}_i)$ are the one-particle-energies of the non-interacting electron system.

Naively, a very high probability for electron-electron-scattering would be expected, since there is one electron per unit cell, which is a high density and there should be strong Coulomb repulsion. However, the Pauli principle is suppressing the electron-electron-scattering strongly. To perform the scattering of electron 1 and 2, the states 3 and 4 have to be empty to fulfill the Pauli principle, i.e., E_3 and E_4 can not be further above E_F than k_BT. So,

$$E_1 + E_2 = E_3 + E_4 \geq 2E_F - 2k_BT. \tag{3.46}$$

Since the occupation-probability below E_F is strongly reduced, the energies E_1 and E_2 can

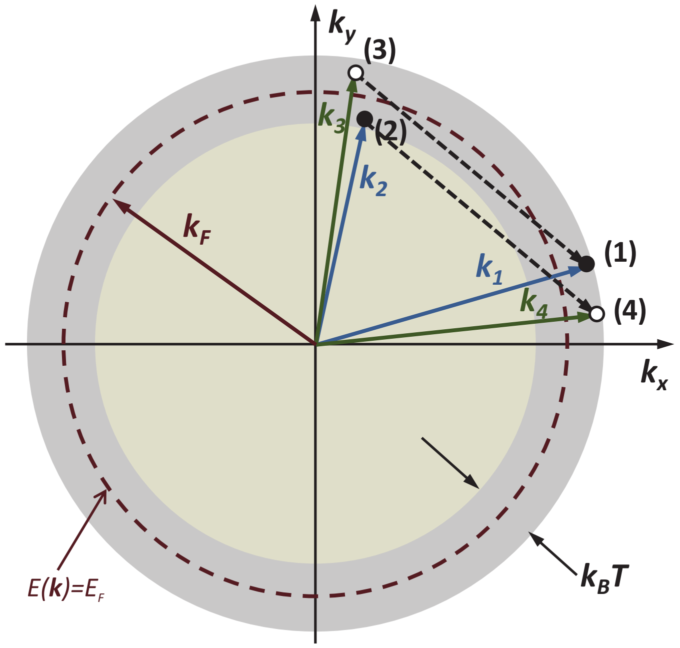

Figure 3.8: Visualization of electron-electron-scattering in **k**-space. Both electrons (1) and (2) with wave-vectors $\mathbf{k}_1$ and $\mathbf{k}_2$ scatter at each other and end up in states (3) and (4) with wave-vectors $\mathbf{k}_3$ and $\mathbf{k}_4$. The Pauli principle demands that the states (3) and (4) have to be empty[19].

not lie further above E_F than k_BT. Together with 3.46 it can be concluded that, only electrons 1 and 2 are useable for electron-electron-scattering processes which are within $\pm k_BT$ around the Fermi energy, i.e., only a small part of $\frac{k_BT}{E_F}$ of all electrons can participate in electron-electron-scattering.

Since E_1 and E_2 lie within a tiny shell of width $\pm k_BT$ around the Fermi energy, eq. (3.45b) and eq. (3.46) demand that also the energies E_3 and E_4 have to be within a tiny shell of width $\pm k_BT$ around E_F. Figure 3.8 visualizes the electron-electron-scattering in **k**-space. The conservation of **k**, i.e., $\mathbf{k}_1 - \mathbf{k}_3 = \mathbf{k}_2 - \mathbf{k}_4$ demands that the connection lines (1)-(3) and (2)-(4) in fig. 3.8 have to be equal. So, the Pauli principle reduces the scattering probability by the factor $\frac{k_BT}{E_F}$.

The reduced scattering probability for electron-electron scattering can be formulated as

$$P_{e-e}(T) = S_{e-e}\left(\frac{k_BT}{E_F}\right)^2 . \tag{3.47}$$

Here S_{e-e} is the scattering cross section for a classical gas of screened point charges.

Assuming S_{e-e} to have the same magnitude as the scattering cross section of an electron scattered at a charged core of an impurity and taking typical values for $E_F \simeq 10\,\text{eV}$ and $k_BT \simeq 10^{-4}\text{eV}$ at $T = 1\,\text{K}$, the electron-electron-scattering is by the factor 10^{-10} smaller than the electron-impurity-scattering.

In a simple one-band metal, this process plays a minor role, since it is quite small compared to the electron-phonon scattering. In a multi-band metal, like transition metals, the resistivity is dominated by the electron-electron scattering, since the different bands show differing effective masses and Fermi-velocities. Heavy bands with low velocities cross faster

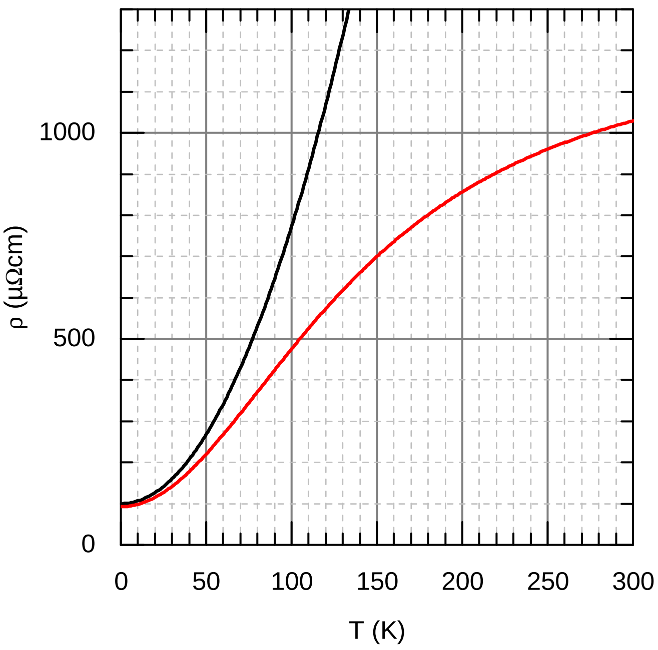

Figure 3.9: Example for resistivity dominated by electron electron scattering. In black is shown a quadratic temperature behavior of the resistivity as one would expect for electron electron scattering. In red is shown the same quadratic behavior with a limiting resistivity for high temperatures, as described by eq. (3.50). In both cases a residual resistivity is present at low temperatures.

and lighter bands. The quadratic temperature dependency of eq. (3.47) is then reflected in the resistivity curve:

$$\rho \propto T^2. \tag{3.48}$$

An example of such a curve is given in fig. 3.9.

3.5 Ioffe–Regel Criterion

The free mean path of an electron cannot become smaller than the order of the lattice constants, which was stated by Ioffe and Regel in 1960 [24] and is called the Ioffe–Regel criterion. The minimum free mean path l_0 can also be expressed as a minimum average colission time . Since the Ioffe–Regel criterion states that free mean paths smaller than l_0, or scattering times τ shorter than $\tau_0 = \frac{l_0}{v_F}$, are forbidden, the probability for a collision in a time t shorter than τ_0 is zero. To illustrate that, a random distribution of impurities can be taken (see fig. 3.10). The impurities cannot be closer to another than a minimum distance of the order of the lattice constants. After the scattering process of an electron, it has to travel at least for a time τ_0 to be scattered again. An electron can scatter at any time $t > \tau_0$ [23]. For calculating the change of the wave vectors of the electrons, the time t

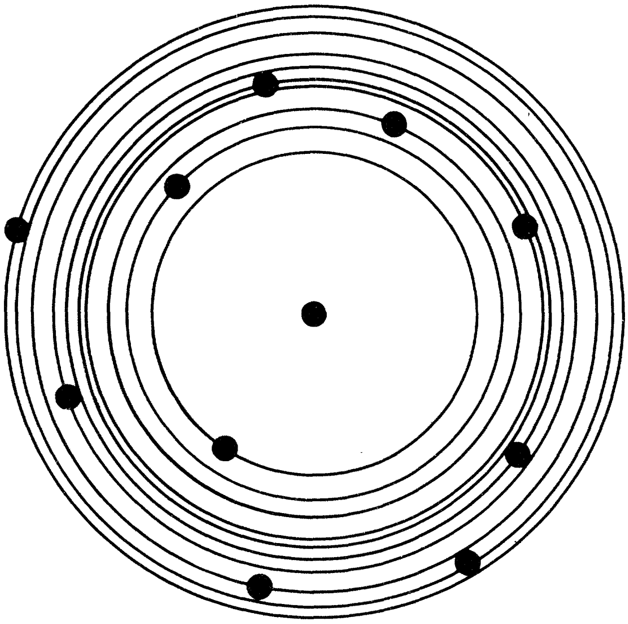

Figure 3.10: Randomly distributed impurities. Circles are drawn to indicate distances from a given impurity to its neighbors[23].

has to be replaced by $t - \tau_0$ and $\delta\mathbf{k}$ becomes $\delta\mathbf{k} = \frac{eE}{\hbar}(\tau - \tau_0)$. Thus, the conductivity σ is calculated by:

$$\sigma = \frac{e^2 n\tau}{m} + \frac{e^2 n\tau_0}{m} = \sigma_{\text{ideal}} + \sigma_{\text{lim}}. \tag{3.49}$$

Equation 3.49 is the conductivity of two parallel resistors. Therefore, the limiting resistivity ρ_{lim} can be described by the parallel resistor formula [25]

$$\frac{1}{\rho} = \frac{1}{\rho_{\text{ideal}}} + \frac{1}{\rho_{\text{lim}}}, \tag{3.50}$$

which describes properly the saturation of the resistivity at high temperatures (see fig. 3.9).

4 Properties of LiFeAs

LiFeAs is an iron pnictide superconductor (IPS) which is a class of unconventional superconductors based on iron compounds. The IPS are typically divided into four different families: the 1111-family, the 122-family, the 111-family, and the 11-family[1]. The name of each family is given by the stoichiometric composition of the parent compounds of its members. One famous member of the 1111-family is LaOFeAs (La1111), which was the first IPS in which a high superconducting transition temperature ($T_c = 26\,\mathrm{K}$) for fluorine-doped La1111 was detected in 2008 by Kamihara et al. [4]. This discovery lead to a tremendous amount of interest resulting in developments which established this class of materials.

LiFeAs (Li111) is a member of the 111-family with a T_c of 18 K [7–9]. It is a special kind of IPS because it shows properties which can only be observed for LiFeAs so far. The first difference compared to other IPS is that it is a stoichiometric superconductor, i.e. the parent compound is superconducting without any kind of doping. Most of the IPS need doping to develop superconductivity. So far, doping experiments on LiFeAs lead to an decrease of T_c, e.g. substituting Fe with Co or Ni [10, 11].

This chapter will give an overview on the properties of LiFeAs and IPS in general and is based on [26].

4.1 Crystal Structure

All IPS crystallize in a tetragonal structure (fig. 4.1). Iron and Arsenic[2] form tetrahedrons with Fe in the center and As at the corners. Together, these tetrahedrons form layers. Depending on the family, the FeAs-layers are intercalated by layers of other elements. In the 1111-family these interstitial layers are formed by tetrahedrons of lanthanide-oxides, for the 122-family there are layers of earth-alkali metals, for the 111-family there are alkali metals and for the 11-family there are no interstitial layers . The distance between the Fe atoms in the structure is rather short (up to 2.84 Å for 1111-IPS [29]). Therefore, the Fe-3d electrons can form bands and are made responsible for a high density of states at the Fermi

---

[1] The 11-family is actually consisting of Iron and elements from the oxygen group hence they should strictly speaking be treated as iron chalcogenide superconductors (ICS), but they are nevertheless included in the IPS.

[2] For 11-ICS there are Selenium or Tellurium

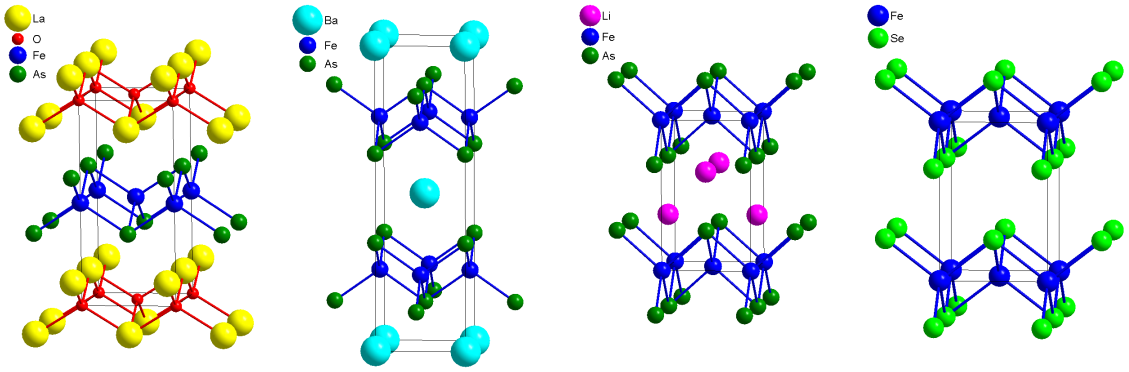

(a) 1111-LaOFeAs [4]
(b) 122-$BaFe_2As_2$ [27]
(c) 111-LiFeAs [6]
(d) 11-FeSe [28]

Figure 4.1: Crystal Structures of IPS. The layered structure of iron-arsenic/selenium tetrahedrons (green and blue spHere, s) is common for all IPS. Depending on the material they are intercalated with other elements or molecules.

energy [30]. Most IPS undergo a structural transition when cooled below a temperature T_s. At this temperature, the crystal structure changes from a tetragonal symmetry to an orthorhombic one.

Li111 does also form a tetragonal structure with the $P4/nmm$-symmetry group [6]. Here, the interstitial layers are formed by the alkali metal Lithium. Unlike most of the other IPS, LiFeAs does not show a structural transition temperature T_s.

4.2 Electronic Structure

Hirschfeld et al. [31] summarize the electronic structure of IPS as follows: There are two hole bands crossing the Fermi energy near the Γ-point (0,0), the center of the Brillouin zone (BZ), and two electron bands crossing close to the M-point, the corner of the BZ, $(\frac{\pi}{\sqrt{2}a},\frac{\pi}{\sqrt{2}a})$ with a being the lattice constant of the square plane in the $P4/nmm$-symmetry. The bands are formed by the Fe 3d-orbitals. The resulting electron and hole Fermi surfaces (FSs), called pockets, are well separated from each other (see fig. 4.2(a)). One phenomenon which is highly relevant for IPS is the nesting of the electron and hole pocket of the FS. If the shape of them is nearly the same, it is possible to connect all points on the hole pocket with points on the electron pocket by one single wave vector, which is called the nesting vector. The shape of the pockets depends strongly on the material and can reach from good nesting conditions,[3] e.g. Ba122 [32, 33], to bad nesting or no nesting,[4] at all, e.g. LiFeAs [34].

---

[3] i.e. same size of electron and hole pocket

[4] different size of the electron and hole pocket

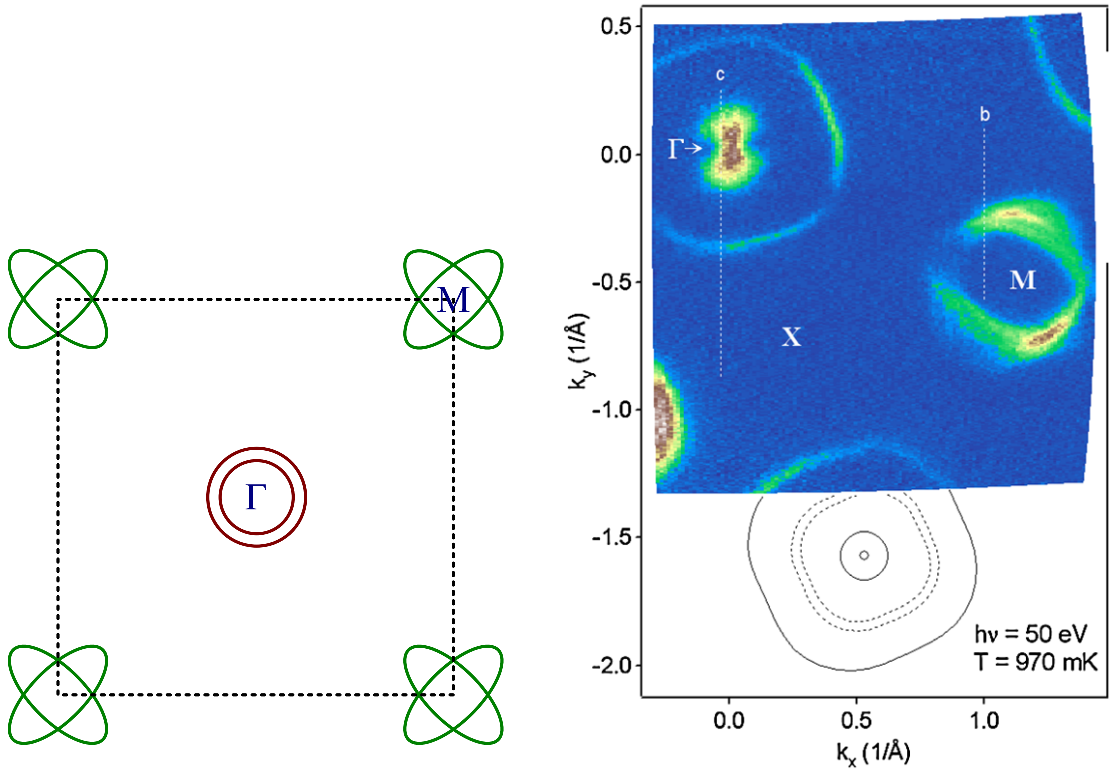

(a) Schematic 2D Fermi-surface of IPS. Electron bands in green and hole bands in red. The dashed line represents the zone boundaries. Reproduced from [31]

(b) Fermi surface of LiFeAs measured by ARPES [34]. The black solid and dashed lines compare the sizes of hole (solid) and electron (dashed) FS.

Figure 4.2: Fermi surfaces of IPS.

Many IPS show an antiferromagnetic (afm) spin density wave (SDW) and its wave vector is coinciding with the nesting vector. Therefore, nesting is thought to be responsible for the formation of the SDW [35]. Indeed, almost all IPS parent compounds, which show good nesting conditions, show an afm SDW transition below the Néel temperature with the same wave vector [36].

As already stated above, LiFeAs does not show nesting [34], i.e., the sizes of the hole and electron pocket of the FS differ from each other which can be seen very clearly in fig. 4.2(b). Since LiFeAs does not show any SDW transition, this was taken as a strong argument, that nesting might be indeed responsible for the formation of SDWs in IPS. In LiFeAs, there are not only two hole bands close to the Fermi level at the Γ-point, but three. In fig. 4.2(b) the most outward pocket, seen from the Γ-point, is formed by a band which is crossing the Fermi level. The butterfly-like structure very close to the Γ-point is formed by two hole like bands which form maxima directly below or above the Fermi level, depending which k_z is taken for FS (see fig. 4.3(c)). In fig. 4.3(a) is shown the threedimenional FS of LiFeAs extracted

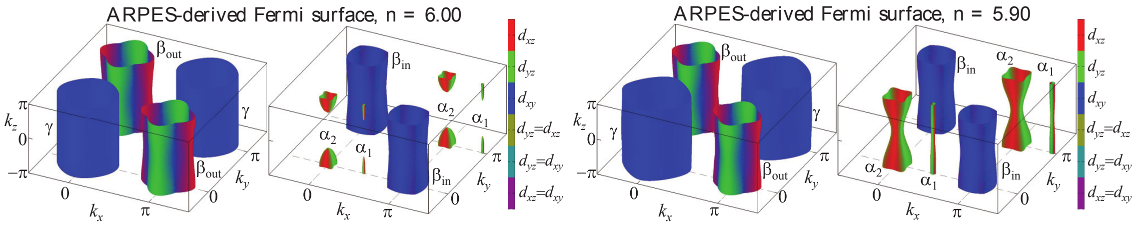

(a) filling $n = 6.00$ corresponds to stoichiometric LiFeAs

(b) filling $n = 5.90$ corresponds to hole-doped LiFeAs

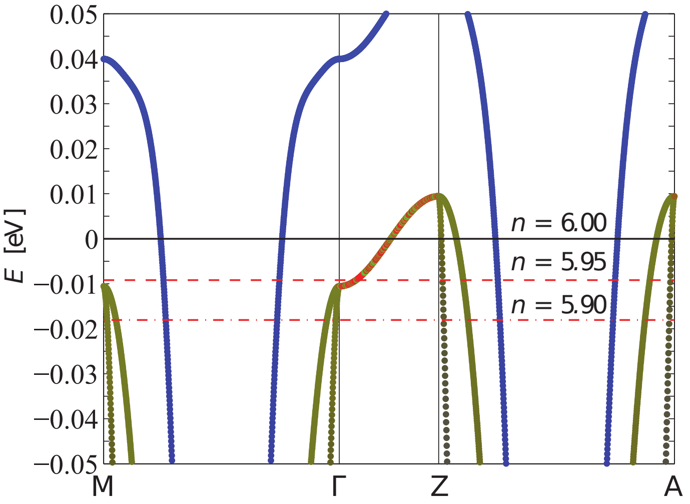

(c) Model derived band structure along the $M - \Gamma - Z - A$ path.

Figure 4.3: Fermi surface of LiFeAs from ten-orbital ARPES calculations at different fillings plotted in the coordinates of the one-Fe BZ as two sets, outer (left) and inner (right) pockets. Majority orbital weights are labeled as shown. Note the smallest inner most hole pocket α_1 with rotation axis $\Gamma - Z$ ($M - A$) has been artificially displaced from its position along the k_x axis for better viewing [37].

from model band calculations [37] of ARPES-measurements [38]. The α-hole pockets are detached regions around the Z point $(0,0,\frac{\pi}{a})$ (see fig. 4.3(a)), since the hole bands do not cross the Fermi level for all k_z.

Maxima in the band structure are called critical points, as $\nabla_k E = 0$, like the maxima of the α-bands. Since the density of states (DOS) is proportional to the inverse of $\nabla_k E$ (see section 3.2.2), a critical point in the band structure has a high DOS. So due to the close vicinity of the α-band maxima to the Fermi level, there is a high DOS close to the Fermi level. By lowering the Fermi level, the critical points of the hole-bands would cross the Fermi level for every k_z, which would result in the connection of the detached pockets to a barrel like structure along Γ-Z (see fig. 4.3(b)) Critical points of the hole bands close

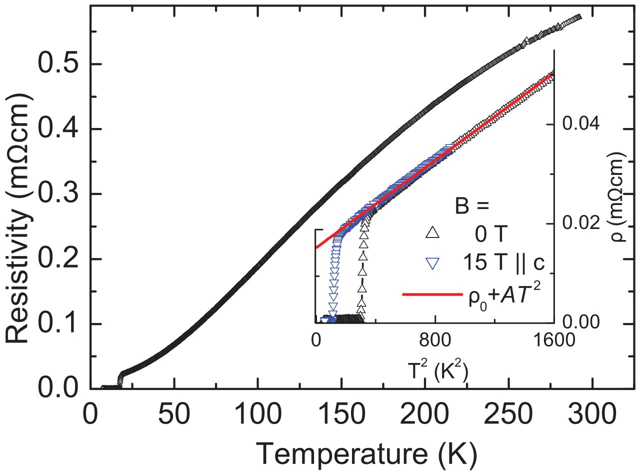

Figure 4.4: In-plane resistivity of LiFeAs as a function of temperature. The inset displays the low-temperature zero-field resistivity and $\rho(T)$ measured at 15 T together with a quadratic fit (line) representing ρ vs. T^2 [39]

to the Fermi level are a commonality of LiFeAs with every optimally doped, i.e. highest T_c, IPS [34, 35]. Therefore, Kordyuk [35] argument the distance of these maxima to the Fermi level is the key to develop a superconducting dome (see section 4.4).

4.3 Superconductivity

Superconductivity is by far the most prominent property of the IPS. Below its transition temperature, the resistivity of a superconductor vanishes (see fig. 4.4). It is caused by an interaction between the conduction electrons. By this interaction the electrons are forming pairs and the pair building causes a energy gap close to the Fermi level. As the pair is a bosonic state, the Pauli principle is not valid here. Therefore, it is possible for all pairs to occupy one macroscopic wave-function. To excite the electrons into higher energy levels, it is necessary to overcome the pair binding energy and break the pairs. As was explained in chapter 3, the origin of resistivity are scattering processes of the electrons close to the Fermi energy. So, to cause resistivity, the scattering processes would need to overcome the energy gap, to break the pairs. This is only possible, if the scattering margin is bigger than the superconducting gap. The scattering margin is proportional to the temperature of the sample and the gap is proportional to the critical temperature T_c. So, resistivity is only possible, if the temperature of the sample exceeds T_c.

For conventional superconductors the interaction between the conduction electrons is mediated by phonons. For unconventional superconductors, like IPS, the origin of the interaction is still not known. For IPS, the most favored interaction to mediate the pair building are afm fluctuations, also for LiFeAs [37, 40–42]. These fluctuations would favor an anti-parallel alignment of the electron-spins in the superconducting pair. The pairs are forming singlets. The total spin of the pair would therefore vanish.

The superconducting gap function is depending on the wave-vector. Therefore its mag-

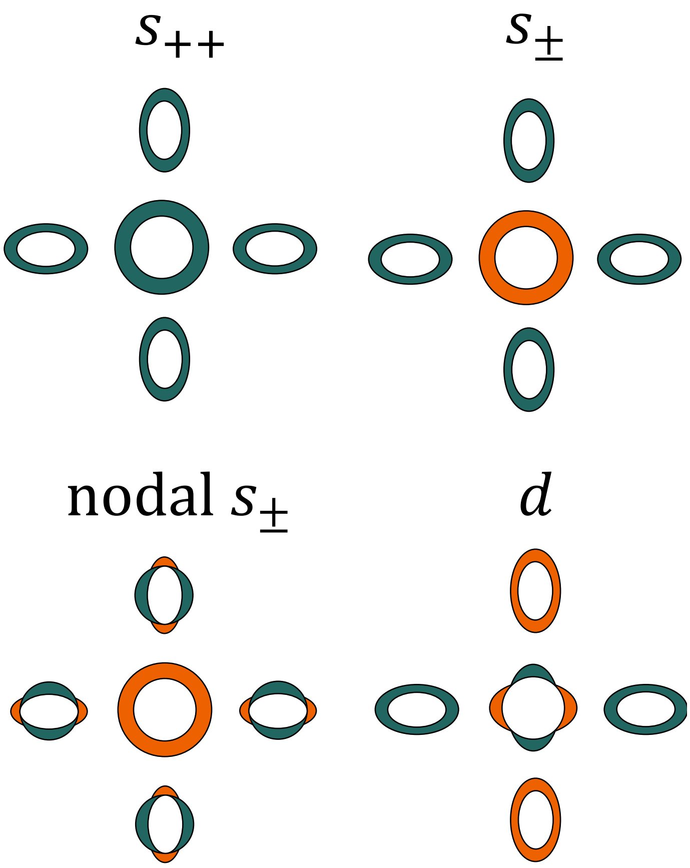

Figure 4.5: Gap function symmetries in discussion for iron pnictide superconductors mediated by antiferromagnetic fluctuations. The colors denote different signs of the gap function [31].

nitude and sign may vary along the FS. This variation is called the gap symmetry. For singlet superconductivity in IPS, four different symmetries are in discussion. The s_{++}, $s_{\pm}$, the nodal $s_{\pm}$, and the d-wave symmetry. Their properties are visualized in a cartoon in fig. 4.5. Most popular are the two $s_{\pm}$-symmetries[31, 37].

But not only afm fluctuations are discussed. Brydon et al. [12] predict that LiFeAs is close to a transition to ferromagnetism. They conclude that, ferromagnetic (fm) fluctuations might be responsible for the pair building. These type of fluctuations favors a parallel alignment of electron-spins in the pair. Thus, the total spin would be one and the two electrons would form a triplet state. A triplet superconductor would show a finite spin susceptibility below the superconducting transition temperature. Measurements of the ^{75}As-NMR Knight-shift, which probes the static spin susceptibility at an exchange vector $q = 0$, show indeed a finite spin susceptibility below the transition temperature for specific orientations of the crystal [43] (see section 4.5).

4.4 Doping Behavior

To get further information on a material, doping is a typical method. This is the process of inserting impurity elements, called dopants, into a substance to alter its physical properties. The compound without dopants is then called the parent compound. By exchanging atoms in the lattice by materials which have fewer or more valence electrons the process is called hole or electron-doping respectively.

The parent compounds of IPS are typically not superconducting. When cooled down, they undergo a structural transition as mentioned in section 4.1 and subsequently they develop an afm SDW below T_{SDW}. The structural transition temperature T_s is usually higher than T_{SDW} for 1111-compounds (e.g. La1111 [44, 45]) or they coincide with each other as in 122-compounds (e.g. $\mathrm{BaFe_2As_2}$ (Ba122) [27]).

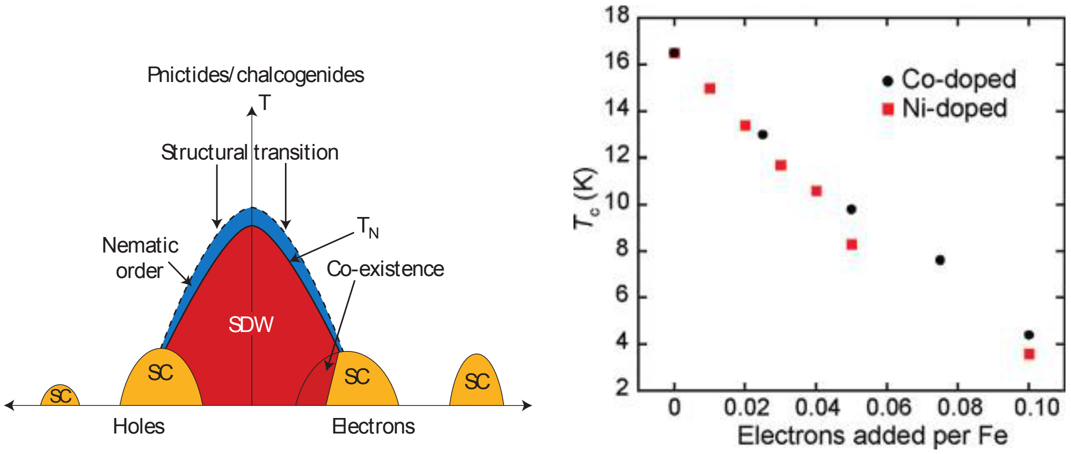

(a) Schematic phase diagram of IPS [46]

(b) Doping behavior of LifeAs [10]

Figure 4.6: Comparison of the schematic phase diagram of the IPS with the doping behavior of LiFeAs.

When doped with electrons (e.g. exchanging F with O in $\mathrm{LaO_{1-x}F_xFeAs}$) or holes (e.g. exchanging K with Ba in $\mathrm{Ba_{1-x}K_xFe_2As_2}$), both T_s and T_{SDW} are reduced and on further doping they are suppressed completely. While the structural transition and the SDW-phase get suppressed a superconducting phase is established. Depending on the material, the superconducting phase is either coexisting, e.g. Ba122 [47], with the magnetic SDW-phase or not, e.g. La1111 [48]. For higher doped superconducting IPS, there is no structural transition present anymore, and the material stays in the tetragonal structure. The critical temperature T_c of the superconducting phase is usually increasing on doping until it reaches a maximum.

In fig. 4.6 is shown a comparison of the schematic phase diagram of the IPS and the doping behavior of LiFeAs. LiFeAs behaves completely different from the other IPS: It is a stoichiometric superconductor. Furthermore, there is no structural or magnetic transition present and T_c is suppressed by electron doping, e.g. exchanging Co with Fe [10, 11](see fig. 4.6(b)).

This thesis is presenting data of joint experiments of the Leibniz Institute for Solid State

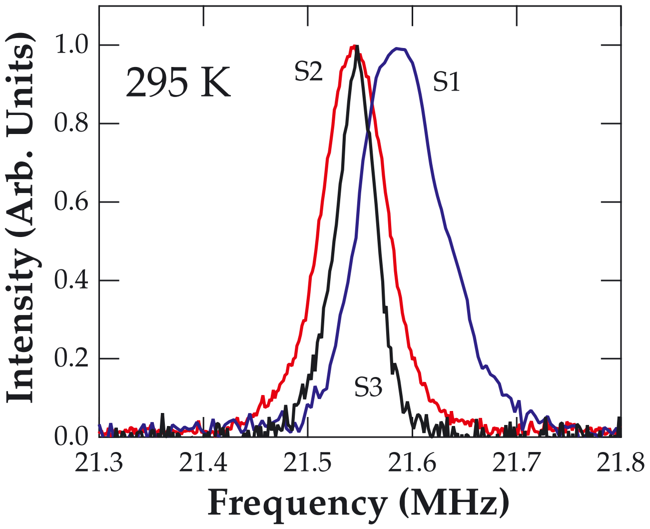

Figure 4.7: nuclear quadrupole resonance (NQR) spectra for stoichiometric LiFeAs. The NQR frequency of the sample S1 is noticeably larger than those of the samples S2 and S3 [43].

and Materials Research Dresden (IFW Dresden), the Technical University Dresden and, the University of Cologne, that state that off-stoichiometric LiFeAs with Li deficiency is developing a bulk fm phase. Because of the high relevance for the present work, this will be discussed in more detail in chapter 6.

4.5 Nuclear Quadrupole and Magnetic Resonance Measurements on LiFeAs

Studies with NQR and nuclear magnetic resonance (NMR) on LiFeAs are quite rare. They are done usually on the ^{75}As nucleus. The first measurements were published by Jeglič et al. [49]. They did Knight-shift K and spin-lattice relaxation rate T_1^{-1} measurements and determined the quadrupole frequency ν_Q on a polycrystalline sample of stoichiometric LiFeAs.

The Knight shift K is a shift of the resonance signal which is originated in small internal magnetic moments of the electron spins surrounding the nucleus. It gives gives information on the static spin susceptibility of the electrons for a interaction vector of $\mathbf{q} = 0$.

To measure the spin lattice relaxation rate T_1^{-1}, the nuclei are tilted out of their equilibrium states. The time they take to relax back is the relaxation time and its inverse is the relaxation rate T_1^{-1}. As the relaxation processes can only happen via interaction of the magnetic moment of the nucleus with the moments of the surrounding electrons of the lattice, the spin lattice relaxation rate T_1^{-1} is proportional to the $\mathbf{q}$-integrated dynamic spin susceptibility.

By comparing these two quantities with the Korringa-relation [50], Jeglič et al. [49] found signs of strong afm spin fluctuations.

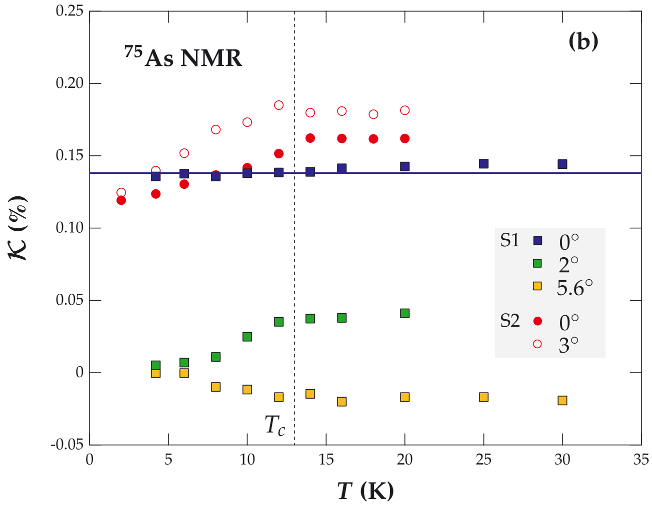

Figure 4.8: Knight shift K as a function of temperature for stoichiometric LiFeAs. S1: At low temperatures and for the magnetic field $H||ab$, K is constant across T_c. S2: K drops below T_c for both H parallel to the ab-plane and parallel to c [43]

Since ^{75}As has a spin of $\frac{3}{2}$, it has a spectrum consisting of a main peak and two satellite peaks. The distance between the two satellite peaks is proportional to the quadrupole frequency ν_Q. The calculated quadrupole frequency at room temperature of Jeglič et al. [49] is $\nu_Q = 21.35\,\text{MHz}$ and they also presented a temperature dependency of ν_Q.

Li et al. [51] published NQR and NMR measurements on polycrystalline LiFeAs. They found a $\nu_Q = 21.12\,\text{MHz}$ with a line width of $\approx 0.17\,\text{MHz}$ at $T = 20\,\text{K}$. They also performed K and T_1^{-1} measurements. Their T_1^{-1} data decreases with no coherence peak and a model of gaps with $s_\pm$-symmetry in presence of impurity scattering can be fitted to their data. Their Korringa-relation estimations show signs of only weak electron correlations.

Morozov et al. [52] used NQR as a method to confirm the quality of their LiFeAs single crystals. They were able to produce single crystals with a very narrow NQR spectrum (FWHM $= 64\,\text{kHz}$) at room temperature with $\nu_Q \approx 21.57\,\text{MHz}$. Such a small line width is exceptional for IPS and excludes deficiencies and anti-site disorder.

Baek et al. [43] reported an NMR and NQR study on three different LiFeAs crystals, labeled as S1, S2, and S3, from the same batch of single crystals. They found that they could distinguish the crystals by their, different NQR frequencies ($\nu_{\text{S1}} = 21.59\,\text{MHz}$ and $\nu_{\text{S2}} = \nu_{\text{S3}} = 21.54\,\text{MHz}$, fig. 4.7). Their crystals also showed very narrow line widths ranging from 60 kHz for S3 to 80 kHz for S1.

Not only could they distinguish the samples, they also found that the sample with the higher frequency (S1) shows an unexpected behavior in the NQR T_1^{-1} measurements and in the K measurements. In contrast to the low frequency samples (S2 and S3), S1 shows an increasing NQR $(T_1T)^{-1}$ below T_c and a constant K for the magnetic field parallel to the ab-plane also below T_c (fig. 4.8).

By other authors, their results are discussed to be a hint for spin triplet superconductivity [12], (see section 4.3). With these results, it was also shown that LiFeAs is very sensitive

Table 4.1: *RRR* of various publications

Publication	**year**	**RRR**
Wang et al. [57] polycrystal	2010	36
Song et al. [58]	2010	46
Lee et al. [59]	2010	24
Kim et al. [60]	2011	65
Zhang et al. [61]	2011	24
Heyer et al. [39]	2011	38
Khim et al. [62]	2011	20
Rullier-Albenque et al. [63]	2012	250

to small changes of its stoichiometry with quite dramatic effects on its properties and that these small changes can be distinguished with NQR spectroscopy.

On another crystal, Baek et al. [53] did detailed K measurements combined with measurements of the dynamic magnetic susceptibility (DMS). They conclude that the constant K below T_c is a sign of triplet superconductivity which occurs next to a singlet superconductivity resulting in two different superconducting transition temperatures.

4.6 Resistivity Measurements on LiFeAs

The first resistivity measurements on LiFeAs were published by Wang et al. [9] and Tapp et al. [8] on polycrystals. Both studies report superconductivity in LiFeAs at $T_c = 18\,\mathrm{K}$ for the first time [5]. Wang et al. [9] also report resistivity data on two nominally Li-deficient samples which show a reduced room temperature resistivity compared to the parent compound which decreases with decreasing amount of Li. Both Tapp et al. [8] and Wang et al. [9], show a metallic temperature dependency of the resistivity of LiFeAs, which is described by Wang et al. [9] as Pauli-metallic behavior.

Chu et al. [54] and Zhang et al. [55] report pressure- and temperature-dependent resistivity measurements on LiFeAs polycrystals. They show a linear decrease of T_c with increasing amount of pressure. Zhang et al. [55] also report a typical decrease of resistivity with increasing pressure. They also report a weak local moment below T_c with electron spin resonance (ESR).

Wang et al. [56] report on single crystalline LiFeAs which shows a weak ferromagnetic signal in susceptibility measurements, but no magnetic transition can be seen in resistivity. They report that by decreasing the amount of Fe in their samples, the magnetic transition gets suppressed and the superconducting volume fraction is increasing.

Heyer et al. [39] measured the in-plane resistivity of a LiFeAs single crystal. They found

---

[5] together with Pitcher et al. [7] which are not presenting resistivity data

that the temperature dependency of the resistivity can be fitted by a quadratic temperature behavior for temperatures below 40 K (see fig. 4.4). This is a clear indication of strong electron-electron scattering. They also found that the resistivity follows a sublinear behavior for high temperatures and argue that this might stem from a saturation of the resistivity above room temperature, when the free mean path of the electrons becomes comparable to the lattice constant. By assumptions on the conductivity tensor, they found that the saturation resistivity ρ_{lim} lies in the order of $\rho_{\text{lim}} \simeq 300\,\mu\Omega\,\text{cm}$. The quadratic temperature behavior was also found by Kasahara et al. [64] and Rullier-Albenque et al. [63]. Bombor [65, 66] found that it is possible to describe the limiting resistivity by the phenomenological 'parallel-resistor'-model of Wiesmann et al. [25] (see section 3.5). He calculated ρ_{lim} to be $\approx 440\,\mu\Omega\,\text{cm}$.

The improvement of crystal quality is usually checked with the residual resistivity ratio (RRR) which can be seen in table 4.1. In general, LiFeAs samples can be considered as one of the purest of IPS, since they have very high *RRR*-values.

4.7 Ferromagnetic LiFeAs

Since 2009, several publications report on indications of a magnetic order in LiFeAs samples.

As it was stated before, LiFeAs does not show any sign of a SDW, unlike any other IPS [34].

Despite this aspect Zhang et al. [55] found a weak local moment with ESR measurements in polycrystalline LiFeAs. They also report a decrease of resistivity with increasing pressure.

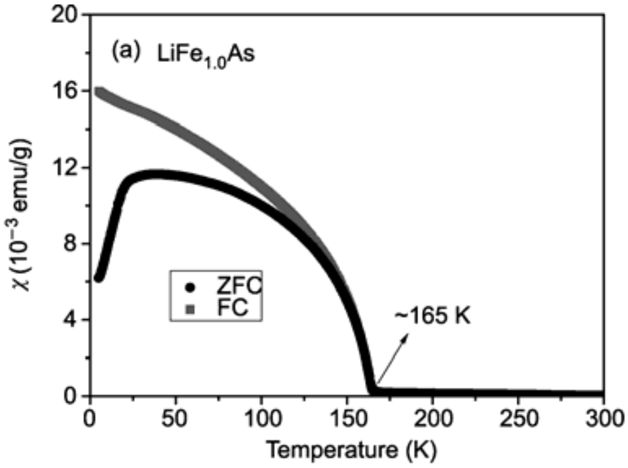

Figure 4.9: Susceptibility of stoichiometric LiFeAs with ferromagnetic transition at 165 K [56].

A couple of months later, Wang et al. [56] found LiFeAs single crystals with a fm transition at 165 K in susceptibility measurements (fig. 4.9). Two possible origins of this fm order are discussed. They argue the possibility of substitutions of Li atoms by Fe due to a solid solution of the iso-structural Fe_2As. The possibility, that the fm order might stem from a Fe_2As-phase, could be excluded because it is afm at 353 K. The second possibility presented is the picture of a canted afm transition, in which the spin orbits are deviating from antiparallel alignment and result in a weak fm moment. Another surprising result of Wang et al. [56] is that their resistivity measurements do not show any anomaly at the fm transition temperature.

Also in 2011, Brydon et al. [12] investigated magnetic and pairing instabilities of LiFeAs by simulating the properties of its Fermi surface [34]. They found that LiFeAs exhibits 'almost fm' incommensurate fluctuations close to the Γ-point. Therefore, they argue that LiFeAs is close to an fm instability, which might be triggered by a reduction of the inner hole pocket at the Γ point. They also found, that these fluctuations favor triplet p-wave superconductivity.

To support their data Brydon et al. [12] relate on the work of Baek et al. [43] which was published later in 2012. As it was already stated in section 4.5, the constant Knight shift K is a support of triplet superconductivity. Another aspect is the strong anisotropy of the line broadening of one of their samples. They argue that this effect might come from anisotropic momentum-dependent spin fluctuations, which would support the 'almost fm' incommensurate fluctuations of Brydon et al. [12].

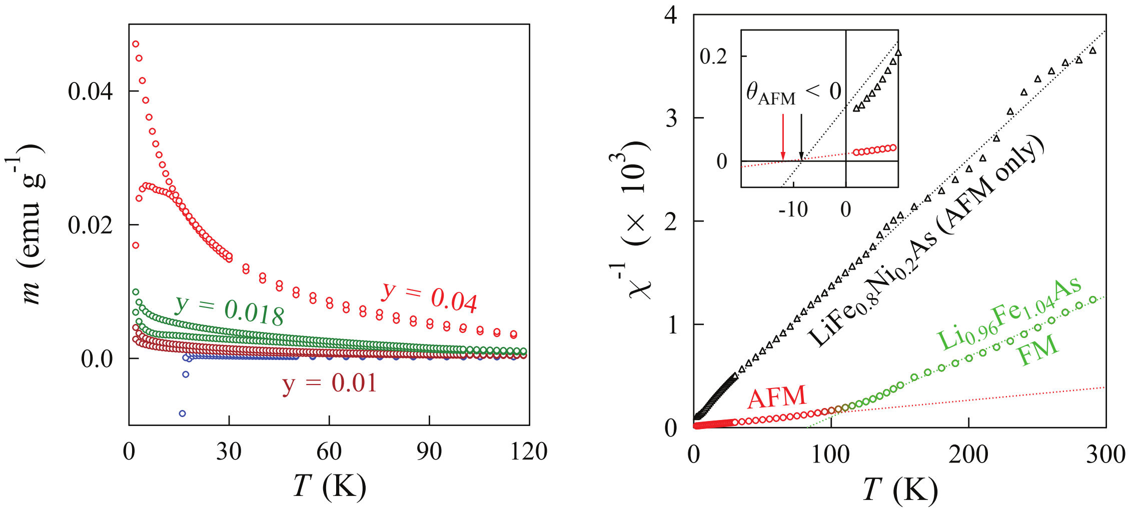

(a) Susceptibility data zero-field cooled (lower curves of same color) and field cooled (upper curves of same color) in 50 Oe for $Li_{1-y}Fe_{1+y}As$ with different Li and Fe concentration y.

(b) Comparison of the inverse susceptibilities of $LiFe_{0.8}Ni_{0.2}As$ and $Li_{0.96}Fe_{1.04}As$. The former demonstrates only afm behavior whereas correlations of the latter seem to cross over from antiferromagnetic to ferromagnetic on warming.

Figure 4.10: Susceptibility measurements on $Li_{1-y}Fe_{1+y}As$ [67]

In 2013, Wright et al. [67] presented susceptibility and muon spin resonance (μSR) studies amongst others on polycrystals of $\mathrm{Li}_{1-y}\mathrm{Fe}_{1+y}\mathrm{As}$. One of their samples ($\mathrm{Li}_{0.96}\mathrm{Fe}_{1.04}\mathrm{As}$) exhibited both fm and afm correlations (see fig. 4.10(b)). They conclude that the moments induced in this Fe-rich samples are not just simply originating from impurity spins of Fe located at the Li places but are of an itinerant character because Fe will mostly act as a donor of electrons and not as impurity scatterer. The extracted moment and transition temperature for the fm behavior are $\mu_{\mathrm{eff}} = 1.75\frac{\mu_B}{\mathrm{f.u.}}$ and $T_C = 78\,\mathrm{K}$. By their µSR measurements of the $\mathrm{Li}_{1-y}\mathrm{Fe}_{1+y}\mathrm{As}$ samples, Wright et al. [67] identified an emergent magnetic phase (see fig. 4.11(a)) with freezing moments on lower temperatures which can be seen by the transformation of the Gaussian relaxation behavior to an exponential one by decreasing temperature and they found these effect to become stronger for higher Fe concentrations. Therefore, Wright et al. [67] proposed a phase diagram containing paramagnetic, superconducting, spin freezing and fm and afm fluctuations regions (see fig. 4.11(b)).

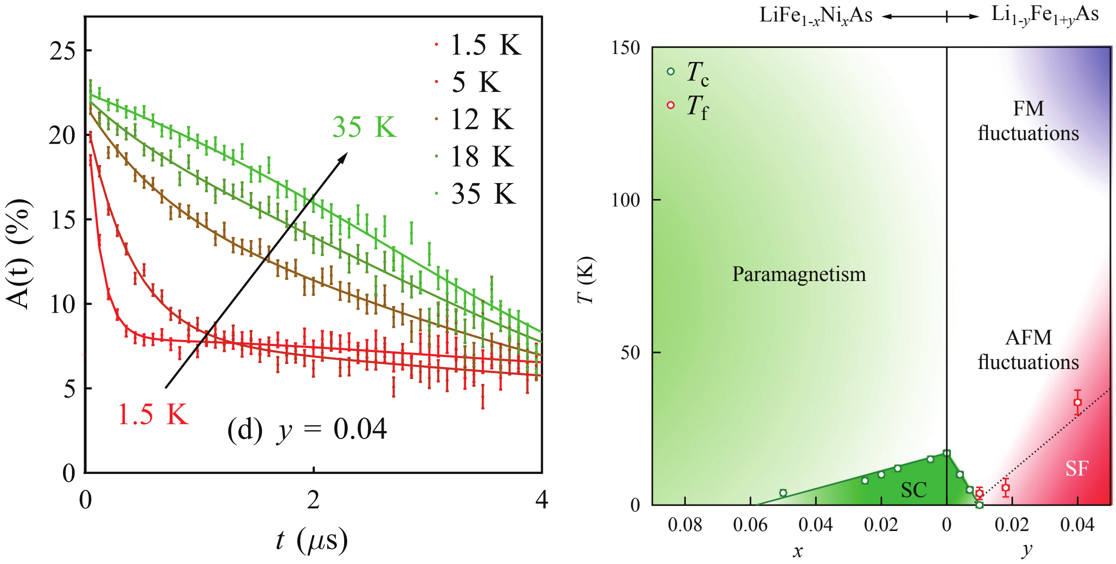

(a) Zero-field muon spin resonance data for $\mathrm{Li}_{0.96}\mathrm{Fe}_{1.04}\mathrm{As}$. A Gaussian function accounts for high-temperature data, but an exponential relaxation emerges on cooling that is more pronounced for samples with higher Fe concentration.

(b) Phase diagram for $\mathrm{Li}_{1-y}\mathrm{Fe}_{1+y}\mathrm{As}$ and $\mathrm{LiFe}_{1-x}\mathrm{Ni}_x\mathrm{As}$, showing regions of superconductivity (SC), spin freezing (SF), as well as antiferromagnetic (AFM) and ferromagnetic (FM) fluctuations.

Figure 4.11: Muon-spin resonance data and phase diagram for $\mathrm{Li}_{1-y}\mathrm{Fe}_{1+y}\mathrm{As}$ [67].

5 Experimental Setup

For this thesis, measurements of nuclear quadrupole resonance (NQR) and electrical resistivity were performed on over 30 different samples of stoichiometric and off-stoichiometric LiFeAs polycrystals. This chapter will briefly describe the course of action taken to perform these measurements.

5.1 Sample Preparation

LiFeAs samples are very air sensitive due to the high reactivity of the Li. To prevent the samples from degradation, all preparations were done under Ar atmosphere in glove boxes. Details on the synthesis procedure can be found in chapter 7. The transport between the synthesis glove box and the experiments was done by using transport bottles closed with paraffin, which were heated to prevent condensation of water inside the bottles.

For the NQR measurements, the polycrystalline samples were grounded to powder and were encapsulated inside a quartz tube which was closed by epoxy. The closed tube was then put into the measurement coil inside the sample probe (see section 5.2). In this way, the samples were stable for several months without degradation and the experiments could be handled without further precautions against air contact as long as the samples were kept at room temperature. By cooling the samples to temperatures of 10 K, it was found that they would degrade after taking them out of the cryostat, i.e. they lost there NQR-signal. It might be possible that the epoxy is getting porous at very low temperatures which could have caused the problem. As long as the sample was kept at low temperatures this was no problem, as it was surrounded by liquid Helium.

For the resistivity measurements, the preparations were performed in a special glove box with a pressure chamber with a length of 2 m which was able to enclose the whole sample rod. After preparing the sample, the rod (see section 5.3) was evacuated to a pressure of 1×10^{-6} bar and was later put into a Dewar flask filled with liquid helium. Due to the condensation of remaining air at the rod walls at these low temperatures, a cryo vacuum was developing which was keeping the sample under high vacuum conditions.

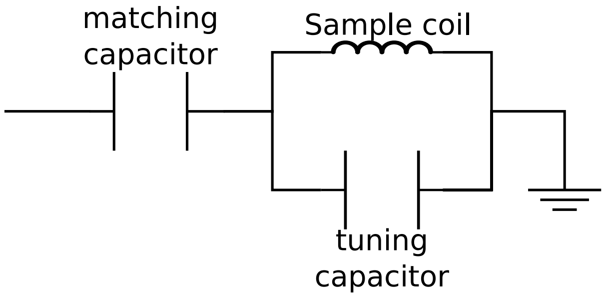

Figure 5.1: Schematic NQR setup.

5.2 Nuclear Quadrupole Resonance

To perform the NQR experiments, a typical nuclear magnetic resonance (NMR) setup with two glass capacitors was used, as described by Hammerath [68], with the major difference that no magnet was needed for NQR. Figure 5.1 shows the schematic setup. It consisted of a matching capacitor and a parallel connection of a tuning capacitor and the sample coil.

The sample coil was constructed to fit the dimensions of the quartz tubes, containing the samples. Wire-thickness and number of turns of the coil were set to get the correct resonance frequency. The possible resonance frequency depends strongly on the inductance L of the sample coil, the higher the number of turns N the lower the resonance frequency ν of the circuit:

$$L \propto N^2, \tag{5.1a}$$

$$\nu \propto \frac{1}{\sqrt{LC}} = \frac{1}{N\sqrt{C}}. \tag{5.1b}$$

The capacitors were cylindrical in shape. The position of the inner cylinder was adjustable, changing the effective length of the capacitor. Thus, it was possible to vary the capacity depending linearly on the effective length.

The variability of the matching and tuning capacitors made it possible to adjust the resonance frequency of the circuit (see eq. (5.1b)). The frequency was changed by the tuning capacitor. The matching capacitor was used to match the amount of applied energy to the coil.

The circuit was put into a sample probe. Additionally to the circuit, the probe contained a heater and a temperature sensor, to control the temperature of the sample. The probe was connected to the outside via shafts for changing the capacities, coaxial cables for the measurement signal and wires for heater and temperature sensor.

The sample probe was able to be put into a cryostat to cool it to the temperature of liquid Helium.

Additionally, a system was used to perform automatic measurements of NQR spectra.

Therefore, it was used either the automatic adjustment system (AAS) developed by Yannic Utz or the NMR Tune system produced by NMR Service GmbH [69]. Both systems were able to automatically tune the resonance circuit to the specified frequency and perform series of multiple measurements.

5.2.1 Temperature Control

Since the NQR frequency is temperature dependent, all spectra were taken at a fixed temperature. Usually, the spectra were taken at 300 K. To get a stable temperature, the NQR probe was put into a cryostat as described in ref. [68]. For 300 K measurements, the sample was only heated without cooling with liquid helium. The heating was performed to get a fixed temperature and thereby minimize instabilities caused by temperature fluctuations at room temperature. The stabilization was done with a proportional-integral control circuit included in the temperature controller. For low temperatures, the sample probe was cooled with liquid helium and the temperature was then stabilized with the heater, see ref. [68].

5.2.2 Measurement Process

To perform an NQR measurement, it is necessary to know the resonance frequency of the sample. From previous measurements, it was known that the NQR frequency of stoichiometric LiFeAs is 21.57 MHz [52]. An area around this frequency was investigated with pulse sequences (see section 2.4) of different frequencies. If there was no resonance signal, the power of the pulse and the pulse length were adjusted.

After finding a signal, the measurement was optimized. Since the signal gets maximized for a 90°-pulse, a pulse-length measurement was performed by the measurement of the signal intensity in dependency of the pulse length.

As the signal intensity is decreasing with increasing distance τ between the pulses and the pulse itself could disturb the measurement, it was necessary to adjust τ to be long enough to prevent disturbances by the 180° pulse and to be short enough to see the signal.

After the optimization process a frequency scan of the NQR-signal was performed. Therefore, the NQR-signal was measured at different frequencies close to the resonance frequency. A frequency scan was necessary, because the ^{75}As-NQR spectra of LiFeAs-polycrystals have a line width which is broader than the band width of the circuit. The resulting signal of each measurement was then Fourier transformed and all measurements were summed up to get the complete spectrum [70].

The signal intensity of the samples was to small to measure it with only one measurement, called scan. Hence, it was necessary to repeat the process and sum the results. This procedure eliminated noise due to its statistical behavior.

5.2.3 Quantitative Analysis

To get quantitative information on the NQR frequency ν_{NQR}, the center of spectral weight (CSW) was extracted by

$$\nu_{\mathrm{NQR}} = \frac{\sum_{i=1}^{N} \nu_i I_i}{\sum_{I=1}^{N} I_i}. \tag{5.2}$$

Here, N is the number of points in the spectrum, ν_i is the frequency of point i and I_i is the intensity at point i. Additionally, the full width at half maximum (FWHM) was extracted as a measure of the line width.

The main target was to get high accuracy on determining the CSW. Therefore, it was necessary to get high intensities of the signals, as can be seen from eq. (5.2). The experimental uncertainty on determining the CSW was mostly defined by the signal to noise ratio (SNR), i.e. a high SNR was resulting in small error bars on the CSW. As the SNR at one frequency ν_i is proportional to

$$\mathrm{SNR} \propto \sqrt{n}\frac{I_{\mathrm{max}}}{I_{\mathrm{noise}}} \tag{5.3}$$

with n being the number of scans, the error of the CSW was reduced if more scans per measurement were taken, i.e. by increasing the measurement time. To get small error bars for broad spectra the measurement time was increased further, since measurements on several frequencies were necessary.

The optimal situation for a set of spectra would have occured if all measurements would have shown the same amount of uncertainty for the CSW, but depending on the width of each spectrum, the measurement time varied strongly. To get a feeling how the measurement time scaled with the width of a spectrum, it was useful to make assumptions on measurements of two spectra with different line widths. The spectra for the two experiments were labeled I and II. Assuming that the line width $\Delta\nu_{\mathrm{II}}$ of spectrum II was twice as wide as the line width $\Delta\nu_{\mathrm{I}}$ of measurement I,

$$\Delta\nu_{\mathrm{II}} = 2\Delta\nu_{\mathrm{I}}, \tag{5.4}$$

and by further assuming that both spectra were symmetric and showed the same integrated intensity, the maximum intensity $I_{\mathrm{max,II}}$ of spectrum II would have been half of the maximum intensity $I_{\mathrm{max,I}}$ of spectrum I:

$$I_{\mathrm{max,II}} = \frac{1}{2} I_{\mathrm{max,I}} \tag{5.5}$$

To get the same SNR for both experiments the following relations have been taken into account:

$$\mathrm{SNR}_{\mathrm{I}} = \sqrt{n_{\mathrm{I}}}\frac{I_{\max,\mathrm{I}}}{I_{\mathrm{noise}}} = \sqrt{n_{\mathrm{II}}}\frac{I_{\max,\mathrm{II}}}{I_{\mathrm{noise}}} = \mathrm{SNR}_{\mathrm{II}} \tag{5.6}$$

$$\sqrt{n_{\mathrm{I}}}\frac{I_{\max,\mathrm{I}}}{I_{\mathrm{noise}}} = \frac{1}{2}\sqrt{n_{\mathrm{II}}}\frac{I_{\max,\mathrm{I}}}{I_{\mathrm{noise}}} \tag{5.7}$$

$$2\sqrt{n_{\mathrm{I}}} = \sqrt{n_{\mathrm{II}}} \tag{5.8}$$

$$4n_{\mathrm{I}} = n_{\mathrm{II}}. \tag{5.9}$$

Thus, to get the same SNR for the maximum position of both spectra, the number of scans for experiment II had to be four times larger than for experiment I. If m_{I} measurements were needed for spectrum I at different frequencies to capture the whole spectrum, typically $m_{\mathrm{II}} = 2m_{\mathrm{I}}$ measurements were needed for spectrum II. If each scan took the time t_{scan}, experiment II would have taken a time of

$$t_{\mathrm{II}} = m_{\mathrm{II}} \cdot n_{\mathrm{II}} \cdot t_{\mathrm{scan}} \tag{5.10}$$

$$= 2m_{\mathrm{I}} \cdot 4n_{\mathrm{I}} \cdot t_{\mathrm{scan}} \tag{5.11}$$

$$= 8 \cdot t_{\mathrm{I}}. \tag{5.12}$$

Therefore, experiment II would have taken eight times longer than experiment I, if the line width between both experiments was doubled and the error of the CSW was kept constant for both experiments. A typical time for an experiment was 9 hours for a small line width. Thus, for the double of the line width the experiment would have taken 72 hours. It would have been the best situation, if the measurement time was maximized to minimize the uncertainties. Such long measurement times were not taken into account for all experiments, therefore, the CSW for experiments with broader line widths usually showed bigger error bars.

5.3 Resistivity

To perform the resistivity measurements, the 4-wire-sensing method was used. To specify the sample geometry, the samples were cut in a cuboid form. A constant current was applied to the sample through two contacts, which were attached to the sample with a conducting glue. These contacts were placed adjacent to each other on both outer sides of the sample (wires A and B in fig. 5.2). The glue covered the full area which was connected to the wires. Thus, the current was able to flow through the whole sample volume. On top of the sample, two other contacts were placed in between the contacts for the current (wires C and D in fig. 5.2). These wires were connected to a voltmeter with a very high impedance. With the 4-wire-sensing method, the current did not flow through the voltage contacts (C,D) and only the voltage between these two contacts was measured.

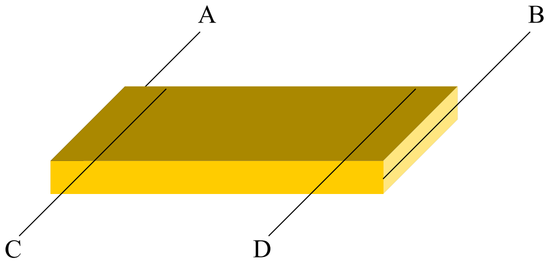

Figure 5.2: Schematic of the 4-wire-sensing method used for the resistivity experiments. The current is applied between contacts A and B and the voltage is measured between contacts C and D.

During the measurement a defined value for the constant current I was generated by a current source. Over a time of 2 s the voltage $U_{\rightarrow}$ over the contacts C and D was measured and averaged. After the measurement of $U_{\rightarrow}$, the current was inversed and the voltage $U_{\leftarrow}$ was measured and averaged for 2 s. Over the whole time of 4 s, the temperature was measured and averaged. The voltage U was then the mean value of $U_{\rightarrow}$ and $U_{\leftarrow}$. The measurement of the voltage for two current directions gave the opportunity to find disturbing voltages, e.g. due to thermoelectric effects. With the measured temperature T, the voltage $U(T)$, and the current I, it was possible to calculate the resistance $R(T) = \frac{U(T)}{I}$. By using the sample geometry, it was then possible to calculate the resistivity of the sample by

$$\rho(T) = R(T) \cdot \frac{wh}{l}, \tag{5.13}$$

with w and h being the sample's width and height, defining the area through which the current was flowing. The distance l is the mean distance between the contacts C and D.

For the resistivity measurements, special sample rods were used, which consist of an inner probe and an outer shell. The inside was able to be evacuated, enabling the measurement under vacuum conditions, which was important for the air sensitive LiFeAs samples. It was possible to connect the inner probe to the outside by the measurement instruments, which were handled by the computer. Due to a thermal coupling with the shell, it was possible to cool the inner probe by a liquid helium bath by putting the rod inside a Dewar flask. The temperature was regulated by a heater which was positioned close to the sample position and a temperature sensor. To minimize temperature errors, the temperature sensor was thermally coupled to the sample by being attached to the sample platform of the rod.

The largest uncertainties by using the 4-wire-sensing method were the dimensions of the sample and the distance between the two voltage contacts, which exceeded the uncertainties of the measurement equipment by several orders of magnitude. Therefore, it was necessary to produce very small contact areas for the voltage contacts, because it is not clear if the voltage was measured between the two contacts or the borders of the contact area of the conducting glue. Achieving small contact areas, was no trivial task by preparations in a glove box. The length of a sample was in a range from 3 mm to 6.6 mm. The width of a typical contact was ≈ 1 mm. Therefore, uncertainties between 15 % and 30 % were typical. Since the uncertainty stemming from the sample geometry was systematic, the temperature dependency of the resistivity stayed unaffected by this. The measurement of the temperature was also affected by uncertainties. Each resistivity-point was measured during a change of temperature and takes ≈ 4 s. Thus, for a chosen rate for temperature-change of $1\,\frac{\mathrm{K}}{\mathrm{min}}$, an uncertainty of 0.07 K per resistivity-point was achieved. Additionally, the measurement of the temperature had a uncertainty of 0.008 K at 4 K and 0.1 K at 300 K.

6 Ferromagnetic LiFeAs

In the year 2010, scientists[1] of the Leibniz Institute for Solid State and Materials Research Dresden (IFW Dresden), the Technical University Dresden and the University Cologne started to investigate ferromagnetic LiFeAs. They performed measurements of static magnetic susceptibility (SMS), ferromagnetic resonance (FMR), nuclear quadrupole resonance (NQR), nuclear magnetic resonance (NMR), muon spin resonance (μSR), dynamic magnetic susceptibility (DMS), magnetoresistance, neutron scattering, Hall effect, and resistivity on $\mathrm{Li}_{1-y}\mathrm{Fe}_{1-x}\mathrm{Ni}_x\mathrm{As}$ single crytsals. Their results prove that $\mathrm{Li}_{1-y}\mathrm{Fe}_{1-x}\mathrm{Ni}_x\mathrm{As}$ undergoes a bulk ferromagnetic (fm) transition which is not originated from an impurity phase. With the use of NQR it is possible to construct an electronic phase diagram of $\mathrm{Li}_{1-y}\mathrm{Fe}_{1-x}\mathrm{Ni}_x\mathrm{As}$ which indicates that LiFeAs is close to an fm instability consistent with the results of Brydon et al. [12]. These results will be published in reference [66].

This chapter will use the results from the experiments mentioned above and combine them to get a comprehensive view of the nature of ferromagnetism in LiFeAs.

6.1 Sample Preparation

The experiments mentioned above were performed on single crystals consisting of Ni doped Li deficient LiFeAs. These samples were synthesized and characterized by Luminita Harnagea. They were grown by the self flux technique [11, 52] and their compositions were checked with the help of energy dispersive x-ray (EDX) and inductively coupled plasma optical emission spectroscopy (ICP). The phase purity was confirmed with single crystal diffractometry and powder X-ray diffraction (XRD). The resulting crystals can be divided into two groups. One single crystal is not doped with Ni and shows a Li-deficiency of $y = 0.1$ and it is therefore referred to as $\mathrm{Li}_{0.9}\mathrm{FeAs}$. The other group are Ni-doped single crystals with a Li-deficiency of $y = 0.33$ and different Ni contents x. These samples are referred to as $\mathrm{Li}_{0.67}\mathrm{Fe}_{1-x}\mathrm{Ni}_{1+x}\mathrm{As}$ with $x = 0.02, 0.025$ and 0.06.

---

[1] Alexey Alfonsov, Bernd Büchner, Hans-Joachim Grafe, Uwe Gräfe, Luminita Harnagea, Christian Hess, Hans-Henning Klauß, Philipp Materne, Seung-Ho Baek, Dirk Bombor, Markus Braden, Franziska Hammerath, Christian Rudisch, Anja U. B. Wolter-Giraud and Sabine Wurmehl

6.2 Evidence of Ferromagnetism in Li deficient LiFeAs Derivatives

The following sections will show the results of the experiments which give proof for the existence of a fm phase transition in Li deficient LiFeAs derivatives. The methods used are SMS, FMR, NQR, µSR, DMS, magnetoresistance, and neutron scattering.

6.2.1 Static Susceptibility

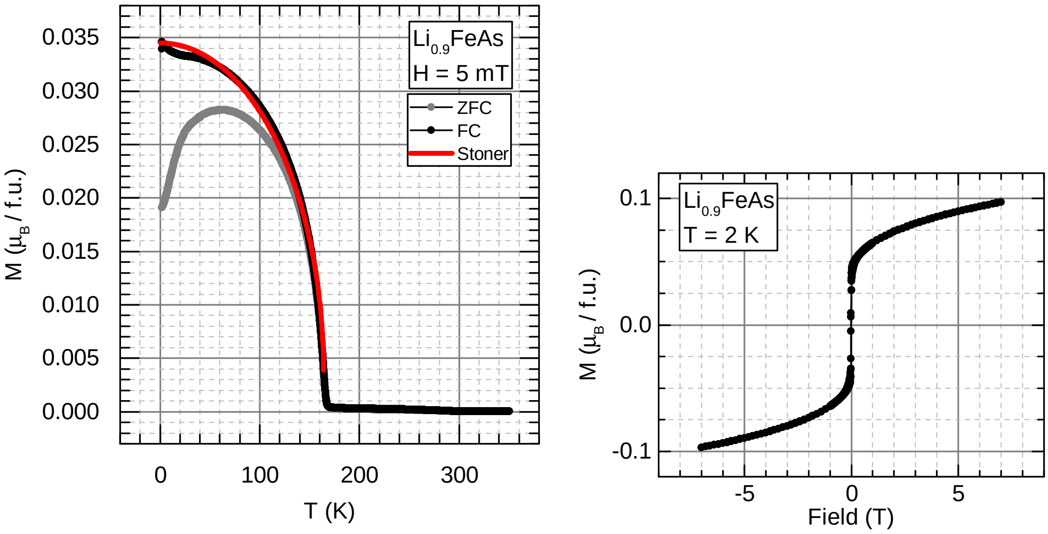

(a) Zero-field cooled magnetization M vs. temperature T at 5 mT and 1 T

(b) Magnetization M vs. magnetic field at 2 K

Figure 6.1: Susceptibility measurements on Li$_{0.9}$FeAs. Measurements done by L. Harnagea [66].

Usually the starting point to study magnetic transitions is the measurement of the SMS. The measurements and analysis of the results presented in this section were performed by Luminita Harnegea.

Figure 6.1(a) shows the temperature dependency of the susceptibility of Li$_{0.9}$FeAs in a field of 5 mT applied along the ab-plane of the sample. The course of the curve shown for 5 mT is typical for the temperature dependent susceptibility of a weak ferromagnet as proposed by the Stoner model [71] (see section 6.5 for more details). So, eq. (6.8) can be easily fitted to the data points. It is possible to extract the Curie temperature T_C from the inflection point, resulting in $T_C \sim 164$ K. The Li$_{0.67}$Fe$_{1-x}$Ni$_{1+x}$As samples exhibit a similar behavior. For $x = 6\,\%$, T_C is reduced to 134 K which might be related to the Ni doping.

The 5 mT curve of fig. 6.1(a) resembles very much the susceptibility data of Wang et al. [56] (shown in fig. 4.9). Even the transition temperatures lie very close to each other (T_C(Wang) = 165 K). The qualitative similarities show that they are most likely dealing with the same physical effect.

Figure 6.1(b) shows the results of field-dependent measurements of the susceptibility at a temperature of 2 K. It can be seen that the magnetization does not saturate for fields below 7 T and the magnetic moment which can be reached at saturation will be above $0.1\,\frac{\mu_\mathrm{B}}{\mathrm{f.u.}}$. This magnetic moment is more than one order below the moment extracted from Wright et al. [67] ($\mu_\mathrm{Wright} = 1.75\frac{\mu_B}{\mathrm{f.u.}}$) and their transition temperature is much smaller (T_C(Wright) = 78 K). It is not clear so far if these differences can be explained by smaller amount of Li deficiency.

The susceptibility curves for temperatures above T_C (not shown here) show a linear field dependency, which proves a paramagnetic (pm) behavior and the absence of magnetic impurities.

6.2.2 Ferromagnetic Resonance

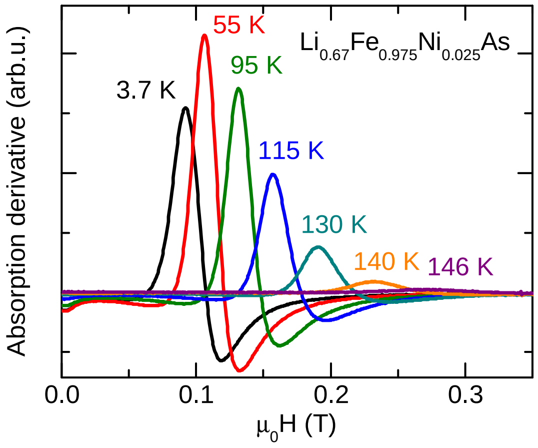

Figure 6.2: Development of the ferromagnetic resonance signal in $Li_{0.67}Fe_{0.975}Ni_{0.025}As$. Measurements done by A. Alfonsov [66].

After SMS showed that the samples are weak ferromagnets, it is worth to try if they also show a FMR signal, which is, as the name suggests, usually only possible if the material is fm. Therefore, such measurements were performed and analyzed by Alexey Alfonsov to get information about the nature of the present magnetism.

FMR is a spectroscopic technique to probe the magnetization of ferromagnetic materials. It is done by the resonant absorption of electromagnetic radiation of a ferromagnet.

Figure 6.2 shows the development of an FMR line in $Li_{0.67}Fe_{0.975}Ni_{0.025}As$ at a frequency of $\nu = 9.6$ GHz. Such an FMR signal can also be seen in $Li_{0.9}FeAs$. The FMR signal emerges below a certain temperature T_FMR which is 155 K for $Li_{0.67}Fe_{0.975}Ni_{0.025}As$ and 175 K for $Li_{0.9}FeAs$. Since FMR is more sensitive to dynamic correlation effects than macroscopic methods like SMS, it is not untypical that T_{FMR} is about 10 K higher than T_C. These dynamic correlations develop already at temperatures slightly above the ordering temperature.

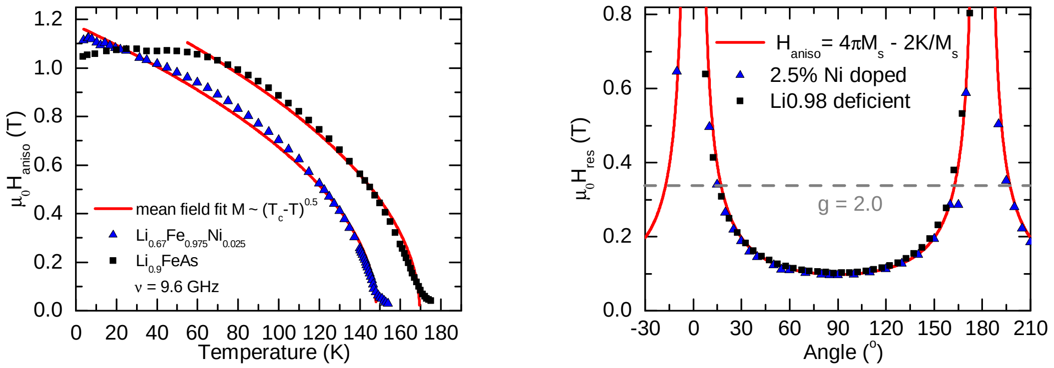

(a) Temperature dependencies of the anisotropy fields for $\mathrm{Li_{0.67}Fe_{0.975}Ni_{0.025}As}$ and $\mathrm{Li_{0.9}FeAs}$ samples.

(b) Angular dependencies of the resonance fields measured at $T = 4\,\mathrm{K}$ in $\mathrm{Li_{0.67}Fe_{0.975}Ni_{0.025}As}$ and $\mathrm{Li_{0.9}FeAs}$ samples. For 0° the external field is parallel to the c-direction.

Figure 6.3: Ferromagnetic resonance measurements on $\mathrm{Li_{0.9}FeAs}$ and $\mathrm{Li_{0.67}Fe_{0.975}Ni_{0.025}As}$. Measurements done by A. Alfonsov [66].

It is possible to extract the effective anisotropy field $H_{\mathrm{aniso}} = 4\pi M_s - 2\frac{K}{M_s}$ with K as uniaxial anisotropy constant [72]. The effective anisotropy field $H_{\mathrm{aniso}}(T)$ is equal to the effective magnetization M_{eff}. The resulting temperature dependencies of H_{aniso} for both samples can be seen in fig. 6.3(a). It is possible to fit a mean field theory $M \propto (T_C - T)^A$ to the data. This theory expresses the spontaneous magnetization below T_{FMR}. The obtained critical exponents of $A \sim 0.5$ suggests conventional 3D ferromagnetism.

Additionally the angular dependency of the resonance fields of $\mathrm{Li_{0.67}Fe_{0.975}Ni_{0.025}As}$ and $\mathrm{Li_{0.9}FeAs}$ samples at 4 K were measured which are almost identical for both samples and the same expression [72, 73] can be fitted to the data(see fig. 6.3(b)). Since the shape anisotropy plays a minor role due to the small investigated magnetic moments, the intrinsic uniaxial anisotropy contributes the most to the angular dependency of the resonance field. Therefore, it can be concluded that the nature of the magnetism in both samples is of anisotropic nature, likely due to the layered structure of the crystals.

6.2.3 Muon Spin Resonance

Next to FMR, a well suited method to investigate on magnetic materials is µSR. Similar to NMR, it is taking advantage of the precession of the magnetic moment, but in this case of

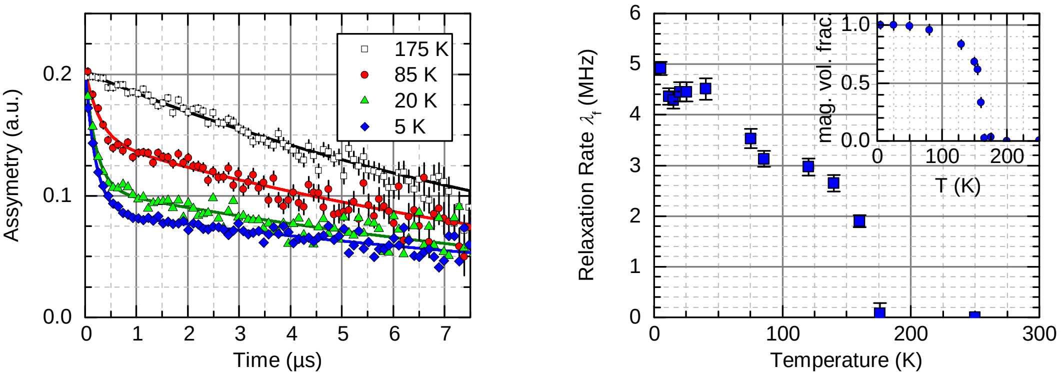

(a) Time evolution of the asymmetry of muon spin resonance spectra at different temperatures.

(b) Relaxation rate λ_f vs. temperature.

Figure 6.4: Muon spin resonance measurements on $Li_{0.9}FeAs$. Measurements done by P. Materne [66]

an implanted muon. The data presented here was measured by Philipp Materne from the TU Dresden.

Figure 6.4(a) shows the time evolution asymmetry of the µSR spectra of $Li_{0.9}FeAs$ at different temperatures. The shown spectra can be described with a combination of gaussian and exponential relaxations and high temperatures. The former is caused by the interaction of the muon spin with dense nuclear magnetic moments and the latter is a result of dynamical behavior.

Below $T = 175\,K$, a fast exponential relaxation sets in which can be explained by a short-range magnetic order.

The relaxation rate of the µSR spectra is a good estimation for the magnetization of a sample, if coherent oscillations of the muon spin are absent. The relaxation rate, which measures the width of the magnetic field distribution at the muon site, was determined, but a dynamic contribution can not be excluded. The temperature dependency of the calculated magnetization can be found in fig. 6.4(b). The resemblance of fig. 6.4(b) with the SMS data shown in fig. 6.1(a) is obvious.

The exponential relaxation of the µSR spectra is the same for the pm and the fm phase which is an indication for a temperature-independent dynamical behavior.

The inset of fig. 6.4(b) shows the corresponding volume fraction which shows a 100 % magnetically ordered sample below ≈ 75 K. The onset of magnetic order at $T = 175\,K$ corresponds very well to the ferromagnetic transition temperature T_{FMR} determined by FMR (see section 6.2.2).

By comparing these measurements with Wright et al. [67], similarities become visible (see fig. 4.11(a)). Also Wright et al. [67] have seen the development of a magnetic order with transformation from a gaussian relaxation to an exponential one. But for them this transition happens below much lower temperatures than 35 K. It might be, that the spin freezing phase proposed by Wright et al. [67] is actually the same as the fm transition at a suppressed T_C.

6.2.4 Dynamic Magnetic Susceptibility

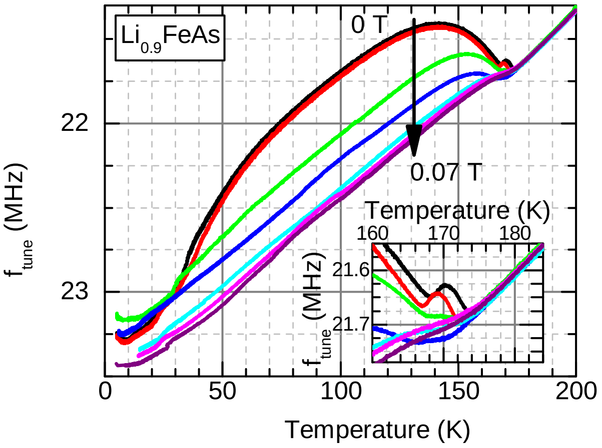

Figure 6.5: Dynamic magnetic susceptibility of $Li_{0.9}$FeAs. Measurements done by C. Rudisch [66, 74].

The DMS is another typical method to determine magnetic phase transitions. It yields not only information about the transition temperature, but also, by examining the shape of the susceptibility curve, it can give information if a magnetic sample shows itinerant or localized magnetism.

In NMR groups, the DMS is measured using an effect, that the change of the resonance frequency of a resonant circuit is directly proportional to the DMS and electric conductivity of the sample inside the coil of the resonant circuit [75]. The data shown here were measured by Christian Rudisch.

Figure 6.5 shows the shift of frequency versus the temperature measured for $Li_{0.9}$FeAs at different magnetic fields ranging from 0 T to 0.07 mT. Two notable features are visible. The first feature is a very broad hump visible for temperatures below 168 K and fields between 0 T and 0.03 T. A broad structure, as this hump, is typical for a weak itinerant ferromagnet [75].

But the curves also show a narrow peak with its maximum at 170 K as a second feature (see inset of fig. 6.5), which is only visible up to a field of 5 mT. The peak begins to rise below a temperature of 174 K. Such a sharp peak is a sign for localized ferromagnetic moments [75].

So, the DMS measurement of $Li_{0.9}$FeAs shows signs of two different magnetic phase transitions. At first, there is a localized fm transition at 174 K, which coincides with the transition temperature measured by FMR ($T_{\mathrm{FMR}} = 175$ K). Then, at 168 K, there is an itinerant fm transition. If this sample really shows two types of fm transitions, it opens the door for interesting physical questions, e.g. if it is possible, that the localized fm moments somehow interact with the conduction electrons which results in the latter itinerant transition. Unfortunately, the two transition temperatures can only be seen with DMS and are not supported by other measurements.

Both the peak and the hump vanish for higher magnetic fields. The reduction of the susceptibility originates from the polarization of the itinerant magnetic moments. Polarized moments do not contribute to the dynamic susceptibility and therefore, the signal vanishes.

6.2.5 Magnetoresistance

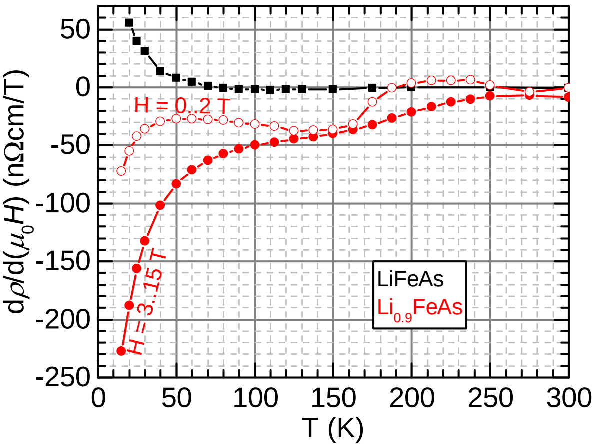

Figure 6.6: Magnetoresistance of $Li_{0.9}FeAs$ compared to stoichiometric LiFeAs. Measurements done by D. Bombor [65, 66].

A fm transition should make it possible to see effects on the conduction electrons by magnetoresistance measurements. Such measurements were performed by Dirk Bombor on $Li_{0.9}FeAs$. The results are shown in fig. 6.6 in comparison to stoichiometric LiFeAs and are divided in measurements of the average for small (0...2 T) and for high (3...15 T) magnetic fields.

For small fields and temperatures above 180 K, the magnetoresitance is close to zero and below it is negative. This can be interpreted as a magnetic transition. For high fields, the magnetoresistance is always below zero. The reason is the same as the reduction of the hump for the DMS in the previous section. The negative magnetoresistance is caused by the magnon-scattering with electrons induced by the ferromagnetism of $Li_{0.9}FeAs$. With increasing magnetic field, the population of magnons is decreasing due to the polarisation of the moments and therefore, the magnon-scattering decreases, too. Thus the magnetoresistance is decreasing.

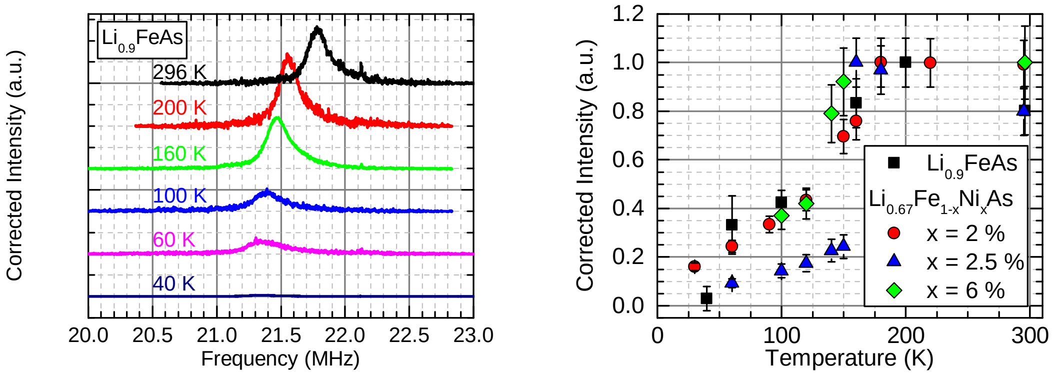

(a) ^{75}As nuclear quadrupole resonance spectra for Li$_{0.9}$FeAs at different temperatures.

(b) Intensities of ^{75}As nuclear quadrupole resonance spectra vs. temperature of Li defcient and Ni doped LiFeAs.

Figure 6.7: Nuclear quadrupole resonance spectra and intensities for Li$_{0.9}$FeAs and Li$_{0.67}$Fe$_{1-x}$Ni$_x$As. Measurements done by S.-H. Baek, H.-J. Grafe, and F. Hammerath [66].

6.2.6 Nuclear Quadrupole Resonance

The previous sections show that the samples undergo a transition to an anisotropic weak 3D-ferromagnet of itinerant nature. But it is not clear so far if the magnetic transition is bulk or if it only originates from a foreign phase inside the sample. At this point NQR, comes into play. As described in section 2.6, an NQR-signal should show an abrupt loss of intensity, if the sample undergoes a magnetic transition. Therefore, S.-H. Baek, H.-J. Grafe and F. Hammerath performed temperature dependent ^{75}As-NQR measurements on Li$_{0.9}$FeAs and Li$_{0.67}$Fe$_{1-x}$Ni$_x$As.

In fig. 6.7(a), the spectra of Li$_{0.9}$FeAs at different temperatures are shown. The NQR signal of ^{75}As is shifting to lower frequencies at decreasing temperature which is a typical behavior for iron pnictide superconductors (IPS) and is usually attributed to electronic multi-orbital effects of Fe 3d^6 electrons [43, 76, 77]. The linewidth of Li$_{0.9}$FeAs ($\sim$ 200 kHz) at room temperature is increased, compared to stoichiometric LiFeAs ($\sim$ 60 kHz). This broadening of the linewidth originates in structural disorder of the electric environment of the nucleus, introduced by Li vacancies. Below 160 K, the intensity drops and further decreases to lower temperatures. The drop of intensity is caused either, by an internal magnetic field at the ^{75}As-nucleus that shifts the resonance to another frequency in case of a commensurate magnetic order or, the drop is caused by a strong broadening of the spectra by an incommensurate magnetic order. It is not possible to exclude an incommensurate magnetic order so far, because a resonance shifted by an internal magnetic field was not found. The intensity drop of Li$_{0.9}$FeAs and Li$_{0.67}$Fe$_{1-x}$Ni$_x$As can be seen in fig. 6.7(b).

Due to the microscopic nature of the NQR, which only probes ^{75}As-nuclei which are inside the FeAs structure of LiFeAs, an origin of the ferromagnetism in impurity phases can be excluded. The drop of the signal intensity below T_C is therefore indeed a proof for the bulk nature of the phase.

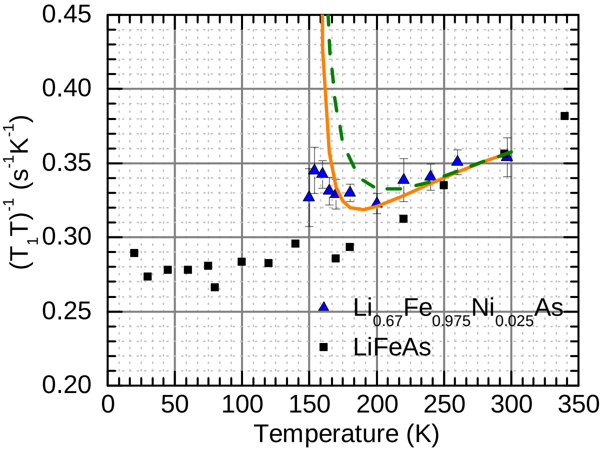

Figure 6.8: $(T_1T)^{-1}$ for $Li_{0.67}Fe_{0.975}Ni_{0.025}As$ and stoichiometric LiFeAs measured by ^{75}As nuclear quadrupole resonance. The solid orange line is a simulation for a ferromagnetic and the dashed green line a simulation for an antiferromagnetic transition at 154 K. Measurements done by S.-H. Baek and H.-J. Grafe [66].

To get further information on the nature of the magnetic transition, the spin lattice relaxation rate divided by temperature $(T_1T)^{-1}$ was analyzed, which is shown in fig. 6.8. The quantity $(T_1T)^{-1}$ measures the sum over all wave vectors $\vec{q}$ of the imaginary part of the dynamic spin susceptibility in the first Brioullin zone [78]: $(T_1T)^{-1} \propto \sum_{\vec{q}} |A_\perp(\vec{q})|^2 \frac{\chi''_\perp(\vec{q},\omega_0)}{\omega_0}$. Surprisingly, $(T_1T)^{-1}$ is only moderately enhanced somewhat above the magnetic transition temperature, T_C, indicating only weak enhancement of magnetic fluctuations towards T_C. A similar behavior can be seen in antiferromagnetic (afm) parent compounds of other IPS, e.g. (Ba,Ca,Sr)Fe_2As_2 [77, 79, 80], where the moderate enhancement of $(T_1T)^{-1}$ above T_{SDW} was interpreted as evidence for a first-order magnetic transition. Allthough, Ning et al. [80] and Curro et al. [81] found that small amounts of Co or Ni doping in $Ba(Fe_{1-x}Co_x)_2As_2$ reduce the magnetic ordering temperature and increase magnetic fluctuations above T_{SDW}, leading to a diverging behavior of $(T_1T)^{-1}$ on approaching the magnetic ordering temperature. Ning et al. [80] and Curro et al. [81] treated this as evidence for a second order transition and an incommensurate spin density wave (SDW) in $Ba(Fe_{1-x}Co_x)_2As_2$. On the other hand, in $Ca(Fe_{1-x}Co_x)_2As_2$ the first-order nature of the transition is conserved even for Co concentrations up to x=0.056, and no divergent behavior of $(T_1T)^{-1}$ could be found.

Therefore, in the case of Ni doped LiFeAs, the magnetic transition is probably first-order-like despite the disorder introduced by Ni doping, which is supported by Cano et al. [82] who theoretically found a conservation of the first order character.

The solid and dashed lines in fig. 6.8 are simulations of fm and afm models, including a linear term to capture the linear temperature dependency of $(T_1T)^{-1}$ at higher temperatures. These fits represent theoretical models for weak fm or afm metals. The ferromagnetic model is given by $(T_1T)^{-1} \propto 1/(T - T_C)$, and the antiferromagnetic by $(T_1T)^{-1} \propto 1/(T - T_N)^{1/2}$ [81, 83]. Such models work well for Ni doped $BaFe_2As_2$ [81], but obviously they do not for $Li_{0.67}Fe_{1-x}Ni_xAs$.

6.2.7 Neutron Scattering

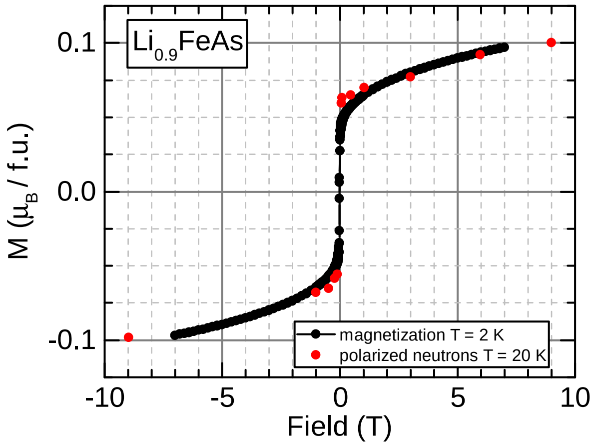

Figure 6.9: Comparison of magnetization measured with neutron scattering and static susceptibility of $Li_{0.9}FeAs$. Measurements done by M. Braden [66].

To further prove the bulk nature of the ferromagnetism in $Li_{0.9}FeAs$ and to exclude secondary phases as origin, the magnetization was measured with polarized-neutron diffraction on several Bragg peaks by Markus Braden of the university of Cologne.

Both, the temperature and the field dependency (see fig. 6.9) mimic the susceptibility data shown in section 6.2.1. Also, the measured magnetic moments originate from positions in the lattice which could be assigned to sites usually taken by Li atoms. Therefore, the occurring fm signal is a property of $Li_{0.9}FeAs$ and not of inclusions or secondary phases.

6.2.8 Summary

By the previous section, a comprehensive picture of the fm transition of Li deficient LiFeAs derivatives was drawn.

The SMS of section 6.2.1 clearly shows an fm transition at 164 K. The susceptibility curve can be fitted by the Stoner model [71], which indicates, that the samples are weak ferromagnets. By FMR it was shown in section 6.2.2 that it is an anisotropic 3D-ferromagnetism, which was done by a mean field fit to the data. µSR of section 6.2.3 could show that the magnetism has to be short ranged due to its fast exponential relaxation µSR spectra below 175 K. By DMS, the magentism was identified as itinerant in section 6.2.4, due to its broad hump in the DMS, but also showed signs of localized magnetism, which is not supported by other methods. The magnetroresistance measurement of section 6.2.5 confirmed the magnetic transition. By NQR, in section 6.2.6 it was shown, that the magnetism is a property of the bulk and is not originated in impurity phases. Furthermore, it showed that the phase transition is of first order. Polarized-neutron diffraction (section 6.2.7) did confirm the bulk nature of the magnetism and identified that the moments originate in Li positions of the structure.

So in summary, $Li_{0.9}FeAs$ undergoes a first order fm tansition at 164 K. The established ferromagnetism is itinerant, shortranged, anisotropic, shows 3D character, and is of bulk nature. Now that the ferromagnetism is characterized, the next section will deal with further distinctive properties of the fm samples to shed light on the origin of the fm transition.

6.3 Distinctive Properties of ferromagnetic LiFeAs Derivatives

Ferromagnetism is not the only property which distinguishes $Li_{1-y}Fe_{1-x}Ni_xAs$ from stoichiometric LiFeAs. All fm samples show different behavior in NQR, Hall effect and electrical resistivity measurements. Especially, the distinction of the fm samples by their NQR frequencies can be used to produce a superconducting and fm phase diagram of $Li_{1-y}Fe_{1-x}Ni_xAs$.

The next sections will present the data of these distinguishing measurements.

6.3.1 Nuclear Quadrupole Resonance

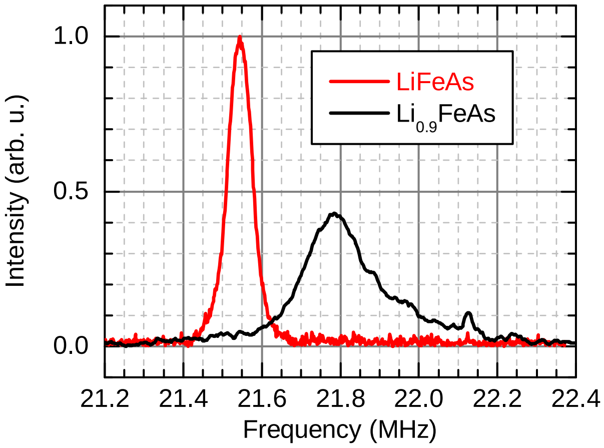

Figure 6.10: Nuclear quadrupole resonance spectra at room temperature of stoichiometric LiFeAs and $Li_{0.9}FeAs$. Measurements done by S.-H. Baek and H.-J. Grafe [66].

In section 6.2.6, it was already mentioned that the room temperature spectrum of $Li_{0.9}FeAs$ is shifted to higher frequencies compared to the stoichiometric compound. This effect, measured by S.-H. Baek and H.-J. Grafe, is visualized in fig. 6.10. From these spectra, it is possible to extract the quadrupole frequency.

As stated in chapter 2, the quadrupole frequency is connected to the local charge distribution in a crystal.

The Li-deficient samples have a different local charge distribution around the ^{75}As-site and the effects on the physical properties, i.e. ferromagnetism, can only be found in samples which show NQR frequencies which are higher than 21.7 MHz.

Also, the Li deficient samples show a strongly modified structure compared to stoichiometric LiFeAs, which can be concluded from the strong increase in line width from $\sim$ 60 kHz for LiFeAs to $\sim$ 200 kHz for $Li_{0.9}FeAs$. A broadening of the NQR signal is caused by a distribution of electric field gradients (EFGs), caused by modified charge distributions. Since there are many different areas, the combined resonant signals sum up to a broad resonance line (see also chapter 2).

6.3.2 Hall Effect and Resistivity

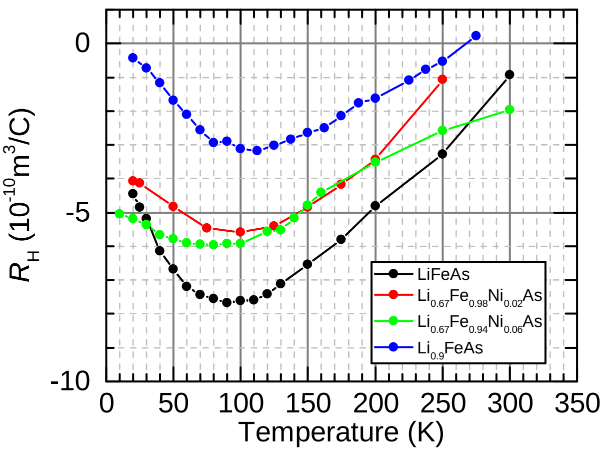

Figure 6.11: Hall constant for $Li_{0.9}FeAs$ and $Li_{0.67}Fe_{1-x}Ni_xAs$. Measurements done by D. Bombor [65, 66].

The distinction of the different samples by Hall effect was measured by Dirk Bombor and can be seen in fig. 6.11.

The Hall coefficient of all samples is negative and shows a clear minimum around 100 K. The increase of the Hall coefficient at higher temperatures can be explained with thermal broadening of the Fermi distribution [39]. The sign of the Hall constant is directly connected to the sign of the charge carriers in the sample. So in samples in which their conductivity is dominated by holes would show a positive Hall constant, and vice versa for electrons. The Li-deficient samples show a clear shift of the Hall coefficient towards positive values, but stays negative. Due to the multiband character, an interpretation is not straight forward. It might be, that electrons are compensated by holes and thus Li deficiency might be hole doping, but there is no guarantee that this is true. For comparison: The Hall coefficient for Co doped LiFeAs [65] is shifted to more negative values and can be classified clearly as electron doping by angle-resolved photoemission spectroscopy (ARPES)-measurements [11].

Figure 6.12 shows the resistivity data for the different samples, also measured by Dirk Bombor.

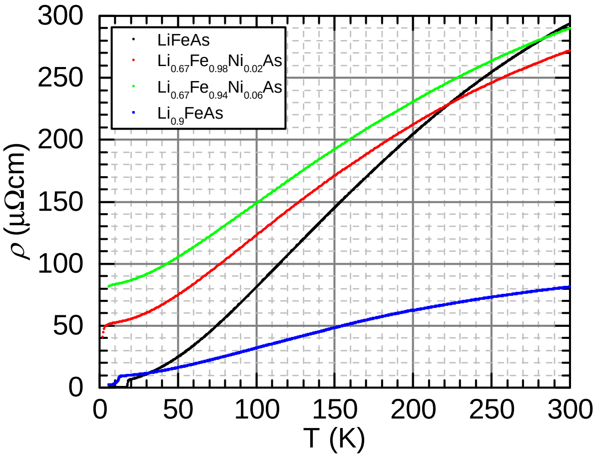

Figure 6.12: Resistivity vs. temperature for $\mathrm{Li_{0.9}FeAs}$ and $\mathrm{Li_{0.67}Fe_{1-x}Ni_xAs}$. Measurements done by D. Bombor [65, 66].

The resistivity ρ exhibits a metallic temperature dependency with a monotonic increase of ρ with temperature. It drops to zero at $T_c = 18\,\mathrm{K}$ for the undoped compound but not for the Ni-doped compounds. The Li-deficient sample also shows a slight drop of the resistivity at low temperatures but it never vanishes, which is consistent with the absence of bulk superconductivity.

In all samples there is no anomaly in the resistivity, which could be attributed to a structural or SDW transition.

At low temperatures a quadratic temperature dependency $\rho = \rho_0 + AT^2$, where ρ_0 is the residual resistivity, was fitted to the resistivity data. The residual resistivity of the undoped compound was found to be as low as $\rho_0 = 2.9\,\mu\Omega\mathrm{cm}$, which results in a residual resistivity ratio of $\rho(300\,\mathrm{K})/\rho_0 = 100$ and is a sign of high quality single crystals.

The resistivity of the Li-deficient sample is strongly decreased compared to the Ni-doped and stoichiometric compounds. Fitting the data with the quadratic model revealed a strong decrease of the quadratic coefficient A. This can be interpreted as a decrease of electron-electron scattering.

A possible explanation for the reduced resistivity at high temperatures of $\mathrm{Li_{0.9}FeAs}$ would be an increase of the density of states (DOS) at the Fermi energy.

In contrast, the resistivity at high temperatures of the Ni-doped compounds is only slightly changed compared to the stoichiometric LiFeAs. Also here, the electron-electron scattering is reduced, as can be seen by the flat slope of the curves, but the reduced scattering in these samples gets hindered by introduced scattering centers through the additional Ni atoms in the compound.

6.4 Charge Doping

Measurements of one Co doped $LiFe_{0.95}Co_{0.05}As$-sample are showing a decreased quadrupole frequency [43] compared to stoichiometric LiFeAs. Co doping on LiFeAs can clearly be asigned to electron doping by ARPES-measurements [11]. Also, measurements of Hall effect show a negative Hall constant for electron doped materials, as it is the case for Co doped LiFeAs [65]. For the Li deficient LiFeAs the Hall constant is shifted to more positive values (see fig. 6.11). Therefore, Li deficiency could be interpreted as hole doping. Since the Li deficient samples show an increased quadrupole frequency compared to stoichiometric LiFeAs and one Co-doped LiFeAs-sample showed an decreased quadrupole frequency, there were hopes that the quadrupole frequency is a measure of the charge carrier concentration.

Unfortunately, this one $LiFe_{0.95}Co_{0.05}As$-sample was the only one which showed the reduced quadrupole frequency. Experiments on samples with other Co concentrations could not confirm this result. Comparison with NQR-studies on other members of the IPS reveal that the quadrupole frequency behaves differently on charge doping depending on which samples are examined. For LaOFeAs (La1111) electron doping is leading to a strong shift of the NQR frequency to higher values [84, 85]. While electron doping, e.g. Co for Fe, on $BaFe_2As_2$ (Ba122) has almost no effect on the quadrupole frequency, but with hole doping, e.g. K for Ba, shows a strong increase of the frequency [76, 86]. Even electron doping in the same family as LiFeAs, Co for Fe in NaFeAs, has no effect on the quadrupole frequency [87].

So the hope that the quadrupole frequency is a measure of the charge carrier concentration did not come true.

6.5 Stoner Model

In section 6.2.1, it was shown that the susceptibility curve of $Li_{0.9}FeAs$ shown in fig. 6.1(a) can be described by the susceptibility of the Stoner model for weak ferromagnets. Before in the next section the origin of the fm order will be discussed, this section will take a look on the Stoner model [71]. The following statements are based on [88] which presents the Stoner model as a mean field treatment of the Hubbard model [89].

The starting point is the Hubbard model, which is, briefly spoken, a model of a solid state body, which describes the behavior of electrons in a rigid lattice. It is the most simple model to study the interplay of kinetic energy, Coulomb repulsion, and Pauli principle. Thereby, the Coulomb forces are only considered for such electrons which are sitting on the same lattice site.

At the beginning the system is placed in a uniform magnetic field H

$$\mathcal{H} = \sum_{k\sigma} E_k \hat{n}_{k\sigma} + U \sum_j \hat{n}_{j\uparrow}\hat{n}_{j\downarrow} - \frac{g\mu_B H}{2} \sum_j (\hat{n}_{j\uparrow} - \hat{n}_{j\downarrow}). \tag{6.1}$$

The first term of eq. (6.1) describes in principle the kinetic energy of the band electrons, the second term is the so called Hubbard term and stands for the Coulomb repulsion of two electrons sharing the lattice site j, therby U is the interaction strength, and the last term stands for the interaction of the system with the magnetic field. The response of the system is the development of a uniform spin polarization m

$$\langle \hat{n}_{j\uparrow} \rangle = \frac{n}{2} + m \qquad \langle \hat{n}_{j\downarrow} \rangle = \frac{n}{2} - m. \tag{6.2}$$

The spin polarization leads to a redistribution from electrons with spin down to electrons with spin up. This redistribution leads to an increase of the kinetic energy which has to be compensated by the potential energy. By doing a mean field decoupling of the Hubbard term, the energy change caused by the spin polarization can be described as

$$\Delta E(m) = \int_{\mu_0}^{\mu_\uparrow} E D(E) dE - \int_{\mu_\downarrow}^{\mu_0} E D(E) dE - U m^2 - g\mu_B H m. \tag{6.3}$$

Hereby, μ_0 is the chemical potential at $H = 0$ and $D(E)$ is the DOS at energy E.

By increasing U from zero, magnetization sets in if $\Delta E(m)$ is becoming negative for some m. For a second order magnetic transition, where m is increasing continuously from 0, m is induced by the external magnetic field. For weak H, $D(E)$ can be replaced by the DOS at the Fermi energy E_F, $D(E) \approx D(E_F)$, in the second order expansion of the energy

$$\Delta E = \frac{m^2}{D(E_F)} - U m^2 - g\mu_B H m. \tag{6.4}$$

Minimizing with respect to m leads to

$$\chi = \frac{m g \mu_B}{H} = \frac{(g\mu_B)^2 D(E_F)}{2} \frac{1}{1 - U D(E_F)} = \frac{\chi_{\text{Pauli}}}{1 - U D(E_F)}. \tag{6.5}$$

So, the susceptibility is enhanced by the electron-electron interaction, with the exchange enhancement factor $(1 - U D(E_F))^{-1}$. As U approaches the critical value

$$U_c = \frac{1}{D(E_F)} \tag{6.6}$$

from below, the susceptibility diverges. By approaching U_c from the side $U < U_c$, it can be spoken of a magnetic instability: The symmetrical ground state becomes unstable against the onset of ferromagnetic ordering. Equation (6.6) is called the Stoner criterion.

The Stoner criterion tells, that ferromagnetism sets in when the interaction energy reaches the order of magnitude of the kinetic energy.

It can be concluded that, it is favourable for the appearance of ferromagnetism if E_F sits in a sharp peak of $D(E)$. If $UD(E_F) - 1$ is small and $UD(E_F) > 1$, it is possible to do an expansion in powers of $UD(E_F) - 1$ to describe the properties of weak itinerant ferromagnets. 'Weak' means, that the magnetization is much smaller than the largest value which the given number of electrons could support.

A celebrated result of the Stoner theory is the description of magnetiaztion for weak itinerant ferromagnets, below T_C,

$$\frac{m^2(T)}{m^2(0)} = 1 - \left(\frac{T}{T_C}\right) \quad \text{or} \tag{6.7}$$

$$m(T) = m(0)\sqrt{1 - \left(\frac{T}{T_C}\right)^2}. \tag{6.8}$$

Note: It is possible to perform a mean field treatment also for a SDW. It leads to generalized susceptibility

$$\chi(\mathbf{q}) = (g\mu_B)^2 \frac{\chi^{(0)}(\mathbf{q})}{1 - U\chi^{(0)}(\mathbf{q})}. \tag{6.9}$$

The $\chi(\mathbf{q})$ diverges when

$$U_c\chi^{(0)}(\mathbf{q}) = 1. \tag{6.10}$$

Equation 6.10 is called the generalized Stoner criterion. The conclusion is similar to that of eq. (6.6). The system becomes unstable against the formation of a SDW with arbitrary wave vector $\mathbf{q}$, if U is large enough. This instability is also possible when U is small compared to the kinetic energy of the electrons, in contrast to the fm instability. So, it can come to a situations where both, a fm and a SDW instability are possible. Then, the instability which occurs at the lowest U_c is realized.

6.6 Origin of the ferromagnetic transition

As mentioned in section 6.3.1, the shifted higher NQR frequency of $Li_{0.9}FeAs$ compared to stoichiometric LiFeAs and the broadening of the NQR line width are clear signs which are atributed to changes in the crystal structure due to the Li deficiency. The measurements of the hall effect in section 6.3.2 hint to a more compensated charge carrier concentration in the Li deficient samples, as seen by the increase of the Hall constant. The reduction of the resistivity could come from an increase of the DOS at the Fermi level. In section 4.2 the electronic structure of LiFeAs was discussed. Typical for LiFeAs are the α hole-pockets of the Fermi surface (FS) around Z-point of the Brillouin zone (BZ) [37] (see fig. 4.3(a)). These pockets consist of hole bands which cross the Fermi energy only for certain values of k_z. The flat region of the alpha bands are critical points for the DOS, bringing the Fermi energy close to these critical points might result in the Fermi energy sitting in a peak of the DOS. As explained in section 6.5, if the Fermi energy sits in a peak of the DOS this is a favorable situation for the Stoner model [71] of weak itinerant ferromagnets. As was already stated in section 6.2.1, the susceptibility curve of $\mathrm{Li_{0.9}FeAs}$ can be described by the Stoner model for weak ferromagnets. Also, the FMR data can be fitted by a mean field theory predicting conventional ferromagnetism (see section 6.2.2) and the DMS data of sec.6.2.4 can also be interpreted as an example of an itinerant ferromagnet.

So, it might be possible that Li deficiency is increasing the DOS at the Fermi level, which can make the system instable against the onset of ferromagnetic ordering. Thus, the results support Brydon et al. [12] who stated, that LiFeAs is close to an fm instability. More samples are needed to further qualify this statement. Here the distinctive qualities of NQR measurements, shown in section 6.3.1, are useful to check for possible candidates for further experiments.

The sensitivity of the NQR frequency to the stoichiometric changes which has already been seen by Baek et al. [43], give the opportunity to form a phase diagram of the superconducting and the fm phase transitions. This phase diagram consists of the transition temperature versus the NQR frequency and can be seen in fig. 6.13.

All samples which undergo the fm phase transition show an NQR frequency which is higher than 21.71 MHz at room temperature. The NQR frequency can therefore, be taken as a tool to make predictions on the physical properties of a LiFeAs derivative.

As can be seen in fig. 6.13, there is a quite big gap between the superconducting and fm samples in the phase diagram. The aim of the following chapters is to close this gap and present a complete superconducting and fm phase diagram of Li deficient LiFeAs derivatives.

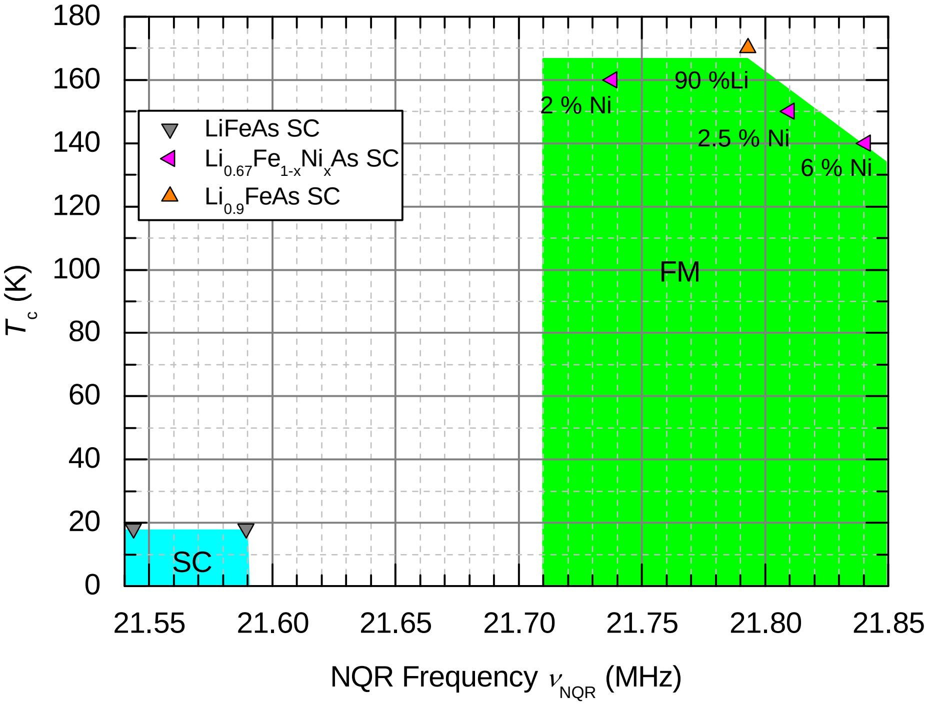

Figure 6.13: Superconducting and ferromagnetic phase diagram of $Li_{1-y}Fe_{1-x}Ni_xAs$ built by nuclear quadrupole resonance. All frequencies were taken at room temperature. The two superconducting samples are the same as in ref. [43]. Measurements done by S.-H. Baek, H.-J. Grafe and F. Hammerath.

7 Nuclear Quadrupole Resonance as Tool for the Optimization of LiFeAs Synthesis

The physical properties of LiFeAs are very sensitive to stoichiometric changes as shown by Baek et al. [43]. Furthermore, superconductivity can be suppressed very easily by off-stoichiometry [10]. To understand the sensitivity of LiFeAs to stoichiometric changes, it is necessary to perform controlled studies on doping and off-stoichiometry.

There are several methods for synthesizing LiFeAs. They differ tremendously in heating conditions ranging from 700 °C up to 1500 °C [8, 9, 52, 56, 58, 59, 67, 90]. However, the most common heating temperature in use is $\approx$ 800 °C for polycrystals [56, 67]. For single crystals usually temperatures from 1050 °C to 1500 °C are taken. However, doping series in single crystals are highly complicated, especially due to the high reactivity of Li at these temperatures which makes compositional control of LiFeAs a difficult task. Polycrystals are easier to handle due to their lower synthesis temperatures. In literature, only Pitcher et al. [7], Tapp et al. [8], and Wang et al. [9] report on the synthesis of polycrystalline LiFeAs so far.

The resulting physical properties of these samples vary as much as their production conditions do. Superconducting transition temperatures T_c are reported in the range from 14 K to 19.2 K [8, 9, 52, 58, 59, 90] which might be caused by the different synthesis procedures resulting in off-stoichiometry and impurity phases.

Therefore, an optimization for the synthesis process of stoichiometric LiFeAs polycrystals is needed to get a controlled starting point for further experiments on the stoichiometry of LiFeAs. Polycrystals were taken for these experiments, because it is easier to change the stoichiometry of a polycrystal than for single crystals.

This chapter will present a nuclear quadrupole resonance (NQR) study on such an optimization process which, together with other techniques, demonstrates that the optimal heating temperature to get maximum T_c with sharp transitions and high quality polycrystals is $\approx$ 600 °C. The results of this study were published in ref. [91].

7.1 Sample Preparation

For this study, samples of polycrystalline stoichiometric LiFeAs were synthesized. The development of the synthesis routine and the execution of the synthesis were done by Shiv J. Singh and Robert Beck [91]. The synthesis was done in a three-step process, which was the same for every sample, except for the synthesis temperature T_{synth}. For each sample T_{synth} was set to one temperature out of the range from 200 °C to 900 °C.

Step one started by mixing the starting reagents with each other. The starting reagents were Li and FeAs both in a purity of 99.99 %. After mixing, the reagents were put into a Al_2O_3 (alumina) crucible, which was then put into a Nb container, which was welded for sealing. Afterwards, the reagents were heated to 200 °C and the temperature was kept constant for 12 h. The outcome is a grey powder. The low temperature was chosen to overcome the high reactivity of Li and its low melting point of 180 °C.

In step two, the powder was pressed into pellets by uniaxial pressure of 5 MPa. The pellets were again put into an alumina crucible and a Nb container and were heated up to T_{synth} and the temperature was kept constant for 45 h. The outcome were brittle pellets with lots of cracks.

Subsequently, step three was used to reduce the amount of cracks in the pellets. Therefore, the pellets were ground, again pressed into pellets, and put into the alumina and Nb containers, followed by the heating process up to T_{synth} and the temperature was kept constant for 2 h. After the heating, the samples were cooled by furnace cooling.

To optimize the cooling process after finding the optimal T_{synth}, the cooling time was varied between $1\,\frac{\text{K}}{\text{min}}$, $0.3\,\frac{\text{K}}{\text{min}}$ and $0.1\,\frac{\text{K}}{\text{min}}$ in the third step for the optimal T_{synth}. Since the slowest rate showed the best results, only measurements for this rate are shown, which is denoted as the *slow cooling rate*.

7.2 Nuclear Quadrupole Spectroscopy

To get information about the sample quality of the synthesized samples, NQR measurements were performed. As stated in chapter 2, NQR is sensitive to structural changes in the environment of the chosen nucleus. For this study ^{75}As was chosen. On structural disorder, the NQR spectrum should show a broadening of the resonance line and for stoichiometric changes like deficiencies or doping effects the resonance line would be shifted compared to the resonance line of a stoichiometric compound. Exactly such a behavior of line broadening and shifting can be seen by the comparison of the resonance lines of LiFeAs samples synthesized at different T_{synth}.

In fig. 7.1(a) spectra for different T_{synth} are shown. All samples exhibit a single resonance line. Samples which were synthesized with $T_{\text{synth}} \leq 800$ °C have a resonance line, with its

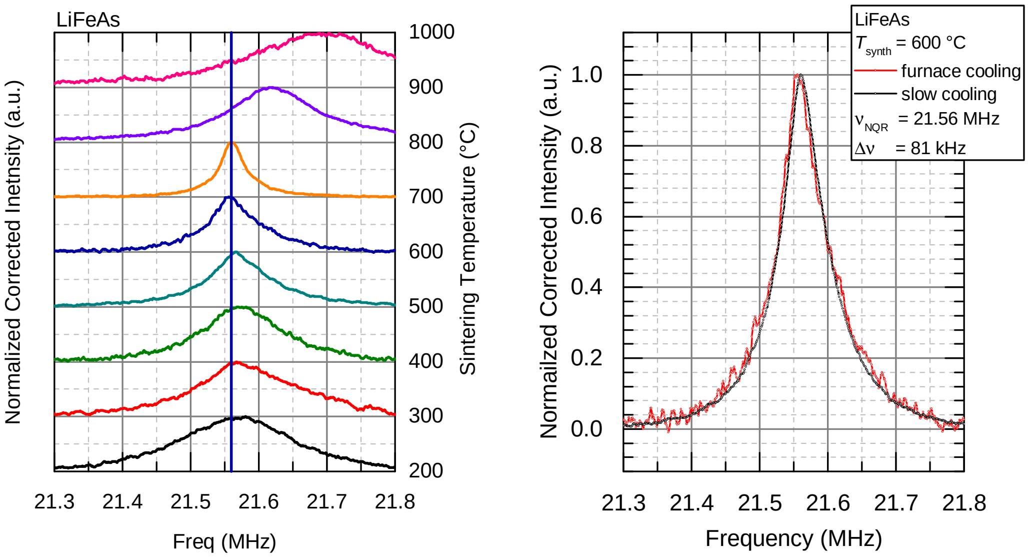

(a) NQR spectra of stoichiometric LiFeAs synthesized at different temperatures T_{synth}. The frequency of 21.56 MHz is marked by a dark blue line.

(b) NQR spectra of stoichiometric LiFeAs synthesized at $T_{\text{synth}} = 600\,^{\circ}\text{C}$ cooled by furnace and slow cooling. Note, that the difference in noise level is not a matter of sample quality but of measurement time (see section 5.2.3).

Figure 7.1: Nuclear quadrupole resonance (NQR) spectra at different synthesis temperatures and cooling rates.

maximum position at $\sim 21.56\,\text{MHz}$. For higher T_{synth}, the maximum position is shifted to higher frequencies. Also, the spectra are more and more asymmetric for samples which were synthesized at temperatures which are farther away from 600 °C. Not only they are more asymmetric, they also show a broader line width.

For further quantification of this behavior, the center of spectral weight (CSW) as a measure of NQR frequency ν_{NQR} (see section 5.2.3) and the full width at half maximum (FWHM) as a measure for the line width $\Delta\nu$ were calculated for every spectrum. The results can be seen in fig. 7.2.

The behavior of the resonance line is mimicked by the NQR frequency, fig. 7.2(a). Starting at $T_{\text{synth}} = 200\,^{\circ}\text{C}$ ν_{NQR} stays more or less constant around $\sim 21.56\,\text{MHz}$, but a small decrease is visible. The minimum frequency is then at $T_{\text{synth}} = 700\,^{\circ}\text{C}$ with $\nu_{\text{NQR}} = 21.562(2)\,\text{MHz}$. At higher T_{synth}, ν_{NQR} is increasing drastically. The shift of ν_{NQR} with different T_{synth}, especially the drastic shift for $T_{\text{synth}} \geq 800\,^{\circ}\text{C}$, is a sign for a changed stoichiometry of the sample. These changes may be caused, e.g. by Li deficiencies. Due to the higher temperatures, the reactivity of Li increases and it might diffuse out of the structure.

Taking a look on the line width, fig. 7.2(b), it is visible, that by increasing T_{synth} the

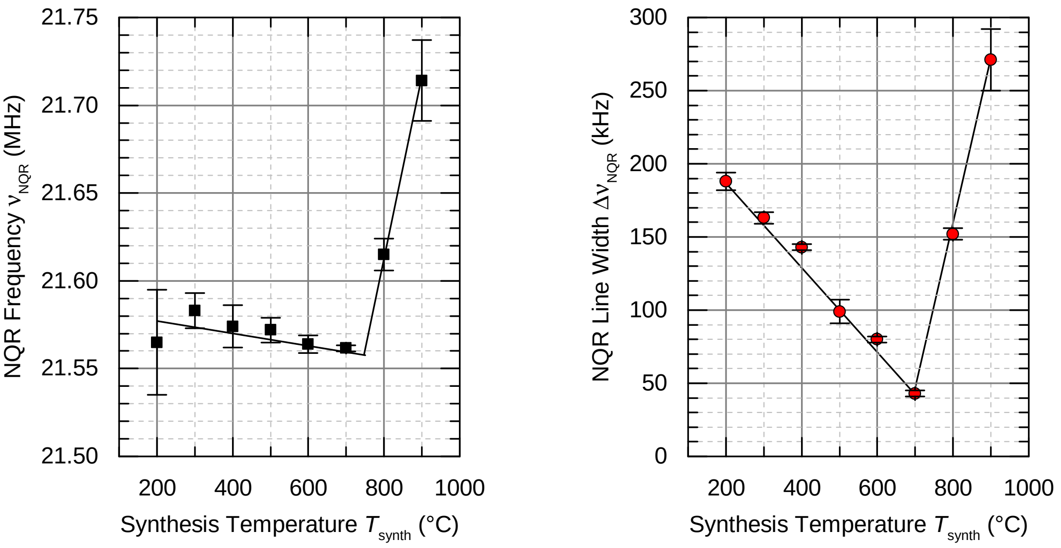

(a) NQR frequency ν_{NQR} derived from the center of spectral weight (CSW). The black solid line is a guide to the eye.

(b) NQR line width $\Delta\nu$ derived from the full width at half maximum (FWHM). The black solid line is a guide to the eye.

Figure 7.2: NQR frequency and NQR line width for different synthesis temperatures T_{synth}.

line width decreases until it reaches its minimum of $\Delta\nu = 43\,\mathrm{kHz}$ at $T_{\mathrm{synth}} = 700\,°\mathrm{C}$. For higher $T_{\mathrm{synth}} \geq 800\,°\mathrm{C}$, $\Delta\nu$ increases much stronger than it decreased for $T_{\mathrm{synth}} \leq 700\,°\mathrm{C}$. The decrease of $\Delta\nu$ is a sign of homogenization of the lattice structure with higher T_{synth}. The increase of $\Delta\nu$ for higher $T_{\mathrm{synth}} > 700\,°\mathrm{C}$ is then having the opposite effect. That the increase for the high T_{synth} is larger than the decrease for the low T_{synth}, can be assigned to the additional change of stoichiometry, which is further increasing the line width.

Thus, by increasing T_{synth} the homogeneity of LiFeAs samples can be improved, resulting in a reduced line width of the NQR resonance line. From the NQR point of view, the optimal T_{synth} is 700 °C, which gives a resonance frequency of 21.562(2) MHz at a line width of 43 kHz. The NQR frequency compares well with measurements of other groups(21.57 MHz [52],21.54 MHz[43]) (see section 4.5) and the line width is that small that it can even compete with that of single crystals.

As it was stated in section 7.1, not only T_{synth} was optimized, but also the cooling rate. To compare the effects of the cooling rates with each other, another NQR spectrum was measured for the slow cooling rate. In fig. 7.1(b), a comparison of spectra between furnace cooling and slow cooling is shown. It can be seen, that there is no difference visible between the two spectra, i.e. from the NQR point of view, both samples are indistinguishable from each other. The next section will show that the slow cooling rate is preferable because it has

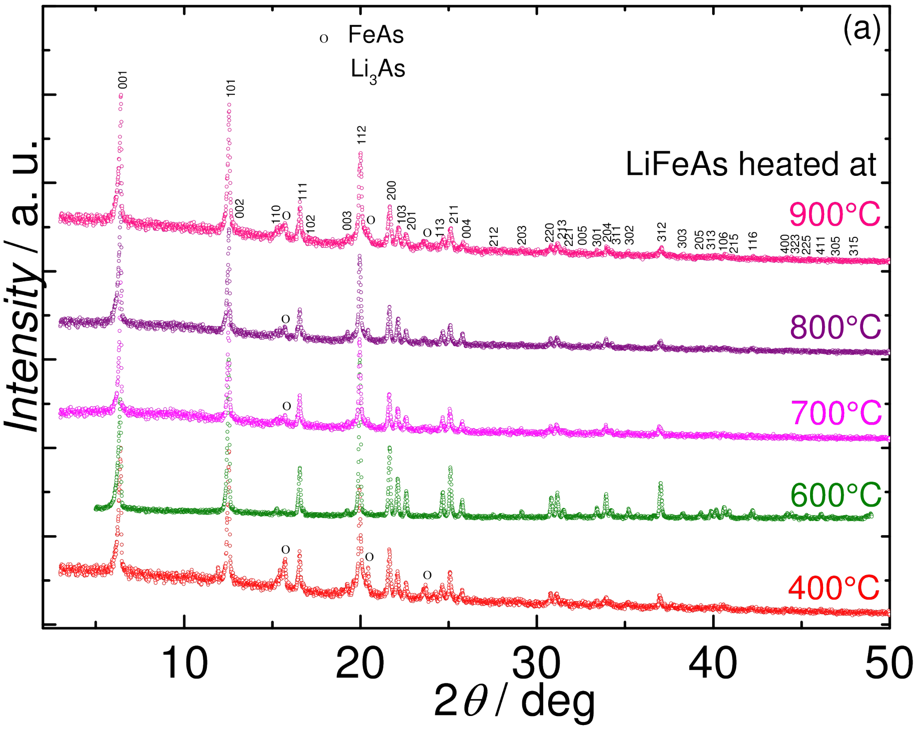

Figure 7.3: Powder X-ray diffraction patterns of LiFeAs heated to 400 °C, 600 °C, and 900 °C [91].

an influence on macroscopic effects, like grain size or inter-grain connectivity. Such effects do not have an influence on NQR measurements, since they do not change the local charge environment of the ^{75}As nucleus.

Despite that NQR is showing an optimum $T_{\mathrm{synth}} = 700\,^{\circ}\mathrm{C}$ other methods draw a different picture, which can be seen in the next section. They propose an optimal $T_{\mathrm{synth}} = 600\,^{\circ}\mathrm{C}$.

7.3 Other Sample Characterization

Besides the NQR measurements the synthesized samples were characterized by X-ray diffraction (XRD), static magnetic susceptibility (SMS), and resistivity measurements. All these measurements were performed by Shiv J. Singh [91]. This section will shortly present the results of these measurements.

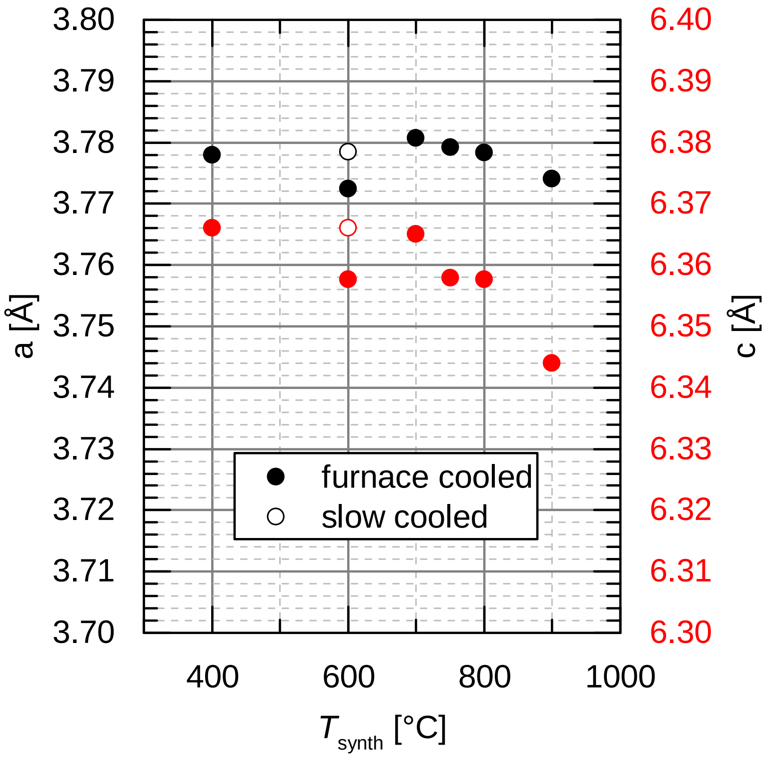

Figure 7.4: Lattice Parameters of LiFeAs prepared at different synthesis temperatures [91, Tab. 1].

7.3.1 Powder X-Ray Diffraction

Beginning from T_{synth}= 200 °C, the typical Cu_2Sb-structure of LiFeAs can be found in the refinement of the XRD patterns (fig. 7.3). This holds true for all T_{synth}. For values T_{synth} lower than 600 °C, a considerable amount of the impurity phases Li_3As and FeAs can be found. The amounts of these impurity phases decrease with increasing T_{synth} until reaching 600 °C. The impurity phases start to reappear for T_{synth}-values higher than 600 °C.

The appearance of foreign phases for all T_{synth}, except for 600 °C shows that 600 °C is the optimal temperature, from the XRD point of view.

The lattice parameters found through the refinement (see fig. 7.4) show almost constant behavior for all T_{synth} below 700 °C. At 900 °C a slight decrease of the c-lattice constant was found.

The constant lattice parameters for all T_{synth} below 600 °C show, that already at lower temperatures a stoichiometric LiFeAs phase is formed. The decreasing lattice constant c at T_{synth} = 900 °C can be explained by stoichiometric changes of the lattice structure of LiFeAs. These might originate from Li deficiencies, caused by the increased reactivity of Li at higher T_{synth}.

7.3.2 Magnetization

Measurements of the magnetization at $H = 20\,\mathrm{Oe}$ show a paramagnetic (pm) background for samples synthesized for T_{synth} below 600 °C, as can be seen by the offset from zero in fig. 7.5. This background is reduced with increasing T_{synth} up to 700 °C. For T_{synth} up to 700 °C all samples show a superconducting transition at $T_c = 18\,\mathrm{K}$. The transition width of the superconducting transition decreases with increasing T_{synth} until it reaches its minimum at 600 °C. The sharp transition temperature for $T_{\mathrm{synth}} = 600\,°\mathrm{C}$ is consistent with reports of single crystals of other groups [52, 58, 59]. For $T_{\mathrm{synth}} \geq 800\,°\mathrm{C}$ T_c is strongly reduced to $\sim 10\,\mathrm{K}$.

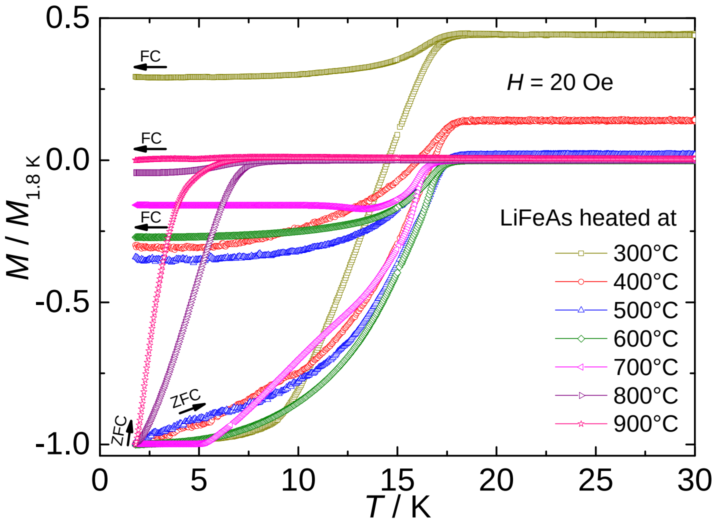

Figure 7.5: Temperature dependency of the normalized magnetization ($\frac{M}{M_{1.8\,\mathrm{K}}}$) measured with zero-field-cooling (ZFC) and field cooling (FC) mode for $H = 20\,\mathrm{Oe}$ of polycrystalline LiFeAs heated at 300-900 °C [91].

The pm background of $T_{\mathrm{synth}} < 600\,°\mathrm{C}$ might stem from impurity phases, which are reduced on increasing T_{synth} up to 600 °C, which can be seen by the decreasing pm background. All samples with $T_{\mathrm{synth}} \leq 700\,°\mathrm{C}$ show the same T_c of $\sim 18\,\mathrm{K}$, which is the same as it is known for stoichiometric LiFeAs. Therefore, these samples most probably include a phase of stoichiometric LiFeAs which is big enough to dominate the magnetic behavior of the samples. But the superconductivity is disturbed by the impurity phases which can be seen in the broadened superconducting transition width, which gets smaller by increasing T_{synth} up to 600 °C. For $T_{\mathrm{synth}} = 600\,°\mathrm{C}$ the smallest transition width is observed. Here, the superconductivity is the least disturbed by impurities. That the transition width is comparable with single crystals of stoichiometric LiFeAs is a sign of the high purity of the 600 °C-sample.

The reduction of T_c at T_{synth}-values higher than 700 °C could stem from the formation of a new phase carrying the superconductivity with a lower T_c. The fact that most of the sample becomes superconducting at the lower T_c and nothing can be seen of the higher T_c anymore can be interpreted such, that the new phase is completely replacing the former phase. Thus, it is not an additional impurity phase, but a replacement of the stoichiometric LiFeAs phase.

7.3.3 Resistivity

The resistivity data for all T_{synth} show a typical metallic behavior (see fig. 7.6(a)). For all samples synthesized below $T_{\text{synth}} = 800\,°\text{C}$, the sample synthesized at 600 °C shows the lowest resistivity. It is even smaller than the resistivity reported for other polycrystals [8, 9]. On the other hand, the two samples synthesized at 800 °C and 900 °C show a lower resistivity at 300 K than all other samples.

In fig. 7.6(b) the results for the resistivity measurements for the low temperature regime normalized at 300 K, are shown. Here, it shows that all samples which were prepared at different T_{synth} than 600 °C show a higher residual resistivity. Comparing the residual resistivity ratio (RRR) for all samples (see fig. 7.7 top) it becomes apparent that the sample synthesized at 600 °C shows the highest value of RRR.

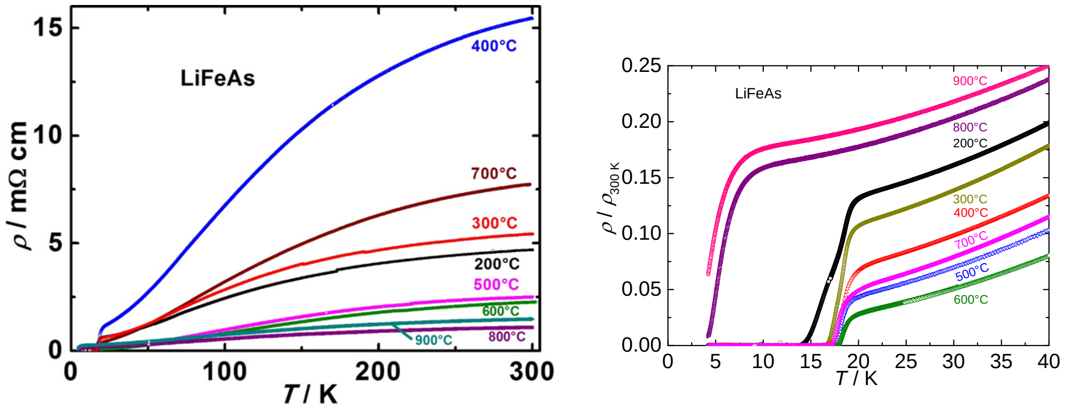

(a) Temperature dependency of the resistivity for the polycrystalline LiFeAs samples synthesized at T_{synth} of 200-900 °C prepared with furnace cooling.

(b) Low-temperature region of the normalized resistivity is shown for all samples prepared with furnace cooling.

Figure 7.6: Resistivity data of LiFeAs for different T_{synth} [91].

Since impurity phases are a typical reason to increase the residual resistivity of a sample, the effect of the increasing residual resistivity in fig. 7.6(b) for all T_{synth} other than 600 °C is a clear sign that the sample prepared at 600 °C has the lowest amount of impurity phases. Also the RRR which is the highest for the 600 °C-sample clearly shows that this sample has the highest purity compared to the samples synthesized at other temperatures. It is even comparable with RRRs of single crystals [39].

The decrease of the resistivity for the two samples prepared at 800 °C and 900 °C is surprising. Although, they show an increased residual resistivity and, therefore, a higher amount of impurities their high temperature resistivity is decreased compared to the sample synthesized at 600 °C. The reduction of the high temperature resistivity must originate from other effects than impurity. They could be a sign of a change of the stoichiometry of the sample. Such a reduction of the high temperature resistivity can also be seen in the ferromagnetic LiFeAs (see section 6.3.2) and the reasons for the reduction might be similar. The next chapter will provide further insight into the subject of the reduced high temperature resistivity.

Comparing the superconducting properties of all samples shows, that the onset temperature of superconductivity for all samples prepared at $T_{\text{synth}} \leq 700\,^{\circ}\text{C}$ lies at $T_{\text{onset}} \sim 19.1\,\text{K}$, but for samples prepared at $T_{\text{synth}} \geq 800\,^{\circ}\text{C}$, T_{onset} is around $\sim 10\,\text{K}$. The sample synthesized at $T_{\text{synth}} = 600\,^{\circ}\text{C}$ shows the highest mid-point superconducting transition temperature $T_{\text{mid}} = \frac{T_{\text{onset}}+T_{\text{offset}}}{2}$ (see fig. 7.7(middle)) and the lowest transition width $\Delta T_c = T_{\text{onset}} - T_{\text{offset}}$, fig. 7.7(bottom).

The small variation of T_{onset} within all samples synthesized at temperatures below 800 °C is an indication for the development of the structure carrying the superconductivity even at low T_{synth}. The sudden decrease of T_{onset} for higher T_{synth} is a sign that the higher T_{synth} induces processes which destroy the superconductivity in LiFeAs. One of these processes could be the development of Li deficiencies in these sample, which are known to suppress the superconductivity [10]. T_{mid} and ΔT_c again clearly show that the optimum temperature for synthesizing superconducting LiFeAs polycrystals lies in the order of $\sim 600\,^{\circ}\text{C}$.

7.4 Discussion

It was shown by the methods of NQR, XRD, SMS, and resistivity that changes of the synthesis temperature T_{synth} of polycrystalline LiFeAs samples have a very strong effect on the sample quality. By increasing T_{synth} starting from 200 °C, the sample quality is increasing, which can be seen by a decreasing NQR line width, section 7.2, reduction of impurity phases in XRD, section 7.3.1, a decrease of pm background and superconducting transition width in SMS, section 7.3.2, and by the increase of the RRR, the midpoint of the superconducting transition T_{mid} and the decrease of the superconducting transition width ΔT_c in resistivity measurements, section 7.3.3.

It is interesting to see that the formation of a phase of stoichiometric LiFeAs already starts at 200 °C, which can be seen in the XRD-pattern and by the NQR-frequency, which is already comparable to typical LiFeAs specimen [43, 52]. The only T_{synth} at which a synthesis of a phase-pure stoichiometric superconducting sample of LiFeAs is possible is for 600 °C. Here, the XRD-pattern does not show signs of impurity phases and the NQR line width

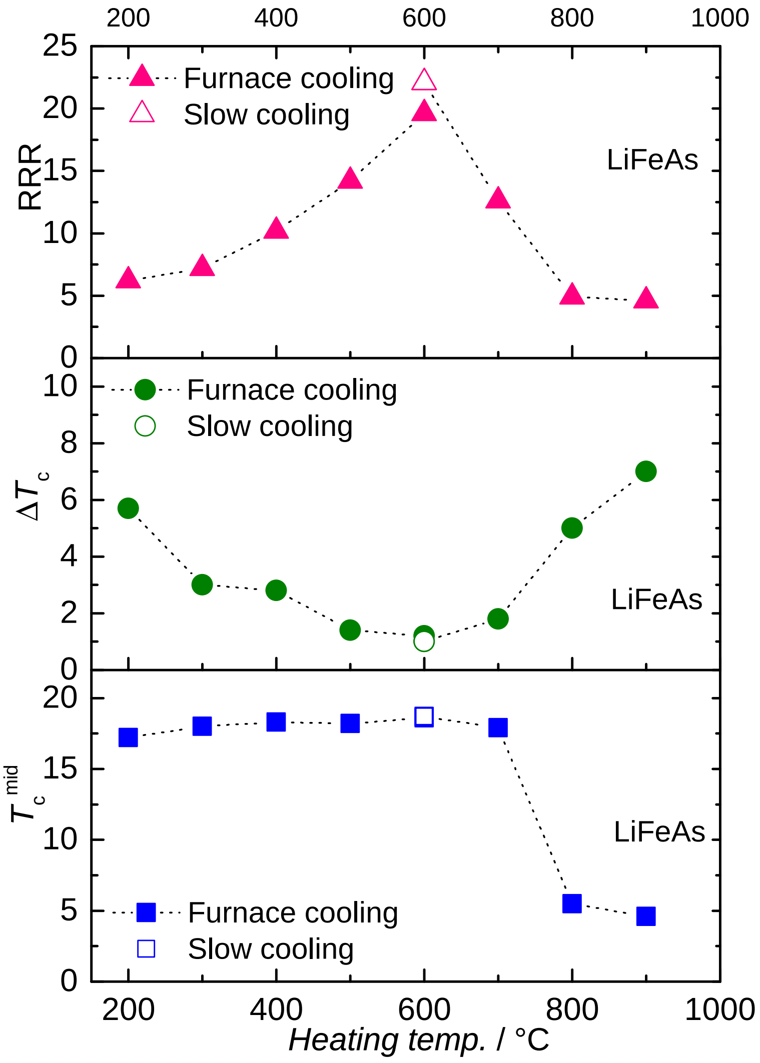

Figure 7.7: dependency of the mid-transition temperature (T_{mid}), transition width (ΔT_c), and residual resistivity ratio ($RRR = \frac{\rho_{300\,\mathrm{K}}}{\rho_{30\,\mathrm{K}}}$) from the synthesis temperature [91].

reaches very low values. Although, the sample for $T_{\mathrm{synth}} = 700\,°\mathrm{C}$ shows the smalles NQR line width, 600 °C was chosen as the optimal synthesis temperature. The small line width of the 700 °C-sample clearly shows that the phase of LiFeAs in this sample has the lowest amount of impurities, but this sample does not have the lowest amount of foreign phases. The superconducting transition width, which is strongly influenced by foreign phases has the smallest values for $T_{\mathrm{synth}} = 600\,°\mathrm{C}$ in both SMS and resistivity measurements. Also the RRR is maximized for this T_{synth}. These optimized polycrystals can easily compare if not compete with single crystals of stoichiometric LiFeAs in all stated properties, see tab. 7.1 for further details. Thus, the optimized samples are a good starting point for further doping studies of LiFeAs.

Another interesting aspect are the samples synthesized at temperatures higher than

Table 7.1: Comparison of the physical properties of the optimized sample synthesized at $T_{\mathrm{synth}} = 600\,°\mathrm{C}$ with published data for stoichiometric LiFeAs single crystals.

Method	**Property**	**Optimized sample**	**Literature**
NQR	ν_{NQR}	21.564(5) MHz	21.57 MHz [52]
	$\Delta\nu$	80(2) kHz	64-80 kHz [43, 52]
Resistivity	T_{mid}	18.6 K	$\sim$ 18 K [39]
	ΔT_c	1.2 K	$\sim$ 0.9 K [39]
	RRR	19.6	24, 20 [61, 62]

700 °C. These samples show signs of a different stoichiometry than the samples synthesized at temperatures below 800 °C. Hints for the different stoichiometry are the drastic shift of the NQR resonance line and the decrease of the lattice constant c, as seen by XRD. Also the superconducting transition temperature T_c is strongly suppressed by nearly a factor of 2, for these samples, as can be seen by magnetization and resistivity. One reason for these stoichiometric changes might be Li deficiencies. They could arise due to the higher synthesis temperature, which would increase the reactivity of Li. Therefore, the Li could react with other components than the reagents, e.g. oxygen of the alumina. The effect of Li deficiency is discussed in more detail in the next chapter.

8 Physical Properties of Off-Stoichiometric LiFeAs

As it was shown in the previous chapters, the properties of LiFeAs are very sensitive to small stoichiometric changes. Li-deficiency is reducing the superconducting transition temperature T_c [10] and even single crystals from the same batch show differences in their superconducting behavior, which can be seen by Knight shift measurements [43]. It is possible to distinguish LiFeAs-samples by their different nuclear quadrupole resonance (NQR) frequencies (see section 4.5).

Not only the superconducting behavior of LiFeAs reacts strongly on off-stoichiometry. As it was shown in section 6.3.2 (fig. 6.12), one Li-deficient sample shows a strongly reduced room temperature resistivity compared to stoichiometric samples. This sample also develops a ferromagnetic (fm) phase transition and shows an increased NQR frequency compared to a stoichiometric sample (see section 6.3.1, fig. 6.10).

This strong sensitivity makes it worthwhile to prepare a systematic study on different off-stoichiometries on LiFeAs. In this chapter such a study is presented. It will show results of NQR, resistivity, X-ray diffraction (XRD) and static magnetic susceptibility (SMS) measurements on 24 different samples with different types of off-stoichiometry.

By investigating the behavior of off-stoichiometric LiFeAs, it was possible to connect Fe excess on LiFeAs with an increasing NQR frequency and to use this connection to supplement the phase diagram of of (fig. 6.13).

Measurements of the electrical resistivity reveal that Fe-excess reduces the high temperature resistivity in a very similar fashion as the Li-deficient sample fig. 6.12. Such behavior of the resistivity gives hints that the underlying mechanism to produce such reduction might be very similar to the mechanism responsible for the development of ferromagnetism in LiFeAs (see section 6.6).

The results of this chapter will be published in [92].

8.1 Sample Preparation

For this study 24 different polycrystals were synthesized by Shiv J. Singh using the three-step-method of Singh et al. [91] described in section 7.1. The samples were synthesized in four different sets with different types of off-stoichiometry.

The first set, in the following referred to as series X, are 5 samples of $Li_{1-x}FeAs$ with a varying nominal Li content x which is ranging from $x = 2\,\%$ to $30\,\%$. The second set, referred to as series Y, are 11 samples of $Li_{1-x}Fe_{1+x}As$ with different nominal contents of Li deficiency and Fe excess ranging from $x = 1\,\%$ to $15\,\%$. The third set, referred to as series Z, are 5 samples of $LiFe_{1+x}As$ with a varying nominal content of Fe excess only, ranging from $x = 2\,\%$ to $20\,\%$. And the last set, referred to as series W, is a series of 3 samples of $LiFeAs_{1-w}$ with a varying nominal As content w ranging from $w = 3\,\%$ to $10\,\%$.

Changes to the synthesis routine described in section 7.1 are, that additionally to the reagents, elemental Li, Fe and As with a purity of 99.99 % were taken into account for the wanted type of off-stoichiometry.

After synthesis, phase indication and structural investigations were done on the samples with XRD by Shiv J. Singh. The results were used to perform calculations of the lattice parameters by refining the data with the Rietveld method [93] using the Fullprof suite [94], also done by Shiv J. Singh.

The magnetic properties of the sample were checked by Shiv J. Singh, with SMS by using a Quantum Design Magnetic Properties Measurement System (MPMS-5T) with different magnetic fields in the temperature range from 1.8 K to 300 K under zero-field cooled (ZFC) and field cooled (FC) conditions.

Measurements of NQR and resistivity were performed as described in chapter 5.

8.2 Nuclear Quadrupole Resonance

For every sample of each set, measurements of the ^{75}As-NQR-spectrum at room temperature were performed. The resonance lines resulting from these measurements can be seen in fig. 8.1. A qualitative look on the different spectra reveals, that there are distinct differences between the different series.

The most notable difference can be seen in the comparison of the spectra of series X with series Y and Z. Both, in series Y and Z a shift of the resonance line to higher frequencies and a line-broadening can be seen with increasing x. While for series X there is neither a shift visible nor a broadening. All resonance lines in series X look the same for every chosen x up to $x = 30\,\%$.

Thus, all samples of series X are indistinguishable from each other in the NQR point of view. To get conditions where different samples show the same resonance line in NQR,

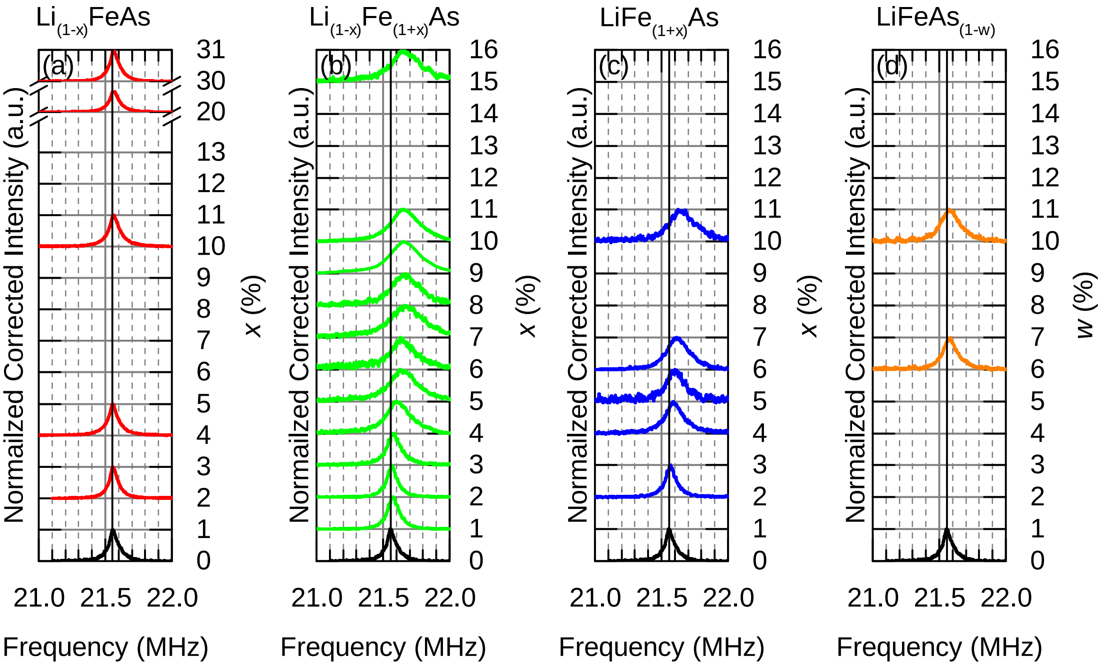

Figure 8.1: Nuclear quadrupole resonance (NQR) spectra for all series of off-stoichiometric LiFeAs. (a) Series X, (b) series Y, (c) series Z and (d) series W. The intensities of each spectrum are corrected by means of frequency and temperature and are normalized to the maximum intensity. The extracted NQR frequency of the stoichiometric compound, shown in black, is marked by a vertical solid black line.

the samples have to have the same electric field gradient (EFG) and the same asymmetry parameter (see eq. (2.17) in section 2.3). This is only possible if the samples have the same structural symmetry. So, although all the samples of series X were produced with a different nominal Li concentration, all the samples show the structure of stoichiometric LiFeAs.

A possible explanation could be, that in the synthesis process the missing Li is not leading to the formation of a modified LiFeAs structure with Li deficiencies, but to the formation of foreign phases of other structures and a phase of stoichiometric LiFeAs without deficiencies.

Thus, the amount of the stoichiometric phase is only shrinking in comparison to a sample without foreign phases, which cannot be seen in the normalized NQR spectra of fig. 8.1(a).

For the series Y and Z, the resonance line shifts with increasing x to higher frequencies and additionally the resonance line broadens. The shift of the resonance line can be explained by a change of the EFG of the samples, caused by a different structure of the samples with higher x. In contrast to series X, series Y and Z show a reaction on the changed stoichiometry caused by the synthesis with less amount of Li and/or higher amount of Fe compared to the stoichiometric sample. The line broadening is an additional confirmation that there really is a change of stoichiometry present. Due to excess or deficiency effects,

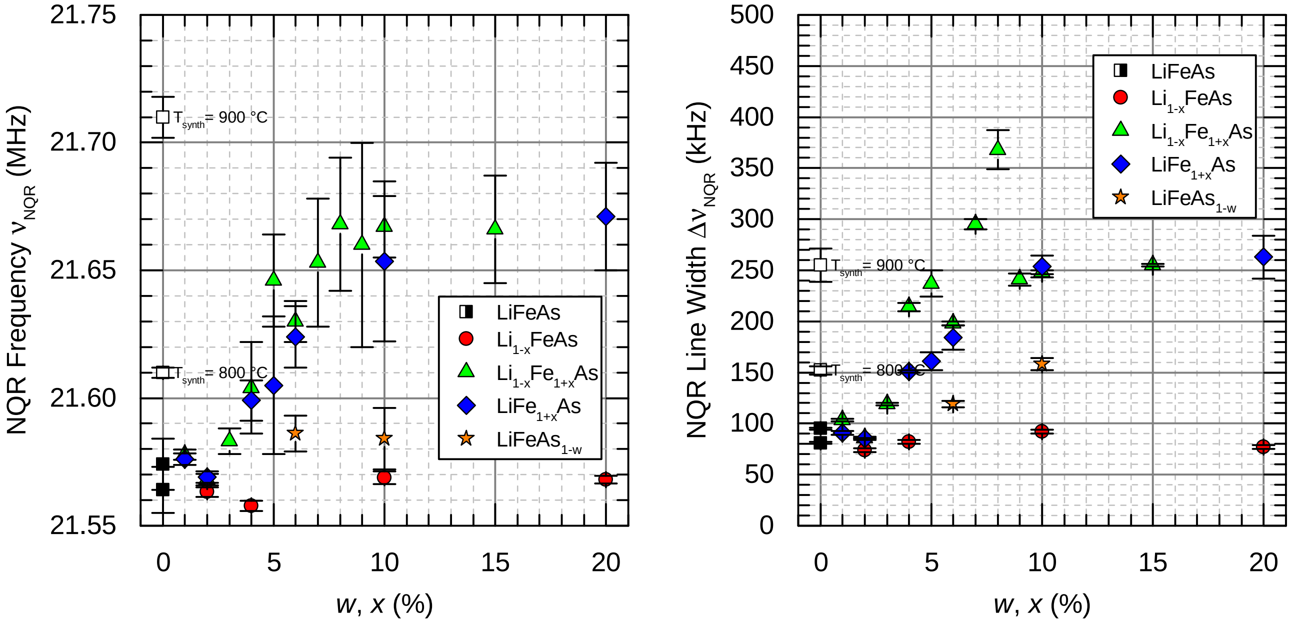

(a) NQR frequency ν_{NQR}

(b) NQR line widths $\Delta\nu_{\mathrm{NQR}}$

Figure 8.2: Nuclear quadrupole resonance frequency (NQR) ν_{NQR} and line widths $\Delta\nu_{\mathrm{NQR}}$ for the spectra shown in fig. 8.1 versus their nominal contents of Li, Fe, and As (w, x). (black □) stoichiometric samples with different sintering temperatures T_{synth}; (red ∘) series X; (green △) series Y; (blue ⋄) series Z; (orange ⋆) series W.

lattice distortions occur in the structure. These distortions lead to a distribution of different EFGs which cause the broadening.

For series W, there is also a shift visible with increasing w, but it seems to be smaller than for series Y and Z. Also a broadening of the resonance line can be seen. The reasons are most probably the same as for series Y and Z.

So, it is possible to change the stoichiometry of LiFeAs. To see if these changes happen in a systematic way, the shift of the resonance line and the line-broadening were quantified. For each spectrum the center of spectral weight (CSW), as a measure for the NQR frequency ν_{NQR}, and the full width at half maximum (FWHM), as a measure of the line width $\Delta\nu$, was calculated, as described in section 5.2.3. The resulting values are visualized in fig. 8.2.

The behavior of the resonance lines seen in fig. 8.1(a) for series X can also be seen with ν_{NQR} and $\Delta\nu$. Both values show a constant behavior for increasing values of x. Thus, they fit very well in the picture of the unchanged but shrinking phase of stoichiometric LiFeAs.

The slight shift of the resonance lines for series W, as can be seen in fig.8.1(d), are reproduced in its ν_{NQR}, but the shift is so small that it looks more or less constant by taking into account the error bars. With only two data points, further conclusions on samples which were synthesized with a lower amount of As are only speculations. More samples are needed to get a more clear picture of this series.

In ν_{NQR} series Y and Z show an almost identical behavior. With increasing x, for both series ν_{NQR} is increasing linearly until it saturates for values of $x > 10\,\%$ on $\nu_{\mathrm{NQR}} \sim 21.67\,\mathrm{MHz}$. As stated above, the shift of the resonance line and, therefore, the ν_{NQR}, is a sign of a changed electronic environment of the ^{75}As-nucleus, probably caused by an altered structure. Due to the fact that the lower Li content of series X has no influence on the stoichiometry of the LiFeAs phase and the fact that series Y and Z show an identical behavior of ν_{NQR}, the origin of the altered stoichiometry can be accounted to the synthesis with additional Fe. Thus, it seems probable that the stoichiometry of the samples of series Y and Z show rather an excess of Fe than a deficiency of Li.

The aspect that ν_{NQR} is saturating for x higher than $10\,\%$ shows that Fe excess can be induced in LiFeAs only to a certain extent, at least with the synthesis method described in section 8.1.

The line width of fig. 8.2(b) shows a very similar picture. It also increases linearly with increasing x and it is saturating at $\Delta\nu \sim 250\,\mathrm{kHz}$ for $x > 10\,\%$, too. Thus, it supports the assumption of the altered stoichiometry due to Fe excess.

The NQR frequencies for samples of the optimization study in chapter 7 [91] can be seen from another point of view, now. The two samples synthesized with $T_{\mathrm{synth}} = 800\,°\mathrm{C}$ and $900\,°\mathrm{C}$ show a high NQR frequency compared to the samples synthesized at $T_{\mathrm{synth}} = 600\,°\mathrm{C}$ (see fig. 7.2(a) and also fig. 8.2(a)). The ν_{NQR} of the 900 °C-sample is even higher than the saturation frequency. With the connection of the NQR frequency with the amount of Fe excess, it seems probable that these two samples with high synthesis temperatures developed a high amount of Fe excess, which might even be higher than the amount produced by samples synthesized with additional Fe of $x = 10\,\%$.

The connection of the NQR frequency with the amount of Fe excess shows, that the higher the Fe excess in the off-stoichiometric samples is, the higher is the NQR frequency. Thus, ν_{NQR} can be taken as a measure of the Fe excess. In the following sections the NQR frequency will be used to assign the samples to their amount of Fe excess.

8.3 X-Ray Diffraction

Pitcher et al. [10] performed a combined X-ray and neutron diffraction study on $\mathrm{Li}_{1-y}\mathrm{Fe}_{1+y}\mathrm{As}$. They were able to calculate the amount of Fe excess and Li deficiency y by refining their diffraction data. From the refinement, they also extracted the unit cell volume and found that it is linearly decreasing with increasing y (see fig.8.3).

Because of the similarity of series Y with the samples from Pitcher et al. [10], it is inter-

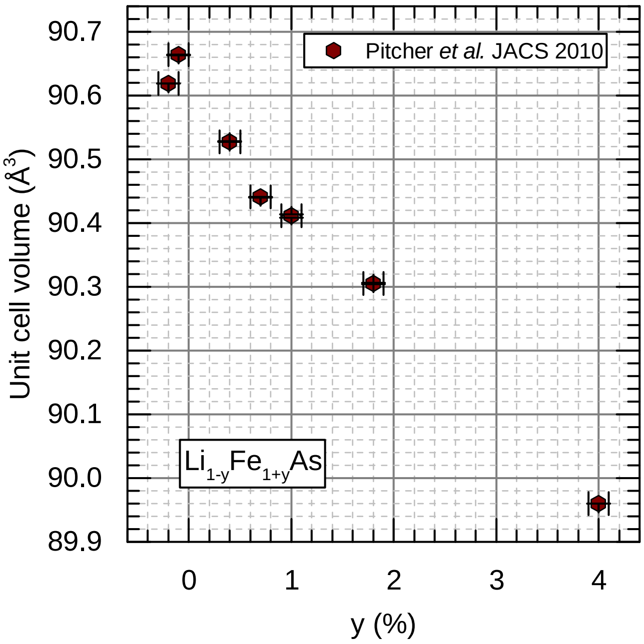

Figure 8.3: Unit cell volume plotted against refined occupancy y refined from joint X-ray diffraction (XRD) and neutron diffraction refinements. Reproduced from [10].

esting to compare results of the XRD measurements of series Y and Z with the results of fig. 8.3. Figure 8.4 shows exemplary XRD patterns for series Y and Z with $x = 10\,\%$.

For series Y, a notable amount of foreign phases consisting of Fe and FeAs can be recognized. For series Z, such impurity phases cannot be seen. Therefore, series Z can be seen as the more preferable way to induce Fe excess in LiFeAs, since it has the same effect on the stoichiometry as series Y, as can be seen by the NQR measurements from the section before, but with lesser amount of impurities.

With the XRD pattern, it was possible to refine the lattice parameters of samples from series Y and Z. In fig. 8.5(a) the resulting unit cell volumes are shown versus the NQR frequency ν_{NQR} as a measure of the Fe excess. The unit cell volume is also showing a linear decrease with increasing amount of Fe excess (represented by the increasing ν_{NQR}), as in fig. 8.3 [10].

Thus, it can be concluded that the shift of the NQR frequency is caused by a shrinking unit cell. A shrinking unit cell alters the surrounding charge environment of the nucleus and thus the EFG. The result is a changed NQR frequency.

The fact that the unit cell volume shows a linear dependency for both, the NQR-frequency and the refined Fe excess y, can be used to estimate the real content of Fe in the off-stoichiometric LiFeAs samples.

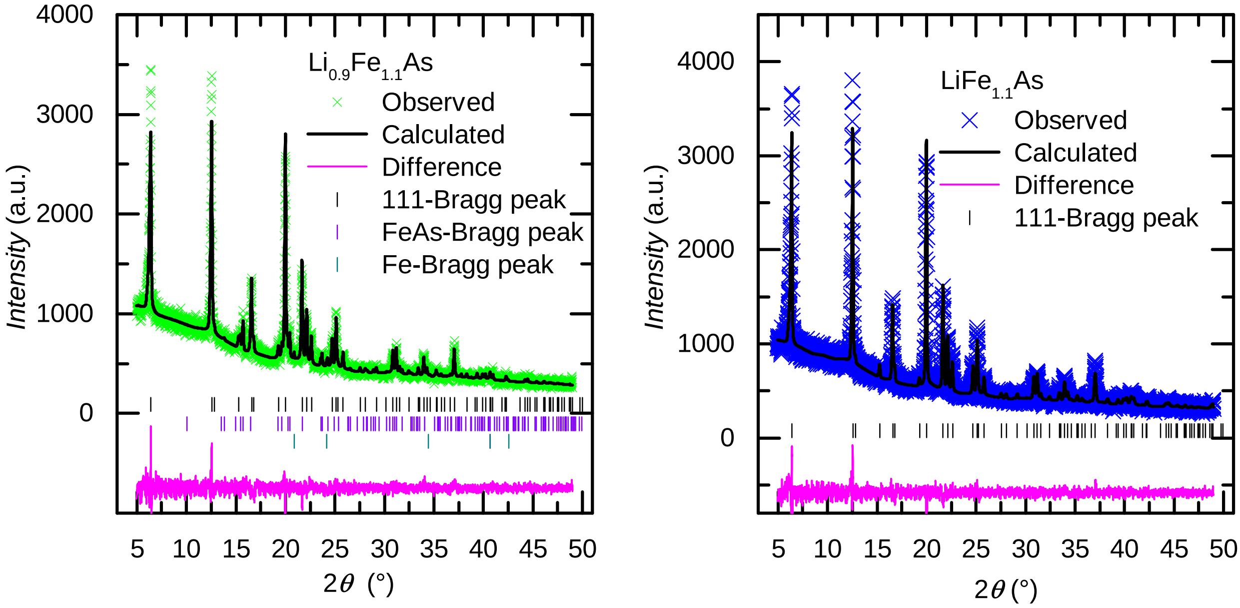

(a) Series Y

(b) Series Z

Figure 8.4: Exemplary X-ray diffraction patterns for series Y and Z with $x = 10\,\%$.

By fitting a linear curve to the data points in fig. 8.5(a), it is possible to obtain a function of the unit cell volume in dependency of the NQR frequency:

$$V(\nu_{\mathrm{NQR}}) = A_n + B_n \cdot \nu_{\mathrm{NQR}}. \tag{8.1}$$

By also performing a linear fit to the data points of fig. 8.3, a function of the unit cell volume in the dependency of the amount y of Fe excess can be derived:

$$V(y) = A + B \cdot y. \tag{8.2}$$

By combining eq. (8.1) and eq. (8.2), it is possible to estimate the amount of Fe from the measured NQR frequency:

$$x_{\mathrm{calc}} = \frac{A_n - A + B_n \cdot \nu_{\mathrm{NQR}}}{B}. \tag{8.3}$$

In fig. 8.5(b), the result of this estimation is visualized for all samples of LiFeAs and off-stoichiometric LiFeAs shown in this work. It is now possible to use the NQR frequency at room temperature to get access to the amount of Fe excess x_{calc}.

It has to be mentioned, that even small changes of the fit parameters A_n and B_n result in dramatic shifts of the linear curve which results in changes of x_{calc} of one order of magnitude.

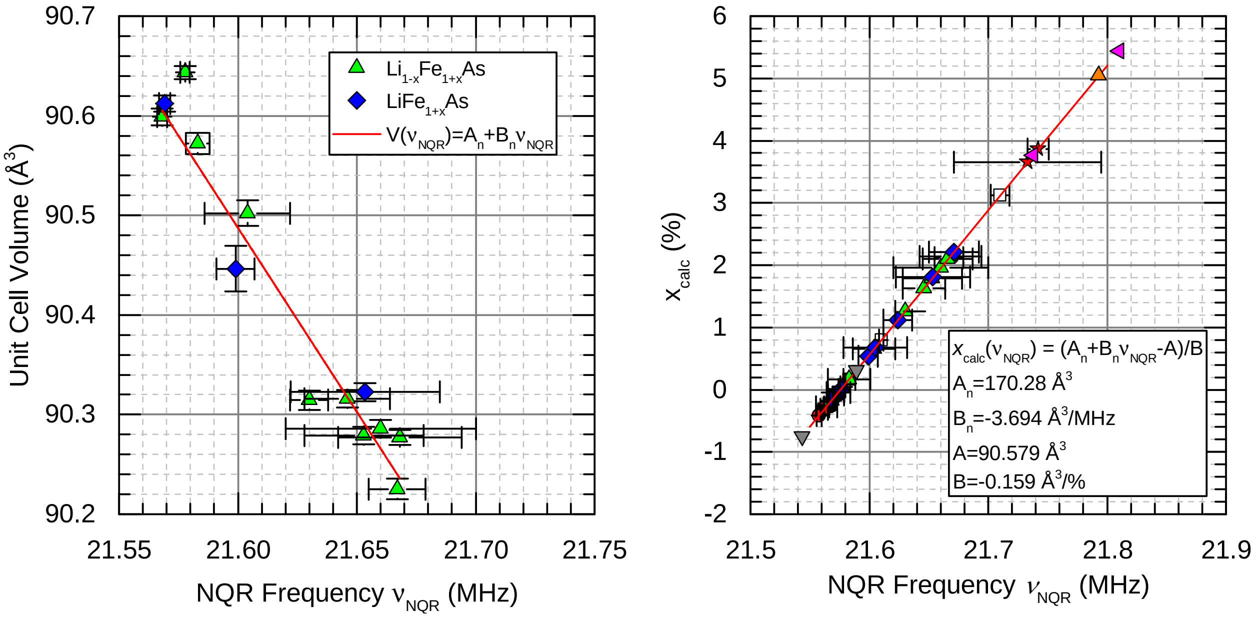

(a) Unit cell volume vs. NQR frequency ν_{NQR} for series Y and Z. The red solid line is a linear fit to the data.

(b) Estimation of the amount of Fe excess x_{calc} from the nuclear quadrupole frequency ν_{NQR}.

Figure 8.5: The combination of the X-ray diffraction measurements and the nuclear quadrupole measurements provide the possibility to calculate the amount of Fe excess x_{calc}.

To minimize the uncertainty of this calculation, very careful measurements of both, the lattice constants and especially the NQR frequency, would be necessary for every kind of LiFeAs sample with Fe excess. If this could be established, it is possible to get a reliable tool to characterize off-stoichiometric LiFeAs samples, by means of NQR.

The figures of the following sections, which show physical properties of series Y and Z in dependency of the amount of Fe excess, will therefore use both, the NQR frequency as a measure of Fe excess and x_{calc} as an estimation to quantify how much Fe is present in the structure.

As can be seen in fig. 8.5(b), the amount of Fe excess for both series Y and series Z saturates at $x_{\mathrm{calc}} \approx 2\,\%$. But the samples were synthesized with a nominal amount of up to $20\,\%$ of Fe excess. So, where are the remaining $18\,\%$?

The XRD-patterns of fig. 8.4 may shed light on this question. A hump-like structure can be seen underneath the Bragg-peaks for low values of the angle 2θ. Such high intensity for low angles, can stand for un-periodic structures in the sample. It might be possible that the remaining Fe, somehow agglomerates in the sample and causes the hump.

The results of the following sections will show, that the electronic properties are still

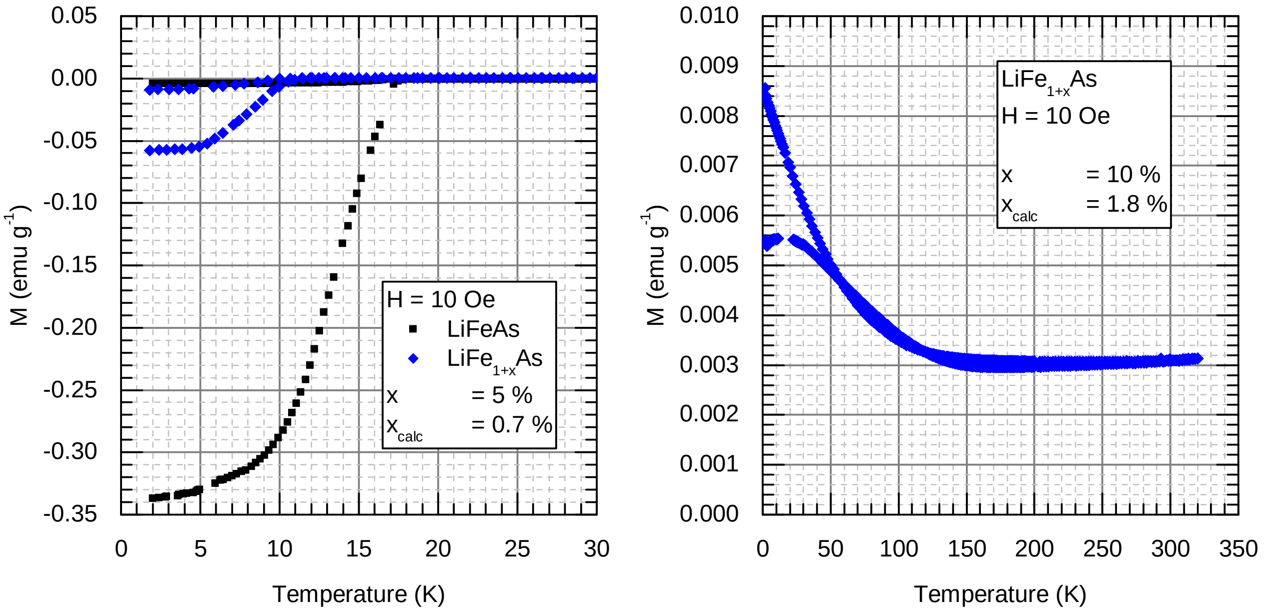

(a) SMS of stoichiometric LiFeAs (black □) and off-stoichiometric LiFe$_{1+x}$As with $x = 5\,\%$ or $x_{\mathrm{calc}} = 0.7\,\%$ respectively (blue ◇), both zero-field and field cooled.

(b) SMS of off-stoichiometric LiFe$_{1+x}$As with $x = 10\,\%$ or $x_{\mathrm{calc}} = 1.8\,\%$ respectively, zero-field and field cooled.

Figure 8.6: Exemplary results of static magnetic susceptibility (SMS) measurements on off-stoichiometric LiFeAs. Measurements done by Shiv J. Singh.

dominated by the altered LiFeAs-phase. At first glance this seems surprising, regarding the high amount of 18 % of agglomerated Fe. If one takes into account that this 18 % of Fe take 6.7 % of the total sample-mass only, the surprise is not that big anymore.

8.4 Static Magnetic Susceptibility

Measurements of the SMS reveal a quite different behavior depending on how much Fe excess in the samples is present. Samples with a Fe content of $x_{\mathrm{calc}} < 1.1\,\%$ show a typical superconducting behavior (see fig. 8.6(a)). Only the superconducting volume fraction is reduced on increasing Fe excess.

But samples with an Fe content of $x_{\mathrm{calc}} \geq 1.1\,\%$ show an increase of the magnetization as it would be typical for magnetic samples (fig. 8.6(b)).

A similar behavior has been seen by Wright et al. [67]. Their samples also show typical superconducting behavior on low amounts of Fe excess and magnetic behavior on higher amounts. Even the overall shape of the magnetization curves from [67] are comparable, at least at first glance (compare with fig. 4.10(a)).

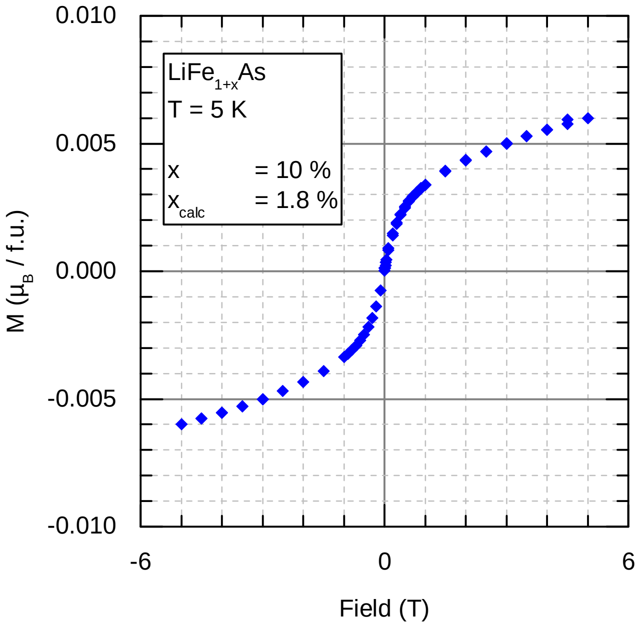

Figure 8.7: Field-dependent static magnetic susceptibility (SMS) on off-stoichiometric $\mathrm{LiFe}_{1+x}\mathrm{As}$ with $x = 10\,\%$ or $x_{\mathrm{calc}} = 1.8\,\%$ respectively. Measurements done by Shiv J. Singh.

On a closer look there are differences. Wright et al. [67] showed a linear behavior of the inverse susceptibility χ^{-1} versus temperature with two different slopes. With a Curie–Weiss fit they could show that the steeper slope stands for fm behavior and the other for antiferromagnetic (afm) behavior (see fig. 4.10(b)). In the case of the shown samples here, this was not possible, as the χ^{-1} did not show linear behavior.

The field-dependency of the magnetization as shown in fig. 8.7 for off-stoichiometric LifeAs with $x_{\mathrm{calc}} = 1.8\,\%$ looks like a typical ferromagnet. It resembles the behavior of fig. 6.1(b), but with a much lower saturation magnetization of $\sim 0.06\,\frac{\mu_{\mathrm{B}}}{\mathrm{f.u.}}$. Also here, the applied fields are not enough to fully saturate the magnetization. The saturated magnetization is also much smaller here than the calculated one of Wright et al. [67] which, for the corresponding amount of Fe, is $1.47\,\frac{\mu_{\mathrm{B}}}{\mathrm{f.u.}}$.

To clarify the discrepancies between the results of Wright et al. [67] and the results presented in this work, further measurements are necessary. At least for the samples shown here, it appears that Fe excess can bring off-stoichiometric LiFeAs close to an fm transition.

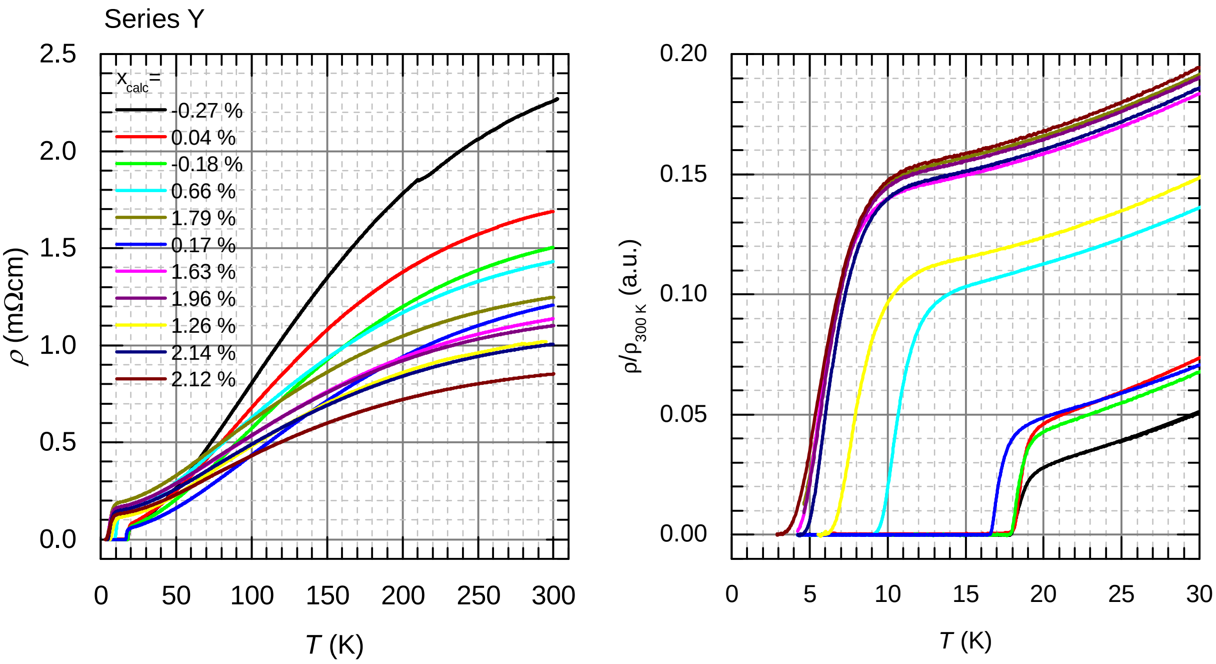

(a) Resistivity versus temperature of series Y for different amounts of Fe excess x_{calc}.

(b) Resistivity of series Y normalized on 300 K in the range from 0 to 30 K. The colors are coded in the same way as in (a).

Figure 8.8: Resistivity measurements on series Y.

8.5 Resistivity

To examine the behavior of the normal-conducting and the superconducting phase on off-stoichiometry, resistivity measurements were performed on series Y and Z. Figures 8.8(a) and 8.9(a) show the temperature behavior of the resistivity for different amounts x_{calc} of Fe excess. The overall behavior of the temperature-dependent resistivity is very well comparable with the typical behavior of LiFeAs (see section 4.6).

Although statements on absolute values for resistivity measurements on polycrystals should be taken with caution, it is eminent, that for both, series Y and series Z, a reduction of the high temperature resistivity with increased Fe excess can be seen. Normally the introduction of additional atoms into the lattice would lead to the formation of new scattering centers, which would increase the resistivity of the samples. Here, the opposite is the case. This behavior is comparable with the reduction of the resistivity seen in fig. 6.12 for fm LiFeAs.

Figures 8.8(b) and 8.9(b) show the the same resistivity data for a low temperature regime, normalized to the resistivity at 300 K. The residual resistivity ρ_0 is increasing with increasing amount x_{calc} of Fe excess (see section 3.4.3) and the superconducting transition temperature

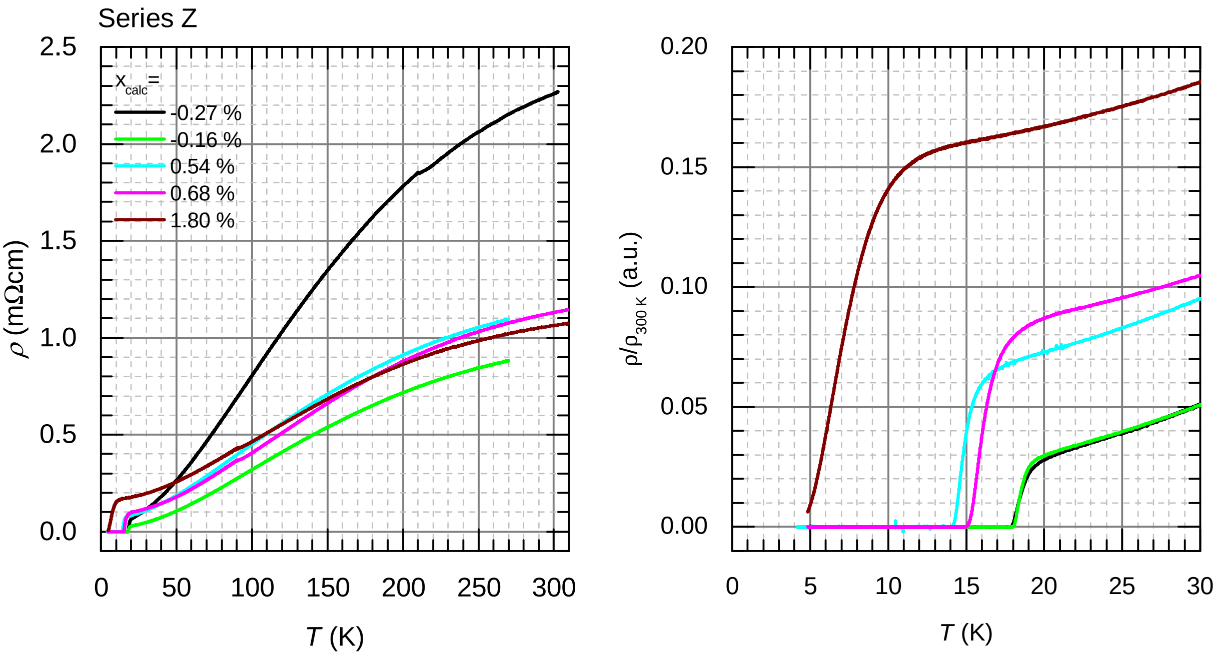

(a) Resistivity versus temperature of series Z for different amounts of Fe excess x_{calc}.

(b) Resistivity of series Z normalized at 300 K in the range from 0 to 30 K. The colors are coded in the same way as in (a).

Figure 8.9: Resistivity measurements on series Z.

T_c is decreasing. The suppression of the superconductivity is no surprise and already known from Pitcher et al. [10]. A surprise is the superconducting behavior of samples with $x_{\mathrm{calc}} \geq 1.1\,\%$. For these samples, SMS was proposing a magnetic behavior (see section 8.4).

To get information of the sample quality, the residual resistivity ratio (RRR) was extracted by

$$RRR = \frac{\rho(300\,\mathrm{K})}{\rho(30\,\mathrm{K})}. \tag{8.4}$$

The results can be seen in fig. 8.10. Here, the inverse RRR is shown versus the NQR frequency as well as the estimated amount x_{calc} of Fe excess, to see that there is a linear relation between the residual resistivity and the Fe content and as such a $\sim \frac{1}{x_{\mathrm{calc}}}$ relation to the RRR. Which is behaving as it should be expected for the small doping range of Fe excess.

To further quantify the resistivity data, the 'parallel-resistor' model of Wiesmann et al. [25], eq. (3.50), was fitted to the curves, as proposed by Bombor [65, 66] (see sections. 3.5

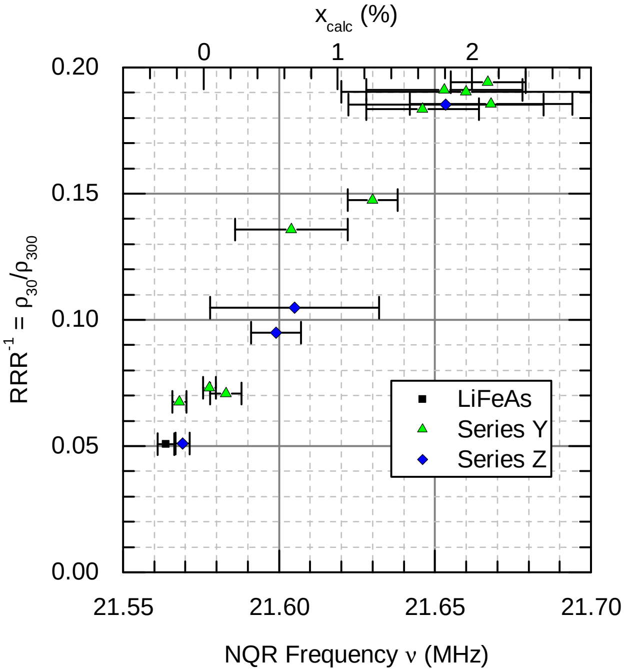

Figure 8.10: Inverse residual resistivity ratio (RRR) calculated by eq. (8.4) versus the nuclear quadrupole resonance frequency ν_{NQR} and the estimated Fe content x_{calc}.

and 4.6). A quadratic temperature behavior was assumed for the ideal resistivity behavior, $\rho_{\mathrm{ideal}} = \rho_0 + A \cdot T^2$, resulting in the fit formula

$$\rho^{-1} = \left(\rho_0 + A \cdot T^2\right)^{-1} + \left(\rho_{\mathrm{lim}}\right)^{-1} . \tag{8.5}$$

The temperature dependency can be described quite well with this fit until superconductivity sets in, as seen in fig. 8.11. The quadratic behavior of this fit can be interpreted as a sign for electron-electron scattering (see section 3.4.4) and the curves mimic the example curve of a sample with dominant electron-electron scattering and limiting resistivity (see fig. 3.9).

The extracted fit parameters are shown in fig. 8.12 versus the NQR frequency and the estimated Fe content x_{calc}. The extracted residual resistivity ρ_0 is shown in fig. 8.12(a). Here, as in fig. 8.10, it can be seen a linear relation between ρ_0 and the Fe content, which is a typical sign for impurity scattering, e.g. from doping with Fe. It confirms the stoichiometric changes seen by the NQR measurements and clearly supports the doping effect of Fe excess on off-stoichiometric LiFeAs.

Figure 8.12(c) shows the surprising result of the reduction of the limiting resistivity with increasing Fe content x_{calc}. As was already stated above, the introduction of additional scattering centers should increase the resistivity. Therefore, another underlying process has to be responsible for this behavior.

A possible explanation for this might be an increased density of states (DOS) at the Fermi level, as already mentioned in section 6.3.2.

Taking a look on fig. 8.12(b) it can be seen that the quadratic coefficient A of the curve

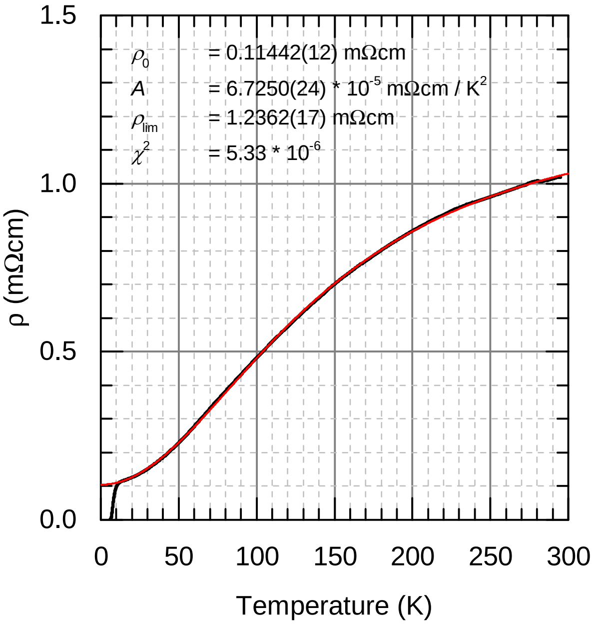

Figure 8.11: Example fit (red solid line) of eq. (3.50) to a sample of series Y (black solid line) with $x = 6\,\%$ or $x_{\mathrm{calc}} = 1.26\,\%$.

is reduced with increasing Fe content. As the quadratic behavior stems from the electron-electron scattering, a decrease of A is a sign of a reduction of this scattering process.

So far, this behavior is not understood. Many effects on the electronic structure can reduce electron-electron-scattering. The reduction of the number of electrons would be one way, but it contradicts with the decrease of the overall resistivity.

8.6 Relevance of the Synthesis Temperature

As it was shown in section 8.2, the shift of the NQR frequency with increasing amount of additional Fe during the synthesis is saturating at $x \approx 10\,\%$ and therefore, the estimated Fe content is also stagnating. It is not possible to further increase the NQR frequency with additional Fe. But the NQR frequencies of the single crystals shown in section 6.3.1 exhibit much higher frequencies and therefore, could have a higher Fe content x_{calc}.

Also two samples of section 7.2, which were synthesized at $T_{\mathrm{synth}} = 800\,°\mathrm{C}$ and $900\,°\mathrm{C}$ show higher NQR frequencies than 21.67 MHz, which is the maximum for series Y and Z.

One crucial difference between the single crystals and the polycrystals, is their synthesis temperature T_{synth}. The single crystals are synthesized usually at a temperature of $\approx 1050\,°\mathrm{C}$. Therefore, the question arises, whether the synthesis temperature might have an effect on the Fe content and thereby on the NQR frequency. To check for such a connection, polycrystals were synthesized with a $T_{\mathrm{synth}} \geq 1000\,°\mathrm{C}$ and a nominal composition of $\mathrm{LiFe_{1.06}As}$.

As can be seen in fig. 8.13(a), the NQR frequency at 300 K is indeed higher than 21.67 MHz.

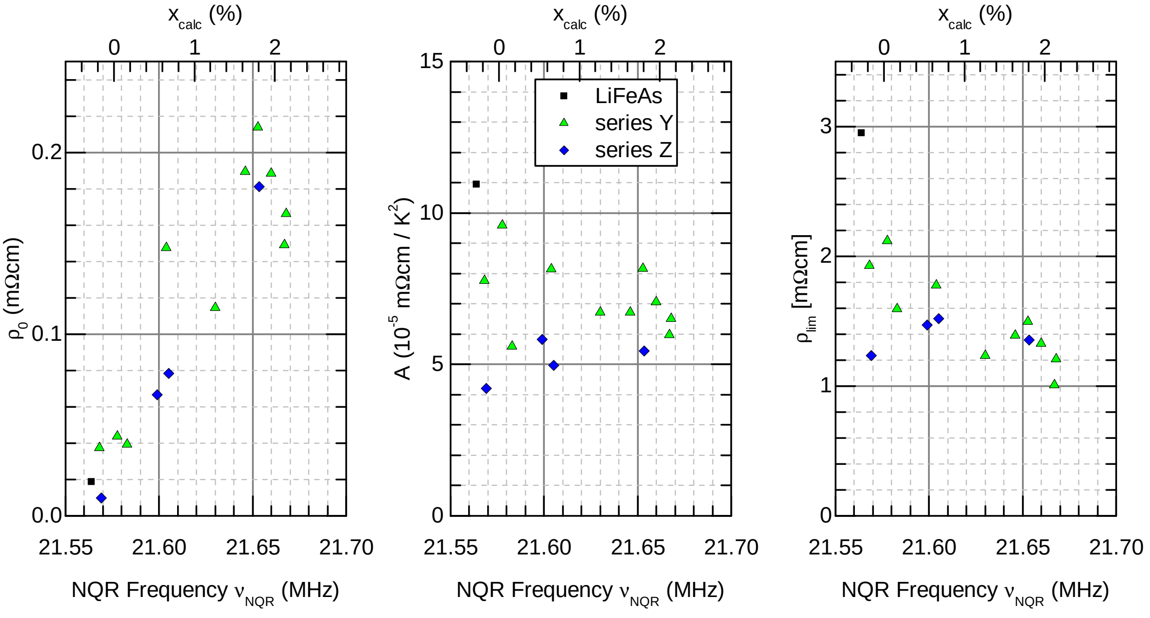

(a) Residual resistivity ρ_0 (b) Quadratic coefficient A (c) Limiting resistivity ρ_{lim}

Figure 8.12: Fit parameters of eq. (3.50) versus the nuclear quadrupole frequency ν_{NQR} and the estimated Fe content x_{calc}.

For $T_{\text{synth}} = 1000\,°\text{C}$ the NQR frequency reaches 21.744 MHz and, therefore, an estimated amount $x_{\text{calc}} = 3.9\,\%$ of Fe excess. A possible explanation was already given in section 7.4. Due to the high synthesis temperature, the Li reactivity is highly increased and it might leave the structure. Since Fe_2As has a structure which is identical with LiFeAs, except the fact that Fe atoms take Li cites [95] it might be that the emerging Li vacancies get filled by Fe atoms.

Comparing the NQR frequencies of these polycrystals synthesized at very high temperatures, with the frequencies of the single crystals, it shows that they lie in the region of fm samples (see fig. 6.13). It would be interesting to see if these samples do also show ferromagnetism.

Already samples with a Fe content of $x_{\text{calc}} \geq 1.1\,\%$ showed magnetic signals in their SMS measurements (see fig. 8.6) but the samples synthesized at $T_{\text{synth}} \geq 800\,°\text{C}$ did not show such a behavior (see fig. 7.5). Therefore, it is not clear if polycrystals synthesized at $T_{\text{synth}} \geq 1000\,°\text{C}$ would also show ferromagnetism. The SMS measurements shown in fig. 8.14 are able to answer this question. Indeed, the very high synthesis temperature is producing a sample with the typical signal of a weak ferromagnet, as proposed by the Stoner model [71] (see section 6.5) with a $T_C \approx 168\,\text{K}$, but the saturation magnetization of about $0.02\,\frac{\mu_B}{\text{f.u.}}$ is much lower as compared to the single crystals.

To further investigate this fm signal, a temperature-dependent measurement of the NQR

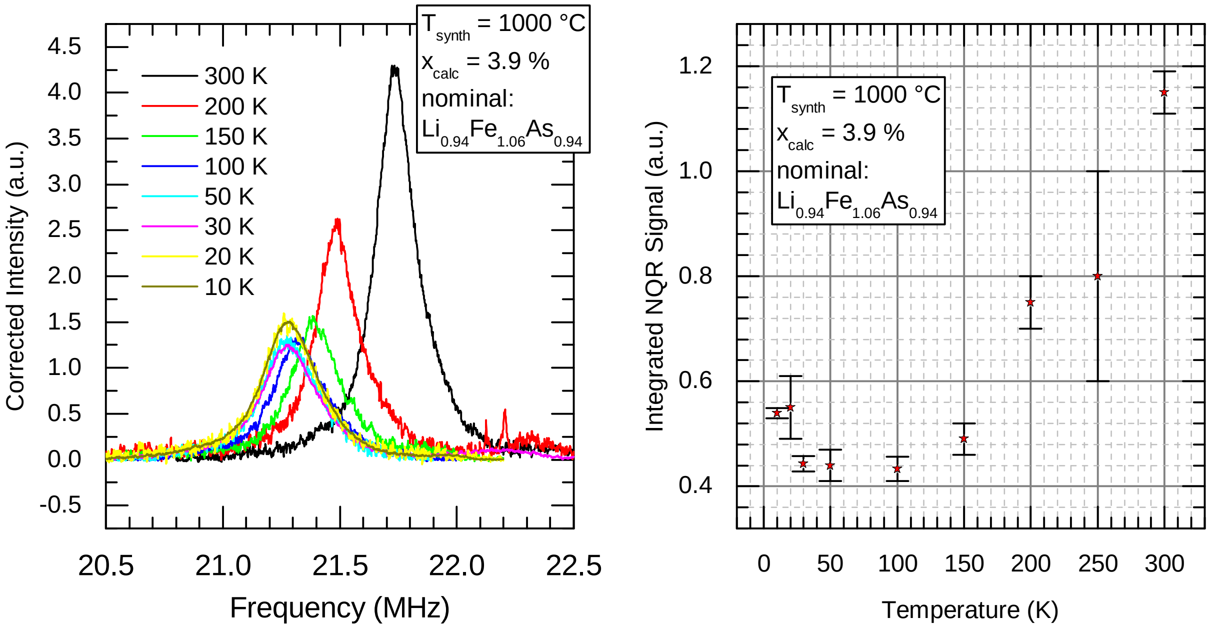

(a) NQR spectra taken at different temperatures

(b) Temperature dependency of the NQR signal intensity

Figure 8.13: Results of nuclear quadrupole resonance (NQR) measurements on a sample synthesized with $T_{\text{synth}} = 1000\,°\text{C}$.

signal intensity was performed. As stated in section 2.6, the occurrence of a strong internal magnetic field would shift the resonance frequency that much, that the irradiated stimulation would be off resonance. As a consequence the NQR resonance signal would lose intensity.

This can be seen in fig. 8.13(b). The signal intensity is dropping with decreasing temperature, but it is not vanishing completely. 40 to 60 % of the intensity remain. So, only 60 to 40 % of the ^{75}As nuclei see the magnetism. Therefore, not the whole sample becomes magnetic.

Such a result would suggests a phase separation in the sample. But if there is a phase separation, it is not influencing the electrical charge environment of the ^{75}As. There is no line splitting visible, which would support it. It seems as there would be two identical structures, but one is seeing the magnetism the other is not.

Other interesting results come from resistivity measurements on these samples synthesized at very high T_{synth} (see fig. 8.15).

The overall temperature-dependency is again very typical for a LiFeAs sample. It does not show any sign of an anomaly at the magnetic transition temperature, but this also holds true for the fm single crystals (see fig. 6.12). The value of the room temperature resistivity is very similar compared to the samples of series Z and, therefore, it also is reduced compared

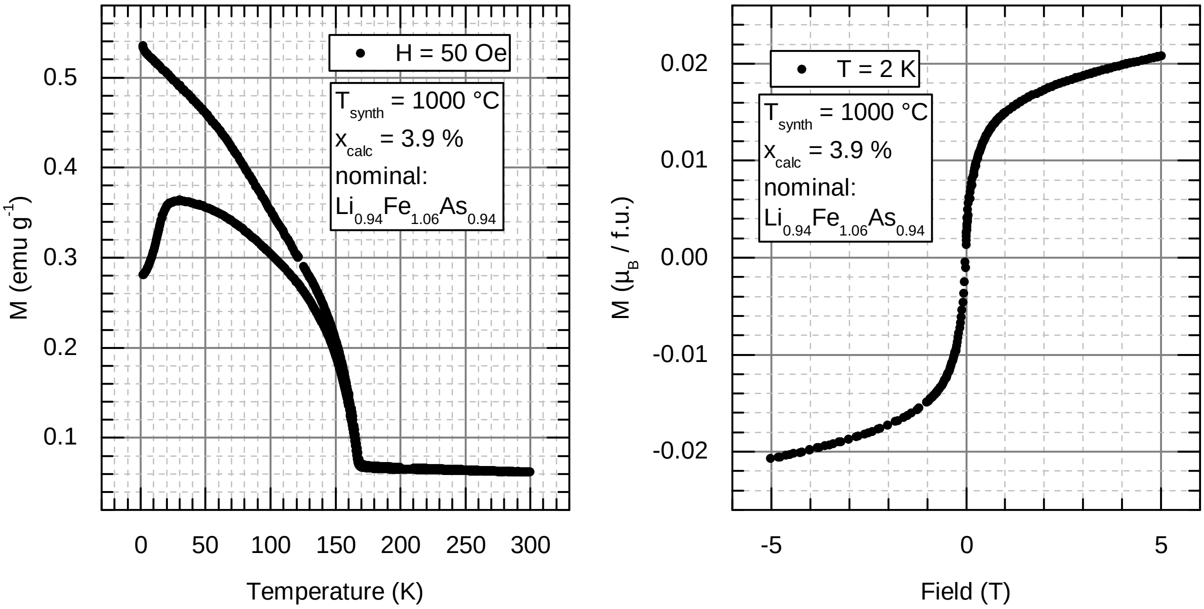

(a) Magnetization versus temperature at a magnetic field of 50 Oe.

(b) Magnetization versus magnetic field at a temperature of 2 K.

Figure 8.14: Magnetization of a sample synthesized with $T_{\text{synth}} = 1000\,°\text{C}$. Measurements done by Shiv J. Singh.

to the stoichiometric sample. The 'parallel-resistor' model (see section 3.5) is also working here, and gives values for the fit parameters which are also comparable to the ones of series Z.

All the values fit quite well to samples which show Fe excess.

The real surprise comes from the low-temperature regime of the measurement. Although the sample shows signs of weak ferromagnetism, it clearly has all properties of a typical superconductor with a T_c of 9 K.

Of course, now the question arises, if the superconductivity is coexistent with the ferromagnetism, but the results are inconclusive so far.

It might be possible that these superconductivity is originated in the remaining phase (see fig.8.13(b)) which did not get fm. The NQR intensity might not fall down to zero as expected, but there are also no signs of a secondary phase visible which would manifest in a second NQR peak or at least in a strong asymmetry of the peak shape. Even the single crystals show a drop of the resistivity, although it does not completely vanish (see fig. 6.12). The overall behavior is quite similar to the samples synthesized at very high T_{synth}.

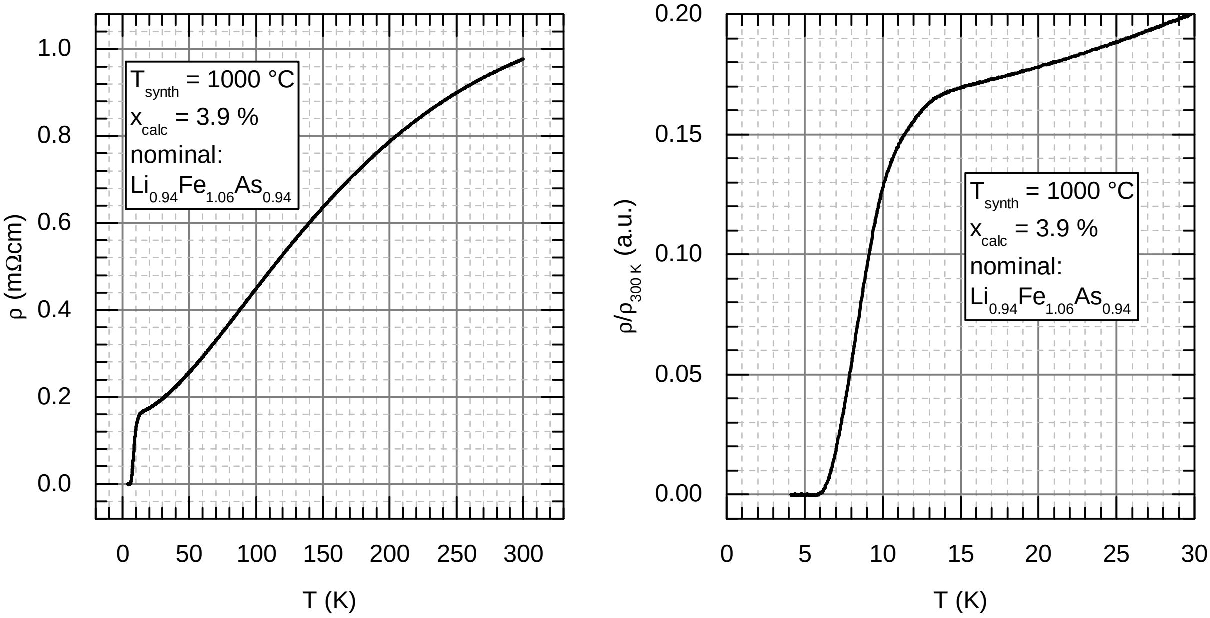

(a) Temperature dependency of the resistivity.

(b) Temperature dependency of the resistivity normalized on 300 K in a low temperature range.

Figure 8.15: Results of resistivity measurements on a sample synthesized with a synthesis temperature $T_{\mathrm{synth}} = 1000\,°\mathrm{C}$.

8.7 Summary

With measurements of the NQR frequency and of the lattice parameters it is possible to scale the NQR frequency to the measured Fe excess of Wright et al. [67] (see fig. 8.5(b)). Therefore, it is possible to estimate the real Fe excess x_{calc} of the off-stoichiometric samples.

By increasing x_{calc} up to 3.2 % ($\nu_{\mathrm{NQR}} = 21.70\,\mathrm{MHz}$), the superconducting transition temperature T_c is suppressed from $\approx 18\,\mathrm{K}$ to $\approx 9\,\mathrm{K}$.

Fe excess is reducing the unit cell volume of the crystal structure (see section 8.3). This could cause a change in the electrical structure, which could increase the DOS at the Fermi level, and thereby decrease the resistivity (see fig. 8.12). As pressure would also cause a shrinking of the unit cell, this is supported by the pressure dependent resistivity measurements of Zhang et al. [55] (discussed in section 4.6) which show a reduction of resistivit with increasing pressure.

As the Stoner criterion suggests (see section 6.5) a high DOS at the Fermi level could cause a fm transition. So the same effect that is reducing the resistivity might also induce the fm transition.

By the NQR frequency, it is possible to supplement the phase diagram shown in fig. 6.13.

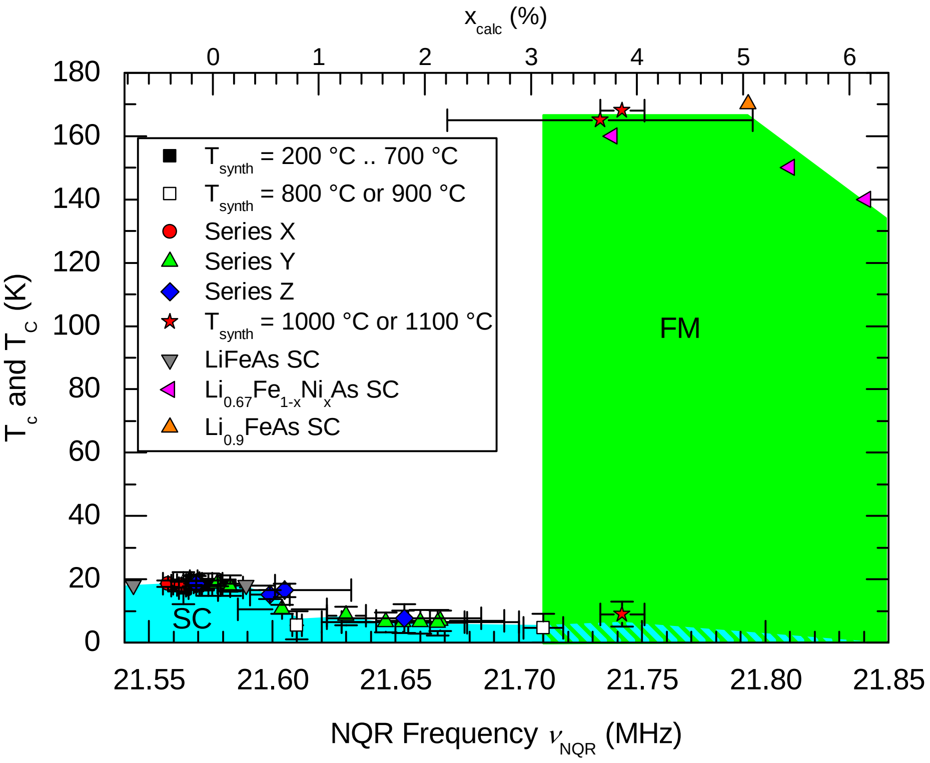

Figure 8.16: Superconducting and Ferromagnetic Phase Diagram of off-stoichiometric LiFeAs with Fe excess built by nuclear quadrupole resonance. All frequencies were taken at room temperature. The data for the single crystals (SC) are the same as in fig. 6.13.

The result can be seen in fig. 8.16. As stated in chapter 6, LiFeAs is indeed close to a fm phase transition and by Fe excess it can be driven into the fm phase. The critical doping level to develop this phase lies in between a Fe content x_{calc} of 3.2 % and 3.6 %.

9 Conclusion and Outlook

The purpose of this work was the investigation of the superconducting and ferromagnetic (fm) phase diagram of off-stoichiometric LiFeAs.

The starting point were a summary of results of a combined study of scientist of the Leibniz Institute for Solid State and Materials Research Dresden (IFW Dresden), the technical university Dresden and the university of Cologne (see chapter 6). The results were combined and used to get a comprehensive view on the nature of ferromagnetism in LiFeAs.

The combination of several methods revealed, that LiFeAs is close to a fm transition as proposed by Brydon et al. [12]. The emerging ferromagnetism is weak and of itinerant nature. By taking the Stoner model [71], the origin of the magnetic transition was put down to an increased density of states (DOS) at the Fermi level.

Distinct properties of the fm samples in nuclear quadrupole resonance (NQR) measurements can be used to characterize the samples, leading to a phase diagram showing a superconducting and an fm region (see fig 6.13).

To fill the gap between the superconducting and the fm samples, optimized samples were needed as a starting point. Chapter 7 showed how to use NQR to optimize the synthesis process of polycrytaline LiFeAs to get high quality samples with maximum T_c. Polycrystals were chosen, because it is easier to alter their stoichiometry than for single crystals. The optimal samples show a very small NQR line width, comparable to single crystals. The Superconducting properties of these samples can compete with single crystals, and the purity measured by the residual resistivity ratio (RRR) is also in the range of single crystals.

With the optimized synthesis process, various samples with different nominal compositions of off-stoichiometries were synthesized. The measurement of the NQR frequency revealed that Fe excess is responsible for stoichiometric changes in the structure (fig. 8.2). It causes a reduction of the unit cell volume as measured by X-ray diffraction (XRD) (fig. 8.5(a)).

The reduction of the unit cell volume is linear with increasing amount of Fe excess and NQR frequency [10]. Thus, it can be used to estimate the real amount of Fe excess in the samples (fig. 8.5(b)).

The high temperature resistivity is significantly reduced by Fe excess (fig. 8.12), which can be explained by an increase of the DOS at the Fermi level. The increased DOS can drive the system to an fm transition at an amount x_{calc} of Fe excess between 3.2 and 3.6 % resulting in the supplemented phase Diagram of LiFeAs (fig. 8.16). As pressure is also shrinking the unit cell, the decreasing resistivity-data by increasing pressure of Zhang et al. [55] further supports this reasoning.

Several questions remain unanswered by this work.

If the fm transition is caused by the shrinking unit cell, then Fe excess might cause a kind of chemical pressure in LiFeAs. To verify the effect of the shrinking unit cell, pressure dependent NQR measurements could be very helpful. The NQR frequency would reveal immediately when the pressure induces structural changes. If the sample would undergo a magnetic transition, it could also be seen by the vanishing NQR intensity.

It is not clear which lattice site the Fe in the structure is occupying. It might occupy interstitial positions or Li positions. As the isostructural Fe_2As is showing a smaller unit cell compared to LiFeAs [95], which is having Fe as intercalations between the FeAs-tetraeders, it is possible that the additional Fe is occupying Li positions.

To prove that the DOS of states is really increased with the shrinking unit cell volume, measurements of the electronic structure of Fe excess LiFeAs are necessary, e.g. by angle-resolved photoemission spectroscopy (ARPES). Also pressure dependent measurement would be useful. Therefore, high quality single crystals would be needed and thus an optimization process of preparing such single crystals. To get the wanted properties, NQR can be used as a tool to characterize the samples.

Moreover, it is still not clear if the fm transition is related to the superconductivity. If that is the case, there should be an enhanced interaction at an scattering vector of $\mathbf{q} = 0$. Such measurements could be done by quasi particle interference, which is also in need of single crystals. Static susceptibility measured at $\mathbf{q} = 0$, namely nuclear magnetic resonance (NMR) Knight, shift can give insides here, too.

In the end, LiFeAs and especially fm LiFeAs caused by Fe excess stays an interesting topic for future studies.

Bibliography

[1] H. K. Onnes. "Further experiments with liquid Helium. C. On the change of electric resitance of pure metals at very low temperatures etc. IV. The resistance of pure mercury at helium temperatures." In: *Proceedings of the Koninklijke Akademie van Wetenschappen Te Amsterdam* (Apr. 1911), p. 1479 (cit. on p. 1).

[2] J. Bardeen, L. N. Cooper, and J. R. Schrieffer. "Theory of Superconductivity". In: *Phys. Rev.* 108 (5 Dec. 1957), p. 1175.
doi:10.1103/PhysRev.108.1175 (cit. on p. 1).

[3] J. G. Bednorz and K. A. Müller. "Possible highT_c superconductivity in the Ba-La-Cu-O system". In: *Zeitschrift für Physik B Condensed Matter* 64.2 (1986), p. 189. ISSN: 1431-584X.
doi:10.1007/BF01303701 (cit. on p. 1).

[4] Y. Kamihara, T. Watanabe, M. Hirano, and H. Hosono. "Iron-Based Layered Superconductor La[$O_{1-x}F_x$]FeAs (x = 0.05-0.12) with T_c = 26 K". In: *J. Am. Chem. Soc.* 130.11 (2008). PMID: 18293989, pp. 3296–3297.
doi:10.1021/ja800073m (cit. on pp. 1, 33, 34).

[5] G. Wu, Y. L. Xie, H. Chen, M. Zhong, R. H. Liu, B. C. Shi, Q. J. Li, X. F. Wang, T. Wu, Y. J. Yan, J. J. Ying, and X. H. Chen. "Superconductivity at 56 K in samarium-doped SrFeAsF". In: *Journal of Physics: Condensed Matter* 21.14 (2009), p. 142203.
`http://stacks.iop.org/0953-8984/21/i=14/a=142203` (cit. on p. 1).

[6] R. Juza and K. Langer. "Ternäre Phosphide und Arsenide des Lithiums mit Eisen, Kobalt oder Chrom im Cu_2Sb-Typ". In: *Zeitschrift für anorganische und allgemeine Chemie* 361.1-2 (1968), pp. 58–73. ISSN: 1521-3749.
doi:10.1002/zaac.19683610107 (cit. on pp. 2, 34).

[7] M. J. Pitcher, D. R. Parker, P. Adamson, S. J. C. Herkelrath, A. T. Boothroyd, R. M. Ibberson, M. Brunelli, and S. J. Clarke. "Structure and superconductivity of LiFeAs". In: *Chem. Commun.* 45 (2008), p. 5918. ISSN: 1364-548X.
doi:10.1039/b813153h (cit. on pp. 2, 33, 42, 73).

[8] J. H. Tapp, Z. Tang, B. Lv, K. Sasmal, B. Lorenz, P. C. W. Chu, and A. M. Guloy. “LiFeAs: An intrinsic FeAs-based superconductor with $T_c = 18$ K”. In: *Phys. Rev. B* 78 (Aug. 2008), p. 060505. ISSN: 1550-235X.
doi:10.1103/physrevb.78.060505 (cit. on pp. 2, 33, 42, 73, 80).

[9] X. Wang, Q. Liu, Y. Lv, W. Gao, L. Yang, R. Yu, F. Li, and C. Jin. “The superconductivity at 18 K in LiFeAs system”. In: *Solid State Commun.* 148 (2008), p. 538. ISSN: 0038-1098.
doi:10.1016/j.ssc.2008.09.057 (cit. on pp. 2, 33, 42, 73, 80).

[10] M. J. Pitcher, T. Lancaster, J. D. Wright, I. Franke, A. J. Steele, P. J. Baker, F. L. Pratt, W. T. Thomas, D. R. Parker, S. J. Blundell, and et al. “Compositional Control of the Superconducting Properties of LiFeAs”. In: *J. Am. Chem. Soc.* 132.30 (Aug. 2010), p. 10467. ISSN: 1520-5126.
doi:10.1021/ja103196c (cit. on pp. 2, 33, 39, 73, 81, 85, 89, 90, 96, 105).

[11] S. Aswartham, G. Behr, L. Harnagea, D. Bombor, A. Bachmann, I. V. Morozov, V. B. Zabolotnyy, A. A. Kordyuk, T. K. Kim, D. V. Evtushinsky, S. V. Borisenko, A. U. B. Wolter, C. Hess, S. Wurmehl, and B. Büchner. “Suppressed superconductivity in charge-doped Li($\mathrm{Fe}_{1-x}\mathrm{Co}_x$)As single crystals”. In: *Phys. Rev. B* 84 (5 Aug. 2011), p. 054534.
doi:10.1103/PhysRevB.84.054534 (cit. on pp. 2, 33, 39, 55, 66, 68).

[12] P. M. R. Brydon, M. Daghofer, C. Timm, and J. van den Brink. “Theory of magnetism and triplet superconductivity in LiFeAs”. In: *Phys. Rev. B* 83 (6 Feb. 2011), p. 060501.
doi:10.1103/PhysRevB.83.060501 (cit. on pp. 2, 38, 41, 44, 55, 71, 105).

[13] H.-G. Dehmelt and H. Krüger. “Kernquadrupolfrequenzen in festem Dichloräthylen”. In: *Naturwissenschaften* 37 (1950), p. 111.
doi:10.1007/BF00623717 (cit. on p. 5).

[14] M. Bloom, E. L. Hahn, and B. Herzog. “Free Magnetic Induction in Nuclear Quadrupole Resonance”. In: *Phys. Rev.* 97 (6 Mar. 1955), pp. 1699–1709.
doi:10.1103/PhysRev.97.1699 (cit. on pp. 5, 10, 11).

[15] C. P. Slichter. *Principles of Magnetic Resonance.* Springer, 1989 (cit. on p. 5).

[16] T. P. Das and E. L. Hahn. *Nuclear Quadrupole Resonance Spectroscopy.* Ed. by F. Seitz and D. Turnbull. Academic Press, NY, 1958. ISBN: 0126077614.
`http://hdl.handle.net/2027/mdp.39015001335077` (cit. on p. 5).

[17] B. H. Suits, S. A. Dikanov, A. R. Crofts, J. M. Cadogan, D. R. Vij, N. Jaggi, N. T. Flynn, and H.-L. Lee. *Handbook of Applied Solid State Spectroscopy.* Ed. by E. R. Vij. Springer US, 2006. ISBN: 978-0-387-32497-5.
doi:10.1007/0-387-37590-2 (cit. on pp. 5, 8).

[18] E. L. Hahn. “Spin Echoes”. In: *Phys. Rev.* 80 (1950), p. 580. doi:10.1103/PhysRev.80.580 (cit. on p. 11).

[19] A. Marx and R. Gross. *Festkörperphysik*. Oldenbourg Wissensch.Vlg, 2012. ISBN: 9783486712940 (cit. on pp. 15–17, 19, 20, 22, 24, 29, 30).

[20] P. Drude. “Zur Elektronentheorie der Metalle”. In: *Ann.Phys.* 306.3 (1900), pp. 566–613. ISSN: 1521-3889. doi:10.1002/andp.19003060312 (cit. on p. 15).

[21] F. Bloch. “Über die Quantenmechanik der Elektronen in Kristallgittern”. In: *Zeitschrift für Physik* 52.7-8 (July 1929), pp. 555–600. doi:10.1007/bf01339455 (cit. on p. 18).

[22] A. Matthiessen and C. Vogt. “On the Influence of Temperature on the Electric Conducting-Power of Alloys”. In: *Philosophical Transactions of the Royal Society of London* 154.0 (Jan. 1864), p. 167. ISSN: 0261-0523. doi:10.1098/rstl.1864.0004 (cit. on p. 28).

[23] M. Gurvitch. “Ioffe-Regel criterion and resistivity of metals”. In: *Phys. Rev. B* 24 (12 Dec. 1981), pp. 7404–7407. doi:10.1103/PhysRevB.24.7404 (cit. on pp. 31, 32).

[24] A. F. Ioffe and A. R. Regel. “Progress in semiconductors”. In: *Vol. 4Wiley, New York* (1960), p. 239 (cit. on p. 31).

[25] H. Wiesmann, M. Gurvitch, H. Lutz, A. Ghosh, B. Schwarz, M. Strongin, P. B. Allen, and J. W. Halley. “Simple Model for Characterizing the Electrical Resistivity in $A-15$ Superconductors”. In: *Phys. Rev. Lett.* 38 (14 Apr. 1977), pp. 782–785. doi:10.1103/PhysRevLett.38.782 (cit. on pp. 32, 43, 96).

[26] G. R. Stewart. “Superconductivity in iron compounds”. In: *Rev.Mod.Phys.* 83 (2011), p. 1589. doi:10.1103/RevModPhys.83.1589 (cit. on p. 33).

[27] M. Rotter, M. Tegel, and D. Johrendt. “Superconductivity at 38 K in the Iron Arsenide $Ba_{1-x}K_xFe_2As_2$”. In: *Phys. Rev. Lett.* 101 (2008), p. 107006. doi:10.1103/PhysRevLett.101.107006 (cit. on pp. 34, 39).

[28] G. Haegg and A. L. Kindstroem. “Röntgenuntersuchungen am System Eisen-Selen”. In: *Zeitschrift für Physikalische Chemie, Abteilung B* 22 (1933), p. 453 (cit. on p. 34).

[29] K. Ishida, Y. Nakai, and H. Hosono. “To What Extent Iron-Pnictide New Superconductors Have Been Clarified: A Progress Report”. In: *J. Phys. Soc. Jpn.* 78.6 (2009), p. 062001. doi:10.1143/JPSJ.78.062001 (cit. on p. 33).

[30] S. Raghu, X.-L. Qi, C.-X. Liu, D. J. Scalapino, and S.-C. Zhang. “Minimal two-band model of the superconducting iron oxypnictides”. In: *Phys. Rev. B* 77 (2008), p. 220503. doi:10.1103/PhysRevB.77.220503 (cit. on p. 34).

[31] P. J. Hirschfeld, M. M. Korshunov, and I. I. Mazin. “Gap symmetry and structure of Fe-based superconductors”. In: *Rep. Prog. Phys.* 74.12 (2011), p. 124508. `http://stacks.iop.org/0034-4885/74/i=12/a=124508` (cit. on pp. 34, 35, 38).

[32] J. Fink, S. Thirupathaiah, R. Ovsyannikov, H. A. Dürr, R. Follath, Y. Huang, S. de Jong, M. S. Golden, Y.-Z. Zhang, H. O. Jeschke, R. Valentí, C. Felser, S. Dastjani Farahani, M. Rotter, and D. Johrendt. “Electronic structure studies of $BaFe_2As_2$ by angle-resolved photoemission spectroscopy”. In: *Phys. Rev. B* 79 (15 Apr. 2009), p. 155118.
doi:10.1103/PhysRevB.79.155118 (cit. on p. 34).

[33] T. Kondo, R. M. Fernandes, R. Khasanov, C. Liu, A. D. Palczewski, N. Ni, M. Shi, A. Bostwick, E. Rotenberg, J. Schmalian, S. L. Bud’ko, P. C. Canfield, and A. Kaminski. “Unexpected Fermi-surface nesting in the pnictide parent compounds $BaFe_2As_2$ and $CaFe_2As_2$ revealed by angle-resolved photoemission spectroscopy”. In: *Phys. Rev. B* 81 (6 Feb. 2010), p. 060507.
doi:10.1103/PhysRevB.81.060507 (cit. on p. 34).

[34] S. V. Borisenko, V. B. Zabolotnyy, D. V. Evtushinsky, T. K. Kim, I. V. Morozov, A. N. Yaresko, A. A. Kordyuk, G. Behr, A. Vasiliev, R. Follath, and B. Büchner. “Superconductivity without Nesting in LiFeAs”. In: *Phys. Rev. Lett.* 105.6 (6 Aug. 2010), p. 067002. ISSN: 1079-7114.
doi:10.1103/PhysRevLett.105.067002 (cit. on pp. 34, 35, 37, 43, 44).

[35] A. A. Kordyuk. “Iron-based superconductors: Magnetism, superconductivity, and electronic structure (Review Article)”. In: *Low Temp. Phys.* 38.9 (2012), pp. 888–899. doi:10.1063/1.4752092 (cit. on pp. 35, 37).

[36] J. Dong, H. J. Zhang, G. Xu, Z. Li, G. Li, W. Z. Hu, D. Wu, G. F. Chen, X. Dai, J. L. Luo, Z. Fang, and N. L. Wang. “Competing orders and spin-density-wave instability in $La(O_{1-x}F_x)FeAs$”. In: *EPL (Europhysics Letters)* 83.2 (2008), p. 27006. `http://stacks.iop.org/0295-5075/83/i=2/a=27006` (cit. on p. 35).

[37] Y. Wang, A. Kreisel, V. B. Zabolotnyy, S. V. Borisenko, B. Büchner, T. A. Maier, P. J. Hirschfeld, and D. J. Scalapino. “Superconducting gap in LiFeAs from three-dimensional spin-fluctuation pairing calculations”. In: *Phys. Rev. B* 88 (17 Nov. 2013), p. 174516.
doi:10.1103/PhysRevB.88.174516 (cit. on pp. 36–38, 71).

[38] S. V. Borisenko, V. B. Zabolotnyy, A. A. Kordyuk, D. V. Evtushinsky, T. K. Kim, I. V. Morozov, R. Follath, and B. Büchner. "One-Sign Order Parameter in Iron Based Superconductor". In: *Symmetry* 4.1 (Mar. 2012), pp. 251–264. ISSN: 2073-8994. doi:10.3390/sym4010251 (cit. on p. 36).

[39] O. Heyer, T. Lorenz, V. B. Zabolotnyy, D. V. Evtushinsky, S. V. Borisenko, I. Morozov, L. Harnagea, S. Wurmehl, C. Hess, and B. Büchner. "Resistivity and Hall effect of LiFeAs: Evidence for electron-electron scattering". In: *Phys. Rev. B* 84 (6 Aug. 2011), p. 064512.
doi:10.1103/PhysRevB.84.064512 (cit. on pp. 37, 42, 66, 80, 83).

[40] A. E. Taylor, M. J. Pitcher, R. A. Ewings, T. G. Perring, S. J. Clarke, and A. T. Boothroyd. "Antiferromagnetic spin fluctuations in LiFeAs observed by neutron scattering". In: *Phys. Rev. B* 83 (22 June 2011), p. 220514.
doi:10.1103/PhysRevB.83.220514 (cit. on p. 37).

[41] M. Wang, X. C. Wang, D. L. Abernathy, L. W. Harriger, H. Q. Luo, Y. Zhao, J. W. Lynn, Q. Q. Liu, C. Q. Jin, C. Fang, and et al. "Antiferromagnetic spin excitations in single crystals of nonsuperconducting Li_{1-x}FeAs". In: *Phys. Rev. B* 83.22 (June 2011). ISSN: 1550-235X.
doi:10.1103/physrevb.83.220515 (cit. on p. 37).

[42] N. Qureshi, P. Steffens, Y. Drees, A. C. Komarek, D. Lamago, Y. Sidis, L. Harnagea, H.-J. Grafe, S. Wurmehl, B. Büchner, and M. Braden. "Inelastic Neutron-Scattering Measurements of Incommensurate Magnetic Excitations on Superconducting LiFeAs Single Crystals". In: *Phys. Rev. Lett.* 108 (11 Mar. 2012), p. 117001.
doi:10.1103/PhysRevLett.108.117001 (cit. on p. 37).

[43] S.-H. Baek, H.-J. Grafe, F. Hammerath, M. Fuchs, C. Rudisch, L. Harnagea, S. Aswartham, S. Wurmehl, J. van den Brink, and B. Büchner. "^{75}As NMR-NQR study in superconducting LiFeAs". In: *Eur. Phys. J. B* 85.5 (May 2012). ISSN: 1434-6036.
doi:10.1140/epjb/e2012-30164-5 (cit. on pp. 38, 40, 41, 44, 62, 68, 71–73, 76, 81, 83, 85).

[44] C. de la Cruz, Q. Huang, J. W. Lynn, J. Li, W. R. II, J. L. Zarestky, H. A. Mook, G. F. Chen, J. L. Luo, N. L. Wang, and P. Dai. "Magnetic order close to superconductivity in the iron-based layered $\mathrm{LaO}_{1-x}\mathrm{F}_x$FeAs systems". In: *Nature* 453 (2008), p. 899.
doi:10.1038/nature07057 (cit. on p. 39).

[45] T. Nomura, S. W. Kim, Y. Kamihara, M. Hirano, P. V. Sushko, K. Kato, M. Takata, A. L. Shluger, and H. Hosono. "Crystallographic phase transition and high- T_c superconductivity in LaFeAsO:F". In: *Supercond. Sci. Technol.* 21.12 (2008), p. 125028.
`http://stacks.iop.org/0953-2048/21/i=12/a=125028` (cit. on p. 39).

[46] D. N. Basov and A. V. Chubukov. “Manifesto for a higher Tc”. In: *Nat. Phys.* 7.4 (Apr. 2011), pp. 272–276. ISSN: 1745-2481.
doi:10.1038/nphys1975 (cit. on p. 39).

[47] N. Ni, A. Thaler, J. Q. Yan, A. Kracher, E. Colombier, S. L. Bud’ko, P. C. Canfield, and S. T. Hannahs. “Temperature versus doping phase diagrams for $\mathrm{Ba(Fe_{1-x}TM_x)_2As_2}$ (TM=Ni,Cu/Co) single crystals”. In: *Phys. Rev. B* 82 (2 July 2010), p. 024519.
doi:10.1103/PhysRevB.82.024519 (cit. on p. 39).

[48] H. Luetkens, H.-H. Klauss, M. Kraken, F. J. Litterst, T. Dellmann, R. Klingeler, C. Hess, R. Khasanov, A. Amato, C. Baines, M. Kosmala, O. J. Schumann5, M. Braden, J. Hamann-Borrero, N. Leps, A. Kondrat, G. Behr, J.Werner, and B. Büchner. “The electronic phase diagram of the $\mathrm{LaO_{1-x}F_xFeAs}$ superconductor”. In: *Nature Mater.* 8 (2009), pp. 305–309.
doi:10.1038/NMAT2397 (cit. on p. 39).

[49] P. Jeglič, A. Potočnik, M. Klanjšek, M. Bobnar, M. Jagodič, K. Koch, H. Rosner, S. Margadonna, B. Lv, A. M. Guloy, and D. Arčon. “^{75}As nuclear magnetic resonance study of antiferromagnetic fluctuations in the normal state of LiFeAs”. In: *Phys. Rev. B* 81.14 (Apr. 2010).
doi:10.1103/physrevb.81.140511 (cit. on pp. 40, 41).

[50] J. Korringa. “Nuclear magnetic relaxation and resonnance line shift in metals”. In: *Physica* 16.7 (1950), pp. 601–610. ISSN: 0031-8914.
doi:http://dx.doi.org/10.1016/0031-8914(50)90105-4 (cit. on p. 40).

[51] Z. Li, Y. Ooe, X.-C. Wang, Q.-Q. Liu, C.-Q. Jin, M. Ichioka, and G.-q. Zheng. “^{75}As NQR and NMR Studies of Superconductivity and Electron Correlations in Iron Arsenide LiFeAs”. In: *J. Phys. Soc. Jpn.* 79.8 (Aug. 2010), p. 083702. ISSN: 1347-4073.
doi:10.1143/jpsj.79.083702 (cit. on p. 41).

[52] I. Morozov, A. Boltalin, O. Volkova, A. Vasiliev, O. Kataeva, U. Stockert, M. Abdel-Hafiez, D. Bombor, A. Bachmann, L. Harnagea, M. Fuchs, H.-J. Grafe, G. Behr, R. Klingeler, S. Borisenko, C. Hess, S. Wurmehl, and B. Bu?chner. “Single Crystal Growth and Characterization of Superconducting LiFeAs”. In: *Crystal Growth & Design* 10.10 (2010), pp. 4428–4432.
doi:10.1021/cg1005538 (cit. on pp. 41, 49, 55, 73, 76, 79, 81, 83).

[53] S.-H. Baek, L. Harnagea, S. Wurmehl, B. Büchner, and H.-J. Grafe. “Anomalous superconducting state in LiFeAs implied by the ^{75}As Knight shift measurement”. In: *J. Phys.: Condens. Matter* 25.16 (Apr. 2013), p. 162204. ISSN: 1361-648X.
doi:10.1088/0953-8984/25/16/162204 (cit. on p. 42).

[54] C. Chu, F. Chen, M. Gooch, A. Guloy, B. Lorenz, B. Lv, K. Sasmal, Z. Tang, J. Tapp, and Y. Xue. “The synthesis and characterization of LiFeAs and NaFeAs”. In: *Physica C* 469.9-12 (May 2009), pp. 326–331. ISSN: 0921-4534.
doi:10.1016/j.physc.2009.03.016 (cit. on p. 42).

[55] S. J. Zhang, X. C. Wang, R. Sammynaiken, J. S. Tse, L. X. Yang, Z. Li, Q. Q. Liu, S. Desgreniers, Y. Yao, H. Z. Liu, and et al. “Effect of pressure on the iron arsenide superconductor $\mathrm{Li}_x\mathrm{FeAs}$ ($x = 0.8, 1.0, 1.1$)”. In: *Phys. Rev. B* 80.1 (July 2009). ISSN: 1550-235X.
doi:10.1103/physrevb.80.014506 (cit. on pp. 42, 43, 102, 106).

[56] X. Wang, Q. Liu, Y. Lv, Z. Deng, K. Zhao, R. Yu, J. Zhu, and C. Jin. “Superconducting properties of "111" type LiFeAs iron arsenide single crystals”. English. In: *Science China Physics, Mechanics and Astronomy* 53.7 (July 2010), pp. 1199–1201. ISSN: 1674-7348.
doi:10.1007/s11433-010-4031-0 (cit. on pp. 42–44, 57, 73).

[57] X. C. Wang, Q. Q. Liu, Z. Deng, Y. X. Lv, W. B. Gao, S. J. Zhang, R. C. Yu, and C. Q. Jin. “The Study of the Properties for "111" Type Iron Arsenide Superconductor”. In: *J. Supercond. Novel Magn.* 23.5 (Mar. 2010), pp. 583–585. ISSN: 1557-1947.
doi:10.1007/s10948-010-0736-6 (cit. on p. 42).

[58] Y. J. Song, J. S. Ghim, B. H. Min, Y. S. Kwon, M. H. Jung, and J.-S. Rhyee. “Synthesis, anisotropy, and superconducting properties of LiFeAs single crystal”. In: *Appl. Phys. Lett.* 96.21 (2010), p. 212508. ISSN: 0003-6951.
doi:10.1063/1.3435472 (cit. on pp. 42, 73, 79).

[59] B. Lee, S. Khim, J. S. Kim, G. R. Stewart, and K. H. Kim. “Single-crystal growth and superconducting properties of LiFeAs”. In: *EPL (Europhysics Letters)* 91.6 (Sept. 2010), p. 67002. ISSN: 1286-4854.
doi:10.1209/0295-5075/91/67002 (cit. on pp. 42, 73, 79).

[60] H. Kim, M. A. Tanatar, Y. J. Song, Y. S. Kwon, and R. Prozorov. “Nodeless two-gap superconducting state in single crystals of the stoichiometric iron pnictide LiFeAs”. In: *Phys. Rev. B* 83.10 (Mar. 2011). ISSN: 1550-235X.
doi:10.1103/physrevb.83.100502 (cit. on p. 42).

[61] J. L. Zhang, L. Jiao, F. F. Balakirev, X. C. Wang, C. Q. Jin, and H. Q. Yuan. “Upper critical field and its anisotropy in LiFeAs”. In: *Phys. Rev. B* 83.17 (May 2011). ISSN: 1550-235X.
doi:10.1103/physrevb.83.174506 (cit. on pp. 42, 83).

[62] S. Khim, B. Lee, J. W. Kim, E. S. Choi, G. R. Stewart, and K. H. Kim. “Pauli-limiting effects in the upper critical fields of a clean LiFeAs single crystal”. In: *Phys. Rev. B* 84.10 (Sept. 2011). ISSN: 1550-235X. doi:10.1103/physrevb.84.104502 (cit. on pp. 42, 83).

[63] F. Rullier-Albenque, D. Colson, A. Forget, and H. Alloul. “Multiorbital Effects on the Transport and the Superconducting Fluctuations in LiFeAs”. In: *Phys. Rev. Lett.* 109 (18 Nov. 2012), p. 187005. doi:10.1103/PhysRevLett.109.187005 (cit. on pp. 42, 43).

[64] S. Kasahara, K. Hashimoto, H. Ikeda, T. Terashima, Y. Matsuda, and T. Shibauchi. “Contrasts in electron correlations and inelastic scattering between LiFeP and LiFeAs revealed by charge transport”. In: *Phys. Rev. B* 85.6 (Feb. 2012). ISSN: 1550-235X. doi:10.1103/physrevb.85.060503 (cit. on p. 43).

[65] D. Bombor. “Transportmessungen an Supraleitenden Eisenpniktiden und Heusler-Verbindungen”. PhD thesis. Technische Universität Dresden, 2013. `http://nbn-resolving.de/urn:nbn:de:bsz:14-qucosa-160515` (cit. on pp. 43, 61, 66–68, 96).

[66] A. Alfonsov, B. Büchner, H.-J. Grafe, U. Gräfe, L. Harnagea, C. Hess, H.-H. Klauß, P. Materne, S.-H. Baek, D. Bombor, M. Braden, F. Hammerath, C. Rudisch, A. U. B. Wolter-Giraud, and S. Wurmehl. “Ferromagnetism in off-stoichiometric LiFeAs”. to be published in Physica Status Solidi. 2016 (cit. on pp. 43, 55–67, 96).

[67] J. D. Wright, M. J. Pitcher, W. Trevelyan-Thomas, T. Lancaster, P. J. Baker, F. L. Pratt, S. J. Clarke, and S. J. Blundell. “Magnetic fluctuations and spin freezing in nonsuperconducting LiFeAs derivatives”. In: *Phys. Rev. B* 88 (6 Aug. 2013), p. 060401. doi:10.1103/PhysRevB.88.060401 (cit. on pp. 44, 45, 57, 59, 60, 73, 93, 94, 102).

[68] F. Hammerath. “Magnetism and Superconductivity in Iron-based Superconductors as probed by Nuclear Magnetic Resonance”. PhD thesis. TU Dresden, 2011. `http://nbn-resolving.de/urn:nbn:de:bsz:14-qucosa-89865` (cit. on pp. 48, 49).

[69] NMR-Service. `http://www.nmr-service.de/home-de.html` (cit. on p. 49).

[70] W. G. Clark, M. E. Hanson, F. Lefloch, and P. Ségransan. “Magnetic resonance spectral reconstruction using frequency-shifted and summed Fourier transform processing”. In: *Review of Scientific Instruments* 66.3 (Mar. 1995), pp. 2453–2464. doi:10.1063/1.1145643 (cit. on p. 49).

[71] E. C. Stoner. “Collective Electron Ferromagnetism”. In: *Proceedings of the Royal Society A: Mathematical, Physical and Engineering Sciences* 165.922 (Apr. 1938), pp. 372–414.
doi:10.1098/rspa.1938.0066 (cit. on pp. 56, 64, 68, 71, 99, 105).

[72] M. Farle. “Ferromagnetic resonance of ultrathin metallic layers”. In: *Reports on Progress in Physics* 61.7 (1998), p. 755.
`http://stacks.iop.org/0034-4885/61/i=7/a=001` (cit. on p. 58).

[73] J. Smit and H. G. Beljers. In: *Philips Res. Rep.* 10 (1955), p. 113 (cit. on p. 58).

[74] C. Rudisch. “Nuclear Magnetic Resonance on Selected Lithium Based Compounds”. PhD thesis. Technische Universität Dresden, 2013.
`http://nbn-resolving.de/urn:nbn:de:bsz:14-qucosa-130485` (cit. on p. 60).

[75] M. Vannette, A. Sefat, S. Jia, S. Law, G. Lapertot, S. Bud’ko, P. Canfield, J. Schmalian, and R. Prozorov. “Precise measurements of radio-frequency magnetic susceptibility in ferromagnetic and antiferromagnetic materials”. In: *J. Magn. Magn. Mater.* 320 (2008), pp. 354–363. ISSN: 0304-8853.
doi:10.1016/j.jmmm.2007.06.018 (cit. on p. 60).

[76] K. Kitagawa, N. Katayama, K. Ohgushi, M. Yoshida, and M. Takigawa. “Commensurate Itinerant Antiferromagnetism in $BaFe_2As_2$: ^{75}As-NMR Studies on a Self-Flux Grown Single Crystal”. In: *J. Phys. Soc. Jpn.* 77.11 (2008), p. 114709.
doi:10.1143/JPSJ.77.114709 (cit. on pp. 62, 68).

[77] S.-H. Baek, N. J. Curro, T. Klimczuk, E. D. Bauer, F. Ronning, and J. D. Thompson. “First-order magnetic transition in single-crystalline $CaFe_2As_2$ detected by ^{75}As nuclear magnetic resonance”. In: *Phys. Rev. B* 79 (5 Feb. 2009), p. 052504.
doi:10.1103/PhysRevB.79.052504 (cit. on pp. 62, 63).

[78] T. Moriya. “The Effect of Electron-Electron Interaction on the Nuclear Spin Relaxation in Metals”. In: *J. Phys. Soc. Jpn.* 18 (1963), pp. 516–520.
doi:10.1143/JPSJ.18.516 (cit. on p. 63).

[79] S. Kitagawa, Y. Nakai, T. Iye, K. Ishida, Y. Kamihara, M. Hirano, and H. Hosono. “Stripe antiferromagnetic correlations in $LaFeAsO_{1-x}F_x$ probed by As^{75} NMR”. In: *Phys. Rev. B* 81 (21 June 2010), p. 212502.
doi:10.1103/PhysRevB.81.212502 (cit. on p. 63).

[80] F. Ning, K. Ahilan, T. Imai, A. S. Sefat, R. Jin, M. A. McGuire, B. C. Sales, and D. Mandrus. “Spin Susceptibility, Phase Diagram, and Quantum Criticality in the Eelctron-Doped High T_c Superconductor $Ba(Fe_{1-x}Co_x)_2As_2$”. In: *J. Phys. Soc. Jpn.* 78.1 (2009), p. 013711.
doi:10.1143/JPSJ.78.013711 (cit. on p. 63).

[81] N. J. Curro, A. P. Dioguardi, N. ApRoberts-Warren, A. C. Shockley, and P. Klavins. “Low-energy spin dynamics in the antiferromagnetic phase of $CaFe_2$ As_2”. In: *New J. Phys.* 11 (2009), p. 075004.
`http://stacks.iop.org/1367-2630/11/i=7/a=075004` (cit. on pp. 63, 64).

[82] A. Cano, M. Civelli, I. Eremin, and I. Paul. “Interplay of magnetic and structural transitions in iron-based pnictide superconductors”. In: *Phys. Rev. B* 82 (2010), p. 020408.
doi:10.1103/PhysRevB.82.020408 (cit. on p. 63).

[83] T. Moriya and K. Ueda. “Nuclear magnetic relaxation in weakly ferro-and antiferromagnetic metals”. In: *Solid State Communications* 15.2 (1974), pp. 169–172. ISSN: 0038-1098.
doi:http://dx.doi.org/10.1016/0038-1098(74)90733-9 (cit. on p. 63).

[84] G. Lang, H.-J. Grafe, D. Paar, F. Hammerath, K. Manthey, G. Behr, J. Werner, and B. Büchner. “Nanoscale Electronic Order in Iron Pnictides”. In: *Phys. Rev. Lett.* 104 (2010), p. 097001.
doi:10.1103/PhysRevLett.104.097001 (cit. on p. 68).

[85] G. Lang, L. Veyrat, U. Gräfe, F. Hammerath, D. Paar, G. Behr, S. Wurmehl, and H.-J. Grafe. “Spatial competition of the ground states in 1111 iron pnictides”. In: *Phys. Rev. B* 94 (1 July 2016), p. 014514.
doi:10.1103/PhysRevB.94.014514 (cit. on p. 68).

[86] M.-H. Julien, H. Mayaffre, M. Horvatić, C. Berthier, X. D. Zhang, W. Wu, G. F. Chen, N. L. Wang, and J. L. Luo. “Homogeneous vs. inhomogeneous coexistence of magnetic order and superconductivity probed by NMR in Co- and K-doped iron pnictides”. In: *Europhys. Lett.* 87 (2009), p. 37001.
`http://stacks.iop.org/0295-5075/87/i=3/a=37001` (cit. on p. 68).

[87] R. Zhou, L. Y. Xing, X. C. Wang, C. Q. Jin, and G.-q. Zheng. “Orbital order and spin nematicity in the tetragonal phase of the electron-doped iron pnictides $NaFe_{1-x}Co_xAs$”. In: *Phys. Rev. B* 93 (6 Feb. 2016), p. 060502.
doi:10.1103/PhysRevB.93.060502 (cit. on p. 68).

[88] P. Fazekas. *Lecture Notes on Electron Correlation and Magnetism (Series in Modern Condensed Matter Physics).* World Scientific Publishing Company, 1999. ISBN: 9810224745 (cit. on p. 68).

[89] J. Hubbard. “Electron Correlations in Narrow Energy Bands”. In: *Proceedings of the Royal Society of London A: Mathematical, Physical and Engineering Sciences* 276.1365 (1963), pp. 238–257. ISSN: 0080-4630.
doi:10.1098/rspa.1963.0204 (cit. on p. 68).

[90] N. Chen, S. Qu, Y. Li, Y. Liu, R. Zhang, and H. Zhao. “Synthesis of LiFeAs superconductor by electrochemistry at room temperature”. In: *Journal of Applied Physics* 107.9, 09E123 (2010).
doi:http://dx.doi.org/10.1063/1.3366609 (cit. on p. 73).

[91] S. J. Singh, U. Gräfe, R. Beck, A. U. Wolter, H.-J. Grafe, C. Hess, S. Wurmehl, and B. Büchner. “Physical properties optimization of polycrystalline LiFeAs”. In: *Physica C* 529 (2016), pp. 8–20. ISSN: 0921-4534.
doi:http://dx.doi.org/10.1016/j.physc.2016.08.004 (cit. on pp. 73, 74, 77–80, 82, 86, 89).

[92] U. Gräfe, S. J. Singh, R. Beck, C. Hess, S. Wurmehl, H.-J. Grafe, and B. Büchner. “Systematic Study of Off-Stoichiometric Li111 with Nuclear Quadrupole Resonance and Transport Measurements”. to be published in Physical Review B. 2016 (cit. on p. 85).

[93] H. M. Rietveld. “Line profiles of neutron powder-diffraction peaks for structure refinement”. In: *Acta Cryst* 22.1 (Jan. 1967), p. 151. ISSN: 0365-110X.
doi:10.1107/s0365110x67000234 (cit. on p. 86).

[94] J. Rodríguez-Carvajal. “Recent advances in magnetic structure determination by neutron powder diffraction”. In: *Physica B* 192.1-2 (1993), pp. 55–69. ISSN: 0921-4526.
doi:10.1016/0921-4526(93)90108-I (cit. on p. 86).

[95] W. Han, X. C. Wang, J. J. Gu, Q. Q. Liu, Z. Deng, and C. Q. Jin. “Doping effect on the physical properties of $\mathrm{Li}_x\mathrm{Fe}_{2-x}\mathrm{As}$”. In: *Int. J. Mod. Phys. B* 29.05 (Feb. 2015), p. 1550019.
doi:10.1142/s0217979215500198 (cit. on pp. 99, 106).

List of Figures

2.1 Non-spherical nucleus near external charges. 8
2.2 Schematic spin echo pulse sequence with a 90°-pulse and a 180°-pulse. 11

3.1 The Fermi sphere encloses all occupied electron states in the **k**-space. 16
3.2 Exemplification of the energy margin in which scattering is possible. 17
3.3 Qualitative picture of the energy bands $E_n(\mathbf{k})$ 19
3.4 Qualitative course of the density of states $D(E)$ 20
3.5 Schematic course of the band structure and the effective mass 22
3.6 Course of $E(\mathbf{k})$ and $\mathbf{v}(\mathbf{k})$ as functions of $\mathbf{k}$ 24
3.7 Temperature dependency for the resistivity of a typical metal. 29
3.8 Visualization of electron-electron-scattering in **k**-space 30
3.9 Example for resistivity dominated by electron electron scattering 31
3.10 Randomly distributed impurities. 32

4.1 Crystal Structures of IPS 34
4.2 Fermi surfaces of IPS 35
4.3 Fermi surface of LiFeAs from ten-orbital ARPES calculations 36
4.4 In-plane resistivity of LiFeAs as a function of temperature. 37
4.5 Gap function symmetries 38
4.6 Comparison of the schematic phase diagram of the IPS with the doping behavior of LiFeAs. 39
4.7 NQR spectra for stoichiometric LiFeAs. 40
4.8 Knight shift K as a function of temperature for stoichiometric LiFeAs. . . . 41
4.9 Susceptibility of stoichiometric LiFeAs with a ferromagnetic transition. . . . 43
4.10 Susceptibility measurements on $\mathrm{Li}_{1-y}\mathrm{Fe}_{1+y}\mathrm{As}$ 44
4.11 Muon-spin resonance data and phase diagram for $\mathrm{Li}_{1-y}\mathrm{Fe}_{1+y}\mathrm{As}$. 45

5.1 Schematic NQR setup. 48
5.2 Schematic of the 4-wire-sensing method 52

6.1 Susceptibility measurements on $\mathrm{Li}_{0.9}\mathrm{FeAs}$. 56
6.2 Development of the ferromagnetic resonance signal in $\mathrm{Li}_{0.67}\mathrm{Fe}_{0.975}\mathrm{Ni}_{0.025}\mathrm{As}$. 57

6.3 Ferromagnetic resonance measurements on $Li_{0.9}FeAs$ and $Li_{0.67}Fe_{0.975}Ni_{0.025}As$ 58
6.4 Muon-spin resonance measurements on $Li_{0.9}FeAs$. 59
6.5 Dynamic magnetic susceptibility of $Li_{0.9}FeAs$ 60
6.6 Magnetoresistance of $Li_{0.9}FeAs$ compared to stoichiometric LiFeAs 61
6.7 Nuclear quadrupole resonance spectra and intensities for Li deficient and Ni doped LiFeAs 62
6.8 $(T_1T)^{-1}$ for $Li_{0.67}Fe_{0.975}Ni_{0.025}As$ and stoichiometric LiFeAs 63
6.9 Comparison of magnetization measured with neutron scattering and static susceptibility of $Li_{0.9}FeAs$. 64
6.10 Nuclear quadrupole resonance spectra at room temperature of stoichiometric LiFeAs and $Li_{0.9}FeAs$ 65
6.11 Hall constant for $Li_{0.9}FeAs$ and $Li_{0.67}Fe_{1-x}Ni_xAs$ 66
6.12 Resistivity vs. temperature for $Li_{0.9}FeAs$ and $Li_{0.67}Fe_{1-x}Ni_xAs$ 67
6.13 Superconducting and ferromagnetic phase diagram of $Li_{1-y}Fe_{1-x}Ni_xAs$ built by nuclear quadrupole resonance. 72

7.1 NQR spectra for different synthesis temperatures and cooling rates. 75
7.2 NQR frequency and NQR line width for different synthesis temperatures T_{synth}. 76
7.3 Powder X-ray diffraction patterns of LiFeAs heated to 400 °C, 600 °C, 900 °C. 77
7.4 Lattice Parameters of LiFeAs prepared at different synthesis temperatures. . 78
7.5 Temperature dependency of the normalized magnetization $(\frac{M}{M_{1.8\,\mathrm{K}}})$ measured with zero-field cooling (ZFC) and field cooling (FC) mode for $H = 20\,\mathrm{Oe}$ of polycrystalline LiFeAs heated at 300-900 °C. 79
7.6 Resistivity data of LiFeAs for different T_{synth} 80
7.7 dependency of the mid-transition temperature (T_{mid}), transition width (ΔT_c) and residual resistivity ratio ($RRR = \frac{\rho_{300\,\mathrm{K}}}{\rho_{30\,\mathrm{K}}}$) from the synthesis temperature. 82

8.1 Nuclear quadrupole resonance (NQR) spectra for all series of off-stoichiometric LiFeAs. 87
8.2 NQR frequency and line widths 88
8.3 Unit cell volume plotted against refined occupancy y 90
8.4 Exemplary X-ray diffraction patterns for series Y and Z with $x = 10\,\%$. . . . 91
8.5 Combination of X-ray diffraction and nuclear quadrupole resonance 92
8.6 Exemplary results of static magnetic susceptibility (SMS) measurements on off-stoichiometric LiFeAs. 93
8.7 Field-dependent static magnetic susceptibility (SMS) on $LiFe_{1+x}As$. 94
8.8 Resistivity measurements on series Y. 95
8.9 Resistivity measurements on series Z. 96

8.10 Inverse residual resistivity ratio 97
8.11 Example fit of eq. (3.50) to a sample of series Y 98
8.12 Fit parameters of eq. (3.50) 99
8.13 Results of nuclear quadrupole resonance (NQR) measurements on a sample synthesized with $T_{\mathrm{synth}} = 1000\,^{\circ}\mathrm{C}$. 100
8.14 Magnetization of a sample synthesized with $T_{\mathrm{synth}} = 1000\,^{\circ}\mathrm{C}$. Measurements done by Shiv J. Singh. 101
8.15 Results of resistivity measurements on a sample synthesized with a synthesis temperature $T_{\mathrm{synth}} = 1000\,^{\circ}\mathrm{C}$. 102
8.16 Superconducting and Ferromagnetic Phase Diagram of off-stoichiometric LiFeAs with Fe excess built by nuclear quadrupole resonance. 103

List of Tables

4.1 RRR of various publications 42

7.1 Comparison of the physical properties of the optimized sample synthesized at $T_{\text{synth}} = 600\,^{\circ}\text{C}$ with published data for stoichiometric LiFeAs single crystals. 83

Acknowledgment

Diese Arbeit wäre nicht möglich gewesen ohne die Hilfe vieler Menschen, denen ich hiermit meinen Dank aussprechen möchte.

Zunächst möchte ich mich bei meinem Doktorvater Herrn Prof. Dr. Bernd Büchner dafür bedanken, dass ich meine Doktorarbeit am IFW Dresden durchführen konnte. Es war ein Privileg am IFW Dresden, mit all seinen technischen Möglichkeiten und dem internationalem Umfeld an Forschern, arbeiten zu dürfen. Ohne seine Zustimmung zu meiner Tätigkeit hätte ich dieses Privileg niemals genießen können.

Herrn Prof. Dr. Klingeler möchte ich danken für die Durchführung des zweiten Gutachtens dieser Arbeit.

Bei Dr. Christian Heß möchte ich mich für die Betreuung meiner Doktorarbeit bedanken und dafür, dass er immer für Ratschläge und Diskussionen zur Verfügung stand.

A special thanks goes to Dr. Shiv Jee Singh. Without his tireless efforts on preparing and characterizing the samples needed for this work, his willingness for excessive discussions and his encouragement in difficult situations, this work would never have come true.

Dr. Hans-Joachim Grafe danke ich für die Eröffnung des spannenden Themengebietes der Kernspinresonanz und der Möglichkeit zu zwei unvergesslichen Messreisen nach Florida.

Erik Haubold, Dr. Gregor Mittag und Dr. Yannic Utz möchte ich für die ausführlichen Korrekturen an meiner Arbeit danken.

Bedanken möchte ich mich auch bei den Mitgliedern der NMR-Gruppe, Dr. Hans-Joachim Grafe, Regina Vogel, Kristina Leger, Dr. Yannic Utz, Dr. Seung-Ho Baek, Tobias Schorr, Anastasia Bauernfeind, Dr. Markus Schäpers und Dr. Franziska Hammerath, sowie bei Dr. Frank Steckel, Richard Hentrich, Pranab Kumar Nag und den restlichen Mitgliedern der Transport und STM-Gruppe für anregende Diskussionen, erheiternde Mittagspausen, schöne Grillfeste und ausschweifende Weihnachtsfeiern.

Besonders hervorheben möchte ich an dieser Stelle Regina Vogel und Kristina Leger, welche durch ihren unermüdlichen Einsatz um das Wohlergehen des Labors den Messalltag um ein beträchtliches erleichtert haben.

Außerdem danke ich Dr. Yannic Utz für die Konstruktion und Programmierung des Auto Tuning Systems, ohne es hätten die Messungen wohl noch Jahre gedauert, sowie für Rat und Tat in fachlichen und persönlichen Belangen.

Bei den Mitgliedern des Elfenbeinturms, Dr. Jan Trinkauf, Dr. Tobias Ritschel, Erik Haubold, Maximilian Kusch, Dr. Yannic Utz, Dr. Frederik Klein und Dr. Christian Salazar Enriquez, sowie der gesamten Doktorandenschaft des Instituts für Festkörperforschung bedanke ich mich für eine großartige Arbeitsatmosphäre.

Außerdem danke ich allen meinen Freunden in Dresden, Berlin, Hamburg und sonst auf der Welt für Zuspruch, Freude, Lachen und Lernen.

Meinen persönlichsten Dank richte ich an meine Familie und meine Frau Katja Gräfe für ihre Unterstützung, Geduld und Liebe in allen Höhen und Tiefen meines Daseins.

Zu guter Letzt danke ich meinem Sohn Albert Gräfe, dass er mir, obwohl weniger als ein Jahr alt, immer wieder vor Augen führt, was letztlich wirklich wichtig ist.

Erklärung

Hiermit versichere ich, dass ich die vorliegende Arbeit ohne unzulässige Hilfe Dritter und ohne Benutzung anderer als der angegebenen Hilfsmittel angefertigt habe. Die aus fremden Quellen direkt oder indirekt übernommenen Gedanken sind als solche kenntlich gemacht. Die Arbeit wurde bisher weder im Inland noch im Ausland in gleicher oder ähnlicher Form einer anderen Prüfungsbehörde vorgelegt.

Diese Arbeit wurde unter Betreuung von Prof. Bernd Büchner am Institut für Festkörperforschung (IFF) des Leibniz-Institutes für Festkörper- und Werkstoffforschung Dresden e.V. (IFW Dresden) angefertigt. Es haben keine früheren Promotionsverfahren stattgefunden.

Ich erkenne hiermit die Promotionsordnung der Fakultät Mathematik und Naturwissenschaften der Technischen Universität Dresden vom 18.06.2014 an.

Uwe Gräfe
Dresden, 24. Februar 2017